CONTENTS Page

Research papers

Technical paper

DOI 10.12776/ams.v25i4.1364 p-ISSN 1335-1532
e-ISSN 1338-1156

TRIBOLOGY PROPERTIES EVALUATION FOR FRICTION PAIR Zn COATED STEEL –TiCN MP COATED/UNCOATED TOOL STEEL

Emil Evin[1)], Miroslav Tomáš[1)]*
[1)] Technical University of Košice, Faculty of Mechanical Engineering, Košice, Slovakia

Received: 12.11.2019
Accepted: 02.12.2019

[*]Corresponding author: e-mail: emil.evin@tuke.sk Tel.: +421 55 602 3547, Department of Automotive Production, Faculty of Mechanical Engineering, Technical University of Košice, Letná 9, 042 00 Košice, Slovakia

Abstract
When the sheet metal stamping processes are simulated, different values of the friction coefficient need to be defined in different regions, considering the nature of the deformation process. Thus, the regression and analytical models to determine the friction coefficient under the blank holder and on the die drawing edge by the strip drawing test are presented in the article. These models were verified by experimental strip drawing test under the same contact conditions. Zn coated high strength low alloyed steel sheet H220PD+Z100 was used at experiments and friction tests were done against the tool steel and TiCN MP coated tool steel. The results indicate, that values of friction coefficients evaluated by linear regression are lower than evaluated from analytical models. The positive effect of coating TiCN MP when applied on the contact surfaces was found, thus, decreases the friction coefficient and the drawing force scattering during the strip drawing test.

Keywords: deep drawing, strip drawing test, friction coefficient, experiment, analytical model

1 Introduction

There are many parameters influencing the sheet metal formability from the view of stamping, such as material properties, the die and the punch geometry, the contact surfaces' microgeometry, lubrication, etc. [1-5] Their accurate determination is ambiguous because these are changed from one case of the stamping process to another. Nowadays, simulation methods take place to predict their influence and to optimise the process parameters [6].

Because the simulations based on finite elements method becomes more and more important in pre-production, the accurate description of the input data is necessary. Besides constitutive equations describing material behaviour, contact conditions, i.e. friction coefficient on the contact surfaces needs to be defined as well. Sniekers [7] introduced the strip drawing test and method of data processing to calculate the friction coefficient at deep drawing. A new friction test method also presented Zhenyu [8]. Roizard [9] presented the improvement of strip drawing test emphasized to the influence of temperature effect, multi-pass, bulk plastic deformation. Kim [10] studied the pressure distribution in draw-bead friction test and its influence on the results of friction coefficient reached. Trzepieciński [11] studied the effect of sheet metal surface roughness, lubricant conditions and sheet orientation on the value of friction coefficient in sheet metal forming processes.

Nowadays, new coatings are applied on the contact surfaces in order to improve the contact conditions during deep drawing. Antoszewski et al. [12] tested electro spark (Cu+Ti) and (Mo-Ti)

coatings applied on the tool steel by pin-on-dics test and their influence on friction. Severo et al. [13] tested in semi-industrial conditions by strip drawing test W-Ti-N coatings and they showed excellent results in comparison with uncoated tools. New trends are focused to the abandonment of lubricants in metal forming processes from the economic and ecological points of view. Vollertsen [14] defined the term dry metal forming and presented its benefits and state of the art in this field. Häfner [15] studied the lubricant-free tribological systems such as laser based surface modifications of tetrahedral amorphous carbon (ta-C) coatings in flat strip drawing test.

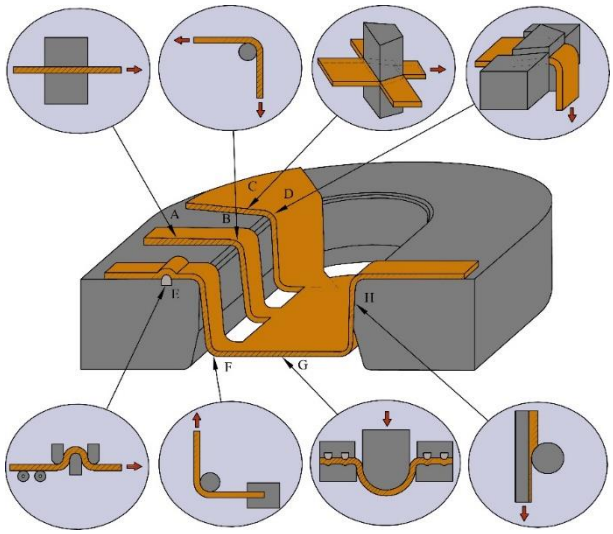

Fig. 1 Types of contacts at deep drawing

Stamping processes – deep drawing, stretching and bending – are characterized by different types of contact between the sheet metal and the die, as it is shown in **Fig. 1**: A – under the blank holder (bending or deep drawing of squared parts, blank is not deformed), B – on the drawing edge (blank is bend and drawn into the die, blank is deformed in radial direction and tangential deformation is negligible), C – corner of the stamped part under the blank holder (friction arises due to compressive tangential deformation when blank is drawn into the die), D - corner of the stamped part on the drawing edge (blank is deformed by the tensile radial and compressive tangential strains), E – the loading of contact surfaces in the drawing bead when it is applied to regulate the material flow in the straight parts, F – the loading of contact surfaces on punch drawing edge, G – stretching of the blank on the punch face, H – calibration of the part stamped. [16, 17]

2 Experimental material and methods

High strength low alloyed steel sheet H220PD with thickness a_0 = 0.8 mm was used in experimental research and Zn coating 100 g.m^{-2} was applied at both sides. Chemical composition is shown in **Table 1** and the surface roughness parameters measured by Surftest SJ-301 were as follows: Ra = 1.46 ± 0.06 μm; RPc = 67 ± 5 cm^{-1}; Rz = 5.2 ± 0.2 μm. Surface texture measured by Olympus BX51 M is shown in **Fig. 2**.

Table 1 Chemical composition of HSLA Zn coated steel H220PD + Z100 [wt %]

C	Mn	Si	P	S	Al	Nb	Ti
0.004	0.415	0.1	0.042	0.004	0.031	0.017	0.037

Mechanical properties were measured by ISO 6892-1, normal anisotropy ratios by ISO 10 113 at strain level of 20% and strain-hardening exponents by ISO 10 275 within the strain range 5÷20%. PC controlled TiraTEST 2300 testing machine with extensometers for both, the length and the width measurement was used with automated evaluation of properties shown in **Table 2**.

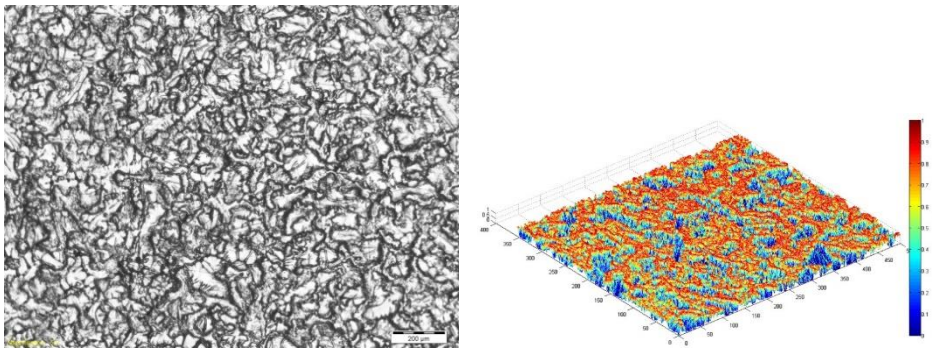

a) b)

Fig. 2 Surface texture of experimental material HSLA Zn coated steel H220PD + Z100 a) microscope 2D view, b) generated in Matlab 3D view

Table 2 Formability parameters of HSLA Zn coated steel H220PD + Z100

Dir. [°]	$R_{p0.2}$ [MPa]	Rm [MPa]	A_g [%]	A_{80} [%]	K [MPa]	n [-]	r [-]
0	214	375	24	40	677	0.24	1.21
45	217	359	26	42	651	0.23	1.76
90	223	368	23	38	658	0.23	1.75

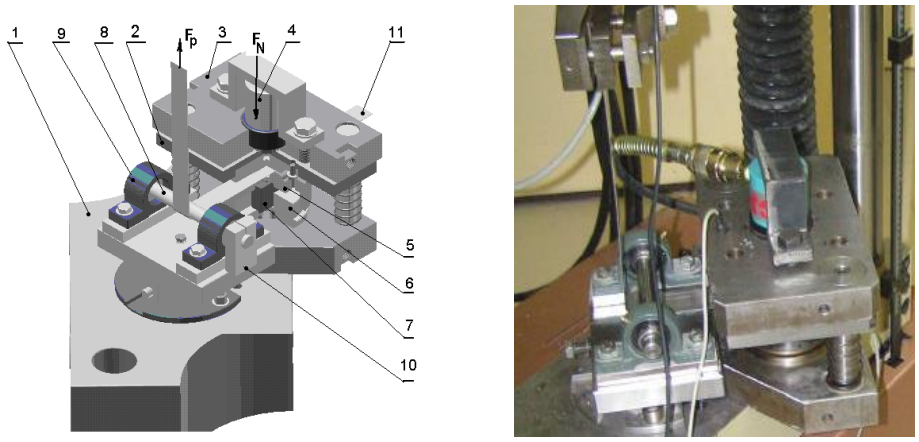

a) b)

Fig. 3 The friction simulator - strip drawing test: a) model, b) real view
1 - base plate, 2 – midplate, 3 – upper plate, 4 – clamping cylinder, 5 - upper grip, 6 - lower grip, 7 – blank-holding force cell, 8 – roller, 9 - ball bearings, 10 – roller brake, 11 - strip

The friction simulator shown in **Fig. 3** was used to study friction in a stamping process. This simulator enables modelling the stress state of flat (Fig. 1-A) and curved regions (Fig. 1-B).

Processes on the contact areas can be investigated separately or combined. The roller can be fixed or free rotated. If the movement of roller is not blocked, we model the loading of die contact areas under blank holder between flat surfaces (Fig. 1-A). In the case the roller is fixed we model the loading of curved contact areas on the die drawing edge (Fig. 1-B).

Drawing conditions were as follows: blank holding forces F_N = 2; 4; 6 and 8 kN, strip drawing speed v = 10 mm/s, strip width 50 mm, grips' contact area 20x50 mm. Both, grips and roller of the friction tester were made from tool steel 1.2379, hardened to 63 HRc and polished to Ra = 0.32 ± 0.05 µm. During the test, exchangeable grips were used and this allowed modelling friction conditions tool steel/Zn surface and TiCN MP coating/Zn surface. Thus, TiCN MP coating was applied on the grips and the roller as well to research the influence of coating to the friction coefficient.

Adhesion and other properties of TiCN MP coating were measured by series of tests. Coating thickness 3.19 µm was measured by Calotest method (**Fig. 4**), microhardness H_{IT} = 51 GPa and modulus E = 480 GPa by indentation tester TTX-NHT S/N with Berkovich diamond indenter at 60mN load, sinusoidal frequency 15 Hz and amplitude 6 mN, holding time 10s. Coating adhesiveness measured by Mercedes test was HF1 (**Fig. 5**) and Scratch test confirmed good adhesion and compactness by acoustic emissivity 0.8 V and the cohesive failure were found at the force L_{C1} = 34.7 ± 4.0 N, adhesion failure and spallation of the coating was found at the force L_{C2} = 41.6 ± 2.6 N and critical force to surface exposure at the centre of the track L_{c3} = 86.1 ± 2.9 N – **Fig 6**.

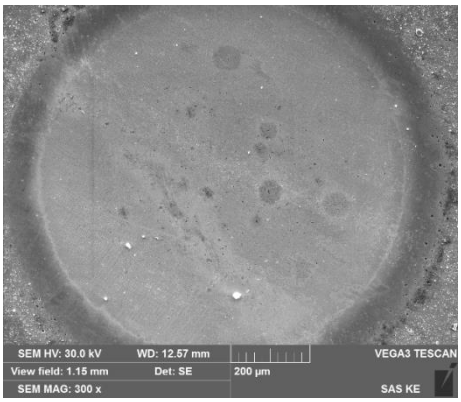

Fig. 4 TiCN MP coating thickness measurement (Calotest method)

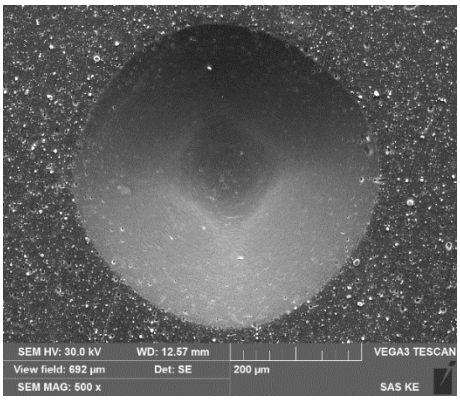

Fig. 5 Mercedes test result for TiCN MP coating

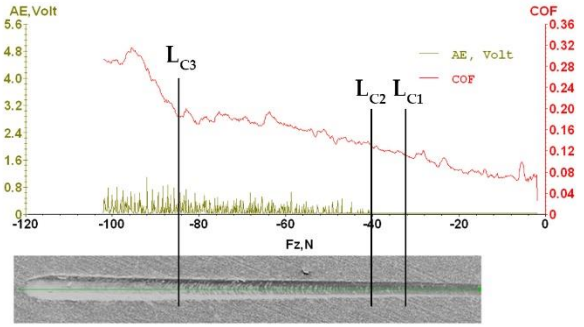

Fig. 6 Scratch test result for TiCM MP coating

Surface roughness after coating deposition measured by Surftest SJ-201 was as follows: Ra = 0.24 ± 0.04 μm and Rz = 2.78 ± 0.15 μm when measured in grinding direction (i.e. longitudinal) and Ra = 0.20 ± 0.05 μm and Rz = 2.40 ± 0.11 μm when measured perpendicular to the grinding direction (i.e. transverse).

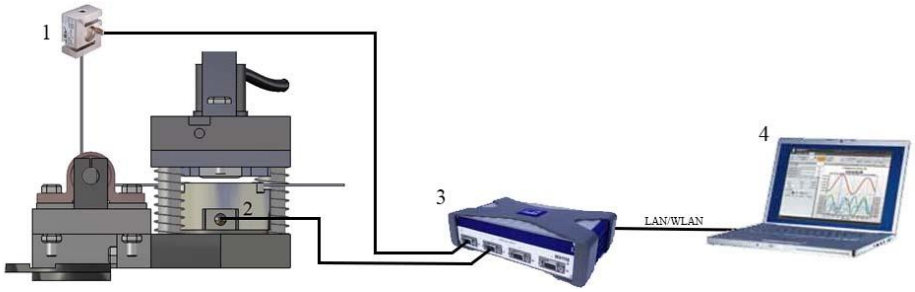

Fig. 7 Measuring system at strip drawing test

The drawing force and the blankholding force were measured during the strip drawing test. Measuring system (**Fig. 7**) consisted of force load cells KAS 20 (1) and KF 20 K (2), tensometric measuring unit QuantumX MX440A (3) and software Catman Easy (4).
Record of drawing and blankholding forces is shown in **Fig. 8** and **Fig. 9** in the next chapter. From experimentally measured values of drawing and blankholding forces the friction coefficient can be determined in the area under blankholder and on the die drawing edge also. Two methods were applied for evaluation of friction coefficient in the area under blankholder.
In the first method the regression analysis was used [16, 17, 18]. The relation between blankholding force and drawing force can be described as follows:

$$\Delta F_{p(f3=0)} = \text{Intercept} + \Delta F_{N1,2}(\text{Slope}) \tag{1.}$$

where: $\Delta F_{p(f3=0)}$ [N] - the difference of drawing forces,
$\Delta F_{N1,2}$ [N] - the difference of blanholding forces $F_{N2} - F_{N1}$, $F_{N2} > F_{N1}$.
Drawing forces increases with the increase of blankholding forces. Thus, the friction coefficient $f_{1,2}$ is calculated as half value of slope:

$$f_{1,2} = \frac{\text{Slope}}{2} \tag{2.}$$

where: $f_{1,2}$ [-] - the mean friction coefficient between die and strip.
The second method comes out from analytical models based on measurement of forces during strip drawing test [17, 18, 19]. When the roller on the friction simulator is not blocked (friction model under the blankholder), the friction coefficient $f_{1,2}$ is calculated as follows:

$$f_{1,2} = \frac{F_{p2(f3=0)} - F_{p1,ref(f3=0)}}{2(F_{N2} - F_{N1,ref})} = \frac{\Delta F_{p1,2(f3=0)}}{2 \cdot \Delta F_{N1,2}} \tag{3.}$$

where: $F_{N1,ref}$ = 2000 N,
F_{N2} [N] – the blankholding force ($F_{N1,ref} < F_{N2}$),
$F_{p2(f3=0)}$ [N] - the drawing force generated by blankholding force F_{N2},
$F_{p1,ref(f3=0)}$ [N] – the drawing force generated by blankholding force $F_{N1,ref}$.

DOI 10.12776/ams.v25i4.1362 p-ISSN 1335-1532
e-ISSN 1338-1156

When the roller on the friction simulator is blocked (friction model on the die drawing edge), the friction coefficient f_3 is calculated as follows:

$$f_3 = \ln\left(\frac{F_{p(f3>0)}}{F_{p(f3=0)}}\right)\frac{2}{\pi} \tag{4.}$$

where: $F_{p(f3=0)}$ [N] – the drawing force generated by a rotating roller,
$F_{p(f3>0)}$ [N] – the drawing force generated by a fixed roller,
f_3 [-] – the friction coefficient on the die drawing edge.

3 Results and discussion

Table 3 shows set values of blankholding forces F_N and measured values of drawing forces $F_{p(f3=0)}$ and $F_{p(f3>0)}$. As it is shown in **Fig. 8** and **Fig. 9**, there was scattering in drawing force for specific pressure over 4 MPa when measured for friction pair tool steel / Zn surface and over 8 MPa when measured for friction pair TiCN MP / Zn surface. Thus, the average values of forces were evaluated beyond the 60 s to exclude initial bending of the strip.

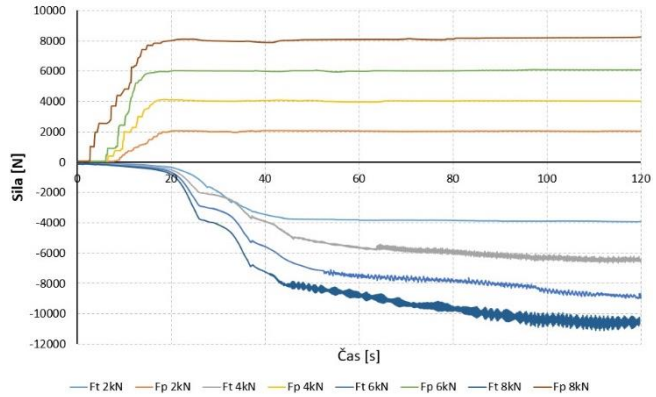

Fig. 8 Record of the drawing and blankholding forces at strip drawing test for friction pair tool steel / Zn surface

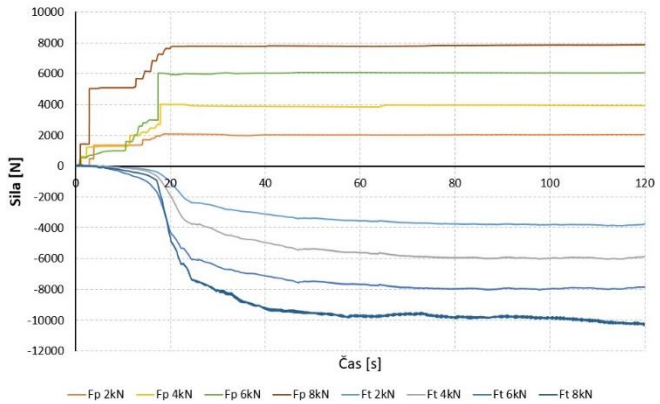

Fig. 9 Record of the drawing and blankholding forces at strip drawing test for friction pair TiCN MP / Zn surface

DOI 10.12776/ams.v25i4.1362 p-ISSN 1335-1532
e-ISSN 1338-1156

Table 3 Measured values of forces and calculated values of friction coefficient – no lubricant

Friction pair	Normal force F_N [N]	Specific pressure p [MPa]	Drawing force F_P [N]		Friction coefficient f [-]		
			$f_3 = 0$	$f_3 > 0$	$f_{1,2}$ Eq. (2.)	$f_{1,2}$ Eq. (3.)	f_3 Eq. (4.)
H220PD+Z100 - Tool steel	2039	2	2280	3816	0.304		0.328
	4033	4	3689	6075		0.353	0.318
	6068	6	4931	8447		0.329	0.343
	8121	8	6178	10119		0.320	0.314
H220PD+Z100 - TiCN	2032	2	2310	3741	0.296		0.307
	4030	4	3580	5905		0.318	0.319
	6047	6	4779	7874		0.307	0.318
	8050	8	5963	9950		0.304	0.326

When evaluated from Eq. (2.), the friction coefficient for friction pair tool steel – Zn surface was 0.304 and for friction pair TiCN MP coating / Zn surface it was 0.296. When friction coefficient evaluated under the blank holder according to Eq. (3.), it varied from 0.320 to 0.353, i.e. 0.334 ± 0.017 for friction pair tool steel / Zn surface; and from 0.304 to 0.318, i.e. 0.310 ± 0.007 for friction pair TiCN coating / Zn surface. When friction coefficient evaluated on the drawing edge according to Eq. (4.), it varied from 0.314 to 0.343. i.e. 0.326 ± 0.013 for friction pair tool steel / Zn surface; and from 0.307 to 0.326, i.e. 0.317 ± 0.008.

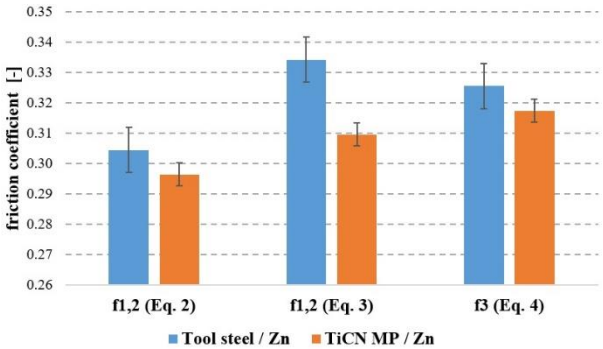

Fig. 10 Comparison of friction coefficient calculated by linear regression (Eq. 2.) and from analytical models (Eq. 3. and Eq. 4.)

The average values of friction coefficient calculated from Eq. (2.), Eq. (3.) and Eq. (4.) are shown and compared in **Fig. 10**. The lowest average value of the friction coefficient was reached when calculated from Eq. (2.), but the average friction coefficient under the blank holder calculated from Eq. (3.) and on the die drawing edge calculated from Eq. (4.) are higher. As supposed in the [16,18], Eq. (2.) gives the averaged friction coefficient and the method is not suitable to evaluate the friction coefficient in different regions.

There were found lower values of friction coefficient for friction pair TiCN MP / Zn coating when calculated from each equation. The results partially comply to the roughness measurement, when lower roughness was identified on the grips after coating the tool steel with TiCN MP coating. Decrease in roughness after coating was reached by Choi [20] also, while Merklein [21] confirmed decreasing the friction coefficient measured at dry conditions for smooth and polished surfaces.

DOI 10.12776/ams.v25i4.1362 p-ISSN 1335-1532
e-ISSN 1338-1156

As it is shown in **Fig. 8**, scattering occurred in the drawing force if the normal force is higher than 4 kN (i.e. specific pressure under the blankholder 4 MPa) when measured for friction pair tool steel / Zn surface. In the case of friction pair TiCN MP coating / Zn surface in **Fig. 9**, scattering in the drawing force occurred only if the normal force 8 kN (i.e. specific pressure under the blank holder 8 MPa) was applied. Roizard in [9] stated the scattering is a result of stick-slip sliding regime at low velocities when the static frictional is nonzero. Considering mentioned and the strip velocity 10 $mm.s^{-1}$, the effect of the TiCN MP coating resulted in a reduction of scattering the drawing force for specific pressure 4 and 6 MPa and the amplitude of scatters decreased for higher specific pressure 8 MPa.

The contact pressure is one of the parameters influencing the friction [22]. When the friction coefficient $f_{1,2}$ calculated from Eq. (3.), i.e. under the blank holder, its value decreases with the contact pressure. The same tendency was found by Trzepiecinski [23] for the strip drawing test performed. But contrary to the results [22] and [23], the dependence of friction coefficient f_3 calculated from Eq. (4.), i.e. on the die drawing edge, on the contact pressure is not unequivocal for both friction pairs tested.

4 Conclusions

Nowadays, lubricant free sheet metal stamping processes appears being a challenge. Besides ecology point of view, economic aspects are also important due to avoid degreasing the stampings. Thus, the article is focused to the friction coefficient measurement under the dry condition for friction pair tool steel / Zn surface and TiCN MP coated tool steel / Zn surface. While the friction coefficient under the blank holder evaluated by linear regression gives the average value, analytical models allow calculating the friction coefficient under the blank holder and on the die drawing edge as well. The effect of TiCN MP coating applied on the tool steel resulted in lower friction coefficients and minimizing the drawing force scattering. Further research will focus to the galling phenomena and verification the results by the simulation.

References

[1] K. Lange: Umformtechnik – Handbuch fur Industrie und Wissenschaft, second ed., Springer/Verlag, Berlin, 2002

[2] J. Bilík, V. Titel, M. Dobisova, R. Suba: Research Papers FMSaT in Trnava, Slovak University of Technology in Bratislava, Vol. 27, 2009, p. 15-20.

[3] O. Mahrenholtz, N. Bontcheva, R. Iankov: Journal of Materials Processing Technology, Vol. 159, Issue 1, 2005, p. 9-16, https://doi.org/10.1016/j.jmatprotec.2003.10.009

[4] T. Kvačkaj et al.: Archives of Metallurgy and Materials, Vol. 58, Issue 2, 2013, p. 407-412, https://doi.org/10.2478/amm-2013-0008

[5] P. Petroušek et al.: Acta Metallurgica Slovaca, Vol. 21, No. 3, 2015, p. 176-183, http://dx.doi.org/10.12776/ams.v21i3.615

[6] A. Schrek, P. Švec, A. Brusilová, Z. Gábrišová: Strojnicky Casopis, Vol. 68, Issue 1, 2018, p. 95-102, https://doi.org/10.2478/scjme-2018-0010

[7] R. J. J. M. Sniekers, H. A. A. Smits: Journal of Materials Processing Technology, Vol. 66, Issues 1-3, 1997, p. 216-223, https://doi.org/10.1016/S0924-0136(96)02526-5

[8] H. Zhenyu, F. Vollertsen: Journal for Technology of Plasticity, Vol. 29, 2004, p.1-9

[9] X. Roizard, J.M. Pothier, J.Y. Hihn, G. Monteil: Journal of Mat. Processing Technology, Vol. 209, Issue 3, 2009, p. 1220-1230, https://doi.org/10.1016/j.jmatprotec.2008.03.023

DOI 10.12776/ams.v25i4.1362 p-ISSN 1335-1532
e-ISSN 1338-1156

[10] Y. S. Kim, M. K. Jain, D. R. Metzger: Non- uniform Pressure Distribution in Draw- Bend Friction Test and its Influence on Friction Measurement. In: AIP Conference Proceedings 778, 661 (2005), https://doi.org/10.1063/1.2011298
[11] T. Trzepieciński: International Journal of Automotive Technology, Vol. 16, Issue 5, 2015, p. 849-863, http://dx.doi.org/10.1007/s12239-015-0087-1
[12] B. Antoszewski, E. Evin, J. Audy: Journal of Tribology, Vol. 130, Issue 2, 2008, p. 021303-1 -021303-6, https://doi.org/10.1115/1.2842296
[13] Severo et al.: Journal of Materials Processing Technology, Vol. 209, Issue 10, 2009, p. 4662-4667, https://doi.org/10.1016/j.jmatprotec.2008.11.040
[14] F. Vollertsen, F. Schmidt: Int. Journal of Precision Engineering and Manufacturing-Green Technology, Vol. 1, Issue 1, 2014, p. 59-62, https://doi.org/10.1007/s40684-014-0009-0
[15] T. Häfner et al.: Journal of Laser Micro/Nanoengineering, Vol. 12, No. 2, 2017, p. 132-140, https://doi.org/10.2961/jlmn.2017.02.0015
[16] A. Hrivnak, E. Evin: Formability of steel sheets, first ed., Elfa, Košice, 2004
[17] E. Evin, M. Tomáš, M. Výrostek: Acta Mechanica Slovaca, Vol. 20, Issue 1, 2016, p. 14-21, https://doi.org/10.21496/ams.2016.003
[18] J. Audy, E. Evin: MM Science Journal, Vol. 6, 2008, p. 20-23, https://doi.org/10.17973/MMSJ.2008_06_20080601
[19] E. Evin, M. Tomáš, M. Kollárová, B. Antoszewski: Acta Metallurgica Slovaca, Vol. 20, No. 2, 2014, p. 189-199, http://dx.doi.org/10.12776/ams.v20i2.298
[20] H. S. Choi et al.: International Journal of Precision Engineering and Manufacturing, Vol. 15, Issue 6, 2014, p. 1101-1107, https://doi.org/10.1007/s12541-014-0443-5
[21] M. Merklein, K. Andreas, J. Steiner: International Journal of Precision Engineering and Manufacturing-Green Technology, Vol. 2, Issue 2, 2015, p. 131-137, https://doi.org/10.1007/s40684-015-0017-8
[22] Y. S. Kim, M. K. Jain, D. R. Metzger: Int. Journal of Machine Tools & Manufacture, Vol. 56, May 2012, p. 69-78, https://doi.org/10.1016/j.ijmachtools.2011.12.011
[23] T. Trzepieciński: Metals, No. 9, Issue 9, 2019, 988, https://doi.org/10.3390/met9090988

Acknowledgements

Authors are grateful for the support of experimental works by projects APVV-0273-12 "Supporting innovations of autobody components from the steel sheet blanks oriented to the safety, the ecology and the car weight reduction", VEGA 2/0800/19 "Prediction of weldability and formability for laser welded tailored blanks made of combined high strength steels with CAE support" and APVV-17-0381 "Increasing the efficiency of forming and joining parts of hybrid car bodies".

CORROSION BEHAVIOUR OF AISI 460LI SUPER-FERRITIC STAINLESS STEEL

Andrea Di Schino[1)*]
[1)]*Università degli Studi di Perugia, Dipartimento di Ingegneria, Perugia, Italy*

Received: 21.10.2019
Accepted: 31.10.2019

[*]*Corresponding author: andrea.dischino@unipg.it, Dipartimento di Ingegneria, Università di Perugia, Via G. Duranti, 01625 Perugia, Italy*

Abstract
Following nickel and molybdenum significant price increase, nowadays the stainless steel market is moving toward an increasing use of ferritic stainless steel instead of austenitic stainless and therefore to the development of advanced ferritic stainless steels grades aimed to substitute the more expensive austenitic materials in all applications allowing it. Super-ferritic stainless steels are higher chromium (Cr) and molybdenum (Mo) steels with properties similar to those of standard ferritic alloys. Such elements increase high temperature and corrosion resistance in strong environment. This paper deal about the corrosion resistance of super-ferritic stainless steels with a Cr content ranging from 21% to 24%.

Keywords: Stainless steels, corrosion resistance, microstructure

1 Introduction

Stainless steels are nowadays applied in many applications facing with strength/ductility requirements coupled with corrosion resistance high targets. In particular, they are adopted in automotive [1-7], construction and building [8-9], energy [10-13], aeronautical [14], medical [15], food [16-21] and 3D printing [22-26] applications. Ferritic stainless steels are more and more required following their lower cost with respect to austenitic stainless steels. As a consequence, there is a strong market demand for innovative ferritic stainless steel grades with the aim to substitute the most expensive austenitic grades in all those applications allowing it.
Based on the above considerations, an innovative stainless steel grade with 22% Cr and a very low interstitial and stabilizing element content is here analyzed. Also Mo is kept at very low level in such materials with the aim to further lower their cost. Even if some data were already published on such materials mechanical behavior [27-31], not many data are still available on their corrosion resistance. Aim of this paper is to evaluate the corrosion resistance of 460LI steel aimed to face the materials selection criteria for stainless steels in specific applications.

2 Experimental materials and methods

AISI 460LI stainless steel is here considered in comparison to standard AISI 304 steel. The chemical composition of the analyzed steels is reported in **Table 1** (in accordance to UNI EN 10088-2).

Table 1 Chemical composition of the analysed stainless steels (UNI EN 10088-2).

	C (%)	N (%)	Cr (%)	Ni (%)	Ti (%)	Nb (%)	Mo (%)
304 (1.4301)	≤0.07	≤0.11	17.5÷19.5	8.0÷10.5	-	-	-
460LI (1.4611)	<0.03	-	19.0÷22.0	<0.5	<1	<1	<0.5

DOI 10.12776/ams.v25i4.1363 p-ISSN 1335-1532
e-ISSN 1338-1156

Materials corrosion resistance was assessed in terms of:

General corrosion resistance

General corrosion resistance has been tests in a salt spray chamber (WEISS system model SSC 450) at 35°C with a nebulized 5%wt of NaCl solution according to UNI EN ISO 9227. Samples were 100 mm x 200 mm. Samples were cleaned with acetone before testing; edges were protected with wax and pix. Then, samples were placed into the chamber hunged on a plastic rack to maintain them at 20 °C respect to the vertical position. This arrangement was essential to avoid mutual contact between samples or with other parts of the chamber. Total duration of this test was 1000 h. Generalized corrosion resistance from chemical agents and conditions typical for stainless steels was tested dipping samples of 20 mm x 50 mm dimensions (polished until to 120 mesh) in 8 solutions at different temperatures, as reported in **Table 2** according to ASTM G157. Before the beginning of the test and after every exposure cycle, samples were weighted and measured to determine the corrosion rate expressed in mm/year.

Table 2 Tested stainless steels and solutions according to ASTM G157. (*only for 470LI)

Corrosive environment (conc.%)	**Test temperature (°C)**
Nitric acid (70%)	30, 70
Acetic acid (80%)	30, 70
Sodium chloride (50%)	30, 70
Caustic soda (50%)	30, 70, 90, 110*
Alum vitriol (10%)	30, 70
Phosphoric acid (85%)	30, 70
Methanol (99.9%)	30, 70
Acetone (99.5%)	30, 70
Urea (32.5%)	-5, 45
Orange juice (100%)	30
Milk (100%)	30, 50

Localized corrosion resistance

Potentio-dynamic polarization curves were measured using an electrochemical cell with three electrodes, with a calomel reference electrode (SCE) and a platinum counter-electrode, immersed in a 3% NaCl solution at room temperature. To realize the potentio-dynamic curves, a Solatron 1287 was used connected to a PC for setting the beginning value of the potential scan, the power value and the surface (1 cm^2) of metal exposed to the corrosive agent. Starting from a potential of 1V (lower than the open circuit potential), a scan rate of 1 mV/s was set and an intensity of the inversion current equal to 5 mA/cm^2. Samples before the beginning of the test were polished until 600 mesh. Moreover:

Critical Pitting Temperature (CPT) has been determined by immersing different samples in a solution of 6% $FeCl_3$ for 24 h at a fixed temperature; this scheme was repeated increasing each time the solution's temperature of 5°C until it was possible to observe the onset of pitting phenomena. Samples had dimensions of 30 mm x 40 mm, with rounded corners. Moreover both samples' surfaces were polished at 120 mesh.

Crevice critical temperature (CCT) determination was realized with the same test procedure used to detect the critical pitting temperature (CPT). The only difference applied on the samples' surfaces regarded two Teflon cylinders with a diameter of 12 mm. 20 embossed sectors were made

DOI 10.12776/ams.v25i4.1363 p-ISSN 1335-1532
e-ISSN 1338-1156

on the cylinders and held together by a nickel-based alloy screw (shielded with Teflon). Test in salt spray chamber was performed applying on the samples two cylinders made in Teflon with a diameter of 50 mm. On their surfaces were also obtained 12 embossed sector. Test duration was 260 h and the spray solution had a content of 5% NaCl as reported in UNI EN ISO 9227. At the end of the cycle, samples were visually analyzed counting the number of sectors imprinted on the sample and assessing, with the same criteria, the gravity.

Stress corrosion resistance

Stress corrosion susceptibility was measured immerging samples, previously bended (U- bend samples), in a boiling solution of $MgCl_2$ (42%) for 500 h, according to ASTM G30-97 standard. At the end of the test, samples were observed with a low magnification microscope, to identify the presence of cracks.

3 Results

Results of general corrosion resistance tests performed in corrosive environments for the 460LI steel are reported in **Table 3**. The testing environment has been chosen with the scope to put in evidence the material attitude to be put in service in applications including chemical sector and food industry. In every case, the result of the test was positive and the corrosion rate was widely within the ASTM G157 limit (0.13 mm/year).

Table 3 General corrosion resistance of 460LI for different corrosive media (ASTM G157). √: corrosion rate <0.13mm/year; X: corrosion rate>0.13mm/year

Steel	Corrosive agent (conc. %)	T_{max} (°C)	Test result (48h)	Test result (96h)
460LI	Nitric acid(70%)	70	√	√
	Acetic acid (80%)	70	√	√
	Sodium chlorate (50%)	70	√	√
	Caustic soda (50%)	70	√	√
	Alum vitriol (10%)	70	√	√
	Phosphoric acid (85%)	70	√	√
	Methanol (99.9%)	70	√	√
	Acetone (99.5%)	59	√	√
	Orange juice (100%)	Boiling	√	√
	Milk (100%)	50	√	√

Passivation current density for AISI 460LI with respect to AISI 304 grade are reported in **Table 4**. Results show lower passivation current density with respect to standard AISI 304 steel. Such values are anyway typical of materials suitable for the target applications.

Table 4 Electrochemical parameters calculated in the anodic polarization curves in 3% NaCl solution

Steel	i_{pass} (A/cm^2)	E_{pit} (mV/SCE)	E_{rep} (mV/SCE)
460LI	$1.4 \cdot 10^{-6}$	430	-110
304	$2.5 \cdot 10^{-6}$	360	-66

DOI 10.12776/ams.v25i4.1363 p-ISSN 1335-1532
e-ISSN 1338-1156

The critical pitting and crevice temperatures, calculated according to ASTM G48, are reported in **Table 5**. The critical pitting temperature of the super-ferritic stainless steel is higher than the austenitic stainless steel, while the pitting critical temperature is comparable.

Table 5 Comparison of CPT and CCT tested in a 10% $FeCl_3$ solution (ASTM G48-E and ASTM G48-F)

Steel	CPT (°C)	CCT (°C)
460LI	10	0
304	4	-

Photos of samples after crevice test in salt spray chamber for 260 h are reported in **Fig. 1**. The number of sectors imprinted on the sample and their severity are reported in **Table 6**. Results show similar behavior in the AIS 460LI and AISI 304 steels.

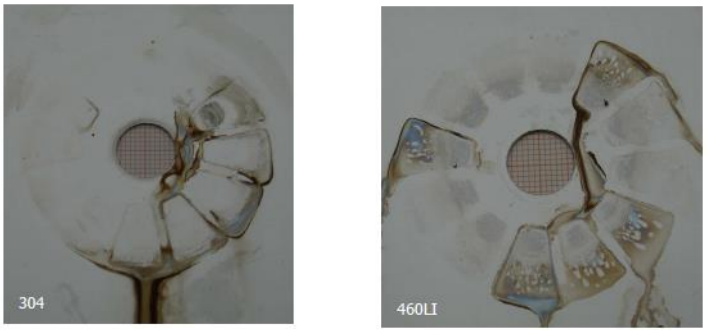

a) b)

Fig. 1 Samples tested in salt spray chamber for the crevice resistance test.

Table 6 Summary of visual inspection at the end of the salt spray chamber cycle.

Steel	Embossed sector	Severity grade
460LI	5	Medium
304	5	Medium

AISI 460LI and AISI 304 steel U-bend samples were immerged in a boiling solution of MgCl2 for 500h. At the end of the test, samples were observed with a low magnification microscope, to identify the presence of cracks and by Electron Scanning Microscope. Analyses reported that the super-ferritic samples are not susceptible to stress corrosion cracking while the tested samples of 304 achieves break, as expected for austenitic stainless steels.

4 Conclusion

The corrosion resistance of AISI 460LI super-ferritic stainless steel is analyzed.
Results show that:
AISI 460 LIA guarantee comparable properties with respectl of austenitic stainless steels in terms of general corrosion resistance. Also, the corrosion resistance tests through immersion in different environments detected low corrosion rates.
The pitting corrosion behavior was a little worst with respect to that of the AISI 304 steel grade.
The super-ferritic stainless steels are not affected by stress corrosion.

DOI 10.12776/ams.v25i4.1363 p-ISSN 1335-1532
e-ISSN 1338-1156

References

[1] P. Marshall: Austenitic stainless steels: Microstructure and Mechanical Properties, Elsevier Applied Science Publisher, 1984
[2] L. Viet, J. Hye-Jin: Metals, Vol.8, 2018, 815, https://doi.org/10.3390/met8100815
[3] C. Xingrun, R. Xiang: Metals, Vol. 8. 2018, 1024, https://doi.org/10.3390/met8121024
[4] D. Hongjinng: Metals, Vol. 9. 2019, 74, https://doi.org/10.3390/met9010074
[5] A. Tachieva: Metals, Vol. 9. 2019, 347, https://doi.org/10.3390/met9030347
[6] A. Prosviryakov: Metals, Vol. 9. 2019, 218, https://doi.org/10.3390/met9020218
[7] R. Rufini, O. Di Pietro, A. Di Schino: Metals, Vol. 8, 2018, 519, https://doi.org/10.3390/met8070519
[8] M. Corradi, A. Di Schino, A. Borri, R. Rufini: Constr. Build. Mater., Vol. 181, 2018, p. 335
[9] A. Borri, M. Corradi, G. Castrori, A. Molinari: Constr. Build. Mater. Vol. 211, 2019, p. 594, https://doi.org/10.1016/j.conbuildmat.2019.03.197
[10] C. Gennari, M. Lago, B. Bögre, I. Mezaros, I. Calliari, L. Pezzato: Metals. Vol. 8, 2018, 1074; https://doi.org/0.3390/met8121074
[11] A. Di Schino, M. Longobardo, G. Porcu. G. Turconi, L. Scoppio: NACE – International Conference Series 2006, 062151-06125114
[12] A. Di Schino, M. Barteri, J.M. Kenny: Journal of Materials Science Letters, Vol. 22, 2003, p. 1511, https://doi.org/10.1023/A:1026155215111
[13] A. Di Schino, J.M. Kenny, M. Barteri: Journal of Materials Science Letters, Vol. 22, 2003, p. 691, https://doi.org/0.1023/A:1023675212900
[14] A. Di Schino: Acta Metallurgica Slovaca, Vol. 22, 2016, p. 266, https://doi.org/10.12776/ams.v22i4.815
[15] M. Talha, C.K. Behera, O.P. Sinha: Mater. Sci. Eng. C, Vol. 33(7), 2013, p. 3563, https://doi.org/0.1016/j.msec.2013.06.002
[16] Boulané- Petermann, L., Biofouling, Vol. 10(4), 1996, p. 275
[17] G. Bregliozzi, S.I.U. Ahmed, A. Di Schino, K.M. Kenny, H. Haefke: Tribol. Lett., Vol. 17, 2004, p. 697, https://doi.org/10.1007/s11249-004-8075-z
[18] A. Di Schino, L. Valentini, J.M. Kenny, Y. Gerbig, I. Ahmed, H. Haefke: Surf. Coat. Technol., Vol. 161, 2002, p. 224, https://doi.org/10.1016/S0257-8972(02)00557-1
[19] A. Di Schino, J.M. Kenny, G. Abbruzzese: J. Mater. Sci., Vol. 37, 2002, p. 5291, https://doi.org/10.1023/A:1021068806598
[20] A. Di Schino, J.M. Kenny, I. Salvatori, G. Abbruzzese: J. Mater. Sci. , Vol. 36, 2001, p. 593, https://doi.org/10.1023/A:1004856001632
[21] L. Valentini, A. Di Schino, J.M. Kenny, Y. Gerbig, H. Haefke: Wear , Vol. 253, 2002, p.458, https://doi.org/10.1016/S0043-1648(02)00140-0
[22] C Zitelli, P. Folgarait, A. Di Schino: Metals, Vol. 9, 2019, 731, https://doi.org/10.3390/met9070731
[23] Z. Brytan, M.A. Grande, M. Rosso, R. Bidulský, L.A. Dobrzański: Materials Science Forum, Vol. 672, 2011, p. 165, https://doi.org/10.4028/www.scientific.net/MSF.672.165
[24] T. Kvačkaj, L.Sokolová, M. Vlado, V. Vrchovinský: High Temperature Materials and Processes, Vol. 24, 2005, Issue 2, p. 139, https://doi.org/10.1515/HTMP.2005.24.2.139
[25] L. Parilak, E. Dudrova, R. Bidulsky, M. Kabatova: Powder Technology, Vol. 322, 2017, p. 447, https://doi.org/10.1016/j.powtec.2017.09.027
[26] C. Wang, M. Wang, J. Shi, H. Dong, H: Scripta Materialia, Vol. 58, 2008, p. 492, D https://doi.org/10.1016/j.scriptamat.2007.10.053

DOI 10.12776/ams.v25i4.1363 p-ISSN 1335-1532
e-ISSN 1338-1156

[27] S. Azuma, T. Kudo, H. Miyuki, M. Yamashita, H. Uchida: Corrosion Science, Vol. 46, 2004, p. 2265, https://doi.org/10.1016/j.corsci.2004.01.003
[28] J. N. Wanklyn: Corrosion Science, Vol. 21, 1981, p. 211, https://doi.org/10.1016/0010-938X(81)90031-7
[29] Y. Peng Y: Metals, Vol. 9, 2019, 723, https://doi.org/10.3390/met9070723
[30] B. Atzori, P. Lazzarin, G. Meneghetti, M. Ricotta: Int. J. Fatigue, Vol. 31, 2009, p. 59, https://doi.org/10.1016/j.ijfatigue.2008.02.013
[31] R. De Finis, D. Palumbo, F. Ancona, U. Galietti: Int. J. Fatigue, Vol. 74, 2015, p. 88, https://doi.org/0.1016/j.ijfatigue.2014.12.010

DOI 10.12776/ams.v25i4.1363 p-ISSN 1335-1532
e-ISSN 1338-1156

KINETIC ANALYSIS OF SECONDARY PRECIPITATION IN A HP40-Nb ALLOY

Matías Humberto Sosa Lissarrague [1), 2)], Alfredo Juan [2)], César Lanz [1)], Bruno La Rocca [3)], Alberto Picasso [1, 4)]*

[1)] Laboratorio de Metalurgia Tecnología Mecánica, Universidad Nacional del Sur, Departamento de Ingeniería, Av. L. N. Alem 1253, B8000CPB, Bahía Blanca, Argentina

[2)] IFISUR, Universidad Nacional del Sur, CONICET, Departamento de Física - UNS, Av. L. N. Alem 1253, B8000CPB, Bahía Blanca, Argentina

[3)] Becario del Consejo Interuniversitario Nacional (CIN)

[4)] Comisión de Investigaciones Científicas de la Provincia de Buenos Aires (CICPBA), Calle 526 entre 10 y 11, B1900, La Plata, Argentina

Received: 30.09.2019
Accepted: 27.11.2019

[*] Corresponding author: e-mail: mhsl1986@gmail.com, Tel.: +54 0291 4595179, Laboratorio de Metalurgia y Tecnología Mecánica, Universidad Nacional del Sur, Departamento de Ingeniería, Av. L. N. Alem 1253, B8000CPB, Bahía Blanca, Argentina

Abstract

The HP40-Nb heat resistant alloy (35Ni-25Cr-Nb) was analysed by means of optical microscopy after aging treatments at 1073 and 1173 K for different times, in order to apply the classic Johnson – Mehl - Avrami – Kolmogorov kinetic model (JMAK), and thus calculate the activation energy of secondary $M_{23}C_6$ precipitation, which occurs during thermal aging. The relevance of this theoretical analysis is to infer the mechanism that controls the nucleation and growth of $M_{23}C_6$ secondary carbides, since the amount and morphology of these phase influences the mechanical properties as well as the corrosion resistance in service. After performing the kinetic analysis using the JMAK model, the activation energy was found to be 208 kJ/mol, which would indicate that the secondary precipitation in this alloy is controlled by the Cr-diffusion phenomenon along the austenitic matrix.

Keywords: JMAK model, HP40-Nb, activation energy, $M_{23}C_6$ secondary carbide precipitation

1 Introduction

The HP40-Nb heat resistant alloy is widely used in pyrolysis furnaces due to its high corrosion resistance under high temperature service, which normally varies between 973 and 1273 K. The high content of alloy elements such as chromium and nickel, give it corrosion resistance under aggressive atmospheres during service. These alloys are manufactured by centrifugal casting, resulting in a dendritic-type microstructure due to the high solidification rate of the alloy during its manufacturing process. The austenitic matrix rich in nickel, chromium and iron, is strengthened by a network of primary carbides that increases its mechanical strength [1-11]. It is during the exposure of the alloy at high temperatures that precipitation of secondary Cr-rich carbides of $M_{23}C_6$ type occurs, whose nuclei begin to form in the vicinity of the primary eutectic Cr-rich $M_{23}C_6$ carbides and Nb-rich MC carbides network [7, 9, 12, 13]. Some authors have found for this heat resistant alloy that, in the as-cast condition, the primary carbides network is formed by Cr-rich M_7C_3 and Nb-rich MC carbides. Moreover, they have found that primary Cr-rich M_7C_3 carbides remains unalterable during aging [12, 14, 15]. $M_{23}C_6$ Cr-rich secondary precipitation

DOI 10.12776/ams.v25i4.1361 p-ISSN 1335-1532
e-ISSN 1338-1156

increases mechanical strength of the alloy when it operates at high temperatures that are characteristic of the pyrolysis production process. In this way, the mechanical properties are influenced by the volume fraction of secondary precipitation as well as its morphology and distribution along the matrix. However, excessive secondary precipitation leads on chromium depleted zones adjacent to the primary eutectic carbides network, since secondary precipitation causes chromium consumption in these areas, resulting in a decrease in resistance to oxidation at high temperature. Therefore, it is interesting to analyse the mechanism of precipitation, by kinetic models as the proposed by Johnson, Mehl, Avrami and Kolmogorov (JMAK model), that is widely used in the kinetic study of nucleation and growth reactions [10, 16-19]. In the present research work, it was found that the calculated activation energy of $M_{23}C_6$ secondary carbides was 208 kJ/mol, which is in good agreement with what was found in a similar analysis carried out on the refractory alloy 45Ni-35Cr-Nb [10] as well as with others research works [10,16,17].

2 Experimental

Chemical composition of HP40-Nb heat resistant alloy is shown in **Table 1**.

Table 1 Chemical composition of centrifugally cast alloy HP40-Nb [wt %].

C	Si	Mn	Cr	Ni	Nb	W	Ti	Fe
0.57	2.73	0.76	23.7	37.6	1.26	0.19	0.07	Balance

These alloys are produced as centrifugally cast tubes, with a 110 mm diameter and 11 mm wall thickness. From an as cast tube were cut several rings of 10 mm-thick of which, in turn, 10x10x11 mm samples were obtained.

Aging heat treatment was made at 1073 and 1173 K using resistive furnaces in air atmosphere. For each temperature, aging times were of 1, 5, 15 and 30 min, and 1, 3, 8, 16, 24 and 27 h. After aging, each specimen was cooled in air. The aging heat treatments were all carried out in the same oven, which has a standardized and previously calibrated S-type thermocouple, which guarantees an accuracy of 1 K. The measurement joint is adjacent to the sample to improve the quality of the measurement. Once each sample was introduced into the oven at the desired temperature, the aging time began to be counted when the thermocouple reached the previously set temperature. Metallographic preparation was done using different abrasive papers, each of them of decreasing particle size. Then, mechanical polishing was carried out with 1μm granulometry alumina. Since the high corrosion resistance of this alloys, electrolytic etching is recommended for optimal observation of it microstructure. For this purpose etching was done on each sample using 10% v/v KOH aqueous solution at an etching potential of 2 V for 14 s. Etching parameters were adjusted to achieve an optimal contrast between matrix and $M_{23}C_6$ secondary carbides, and thus facilitating the later quantitative analysis. Optical micrographs were taken using a Leica DM ILM optical microscope with a DFC 295CCD camera. On each sample, 5 micrographs of 1000X magnification were taken for make the quantitative analysis. Finally, area fraction of secondary carbides was measured by image analysis using ImageJ software version 1.41, developed by National Institutes of Health in the United States of America. The measurement method of this software is based on the contrast between particles and the background. In this way, the program calculates the ratio between the total area of the particles and the area of the micrograph, that is, the area fraction of the particles which, in the case of this work, are the secondary $M_{23}C_6$ carbides. In each optical micrograph, using Adobe Photoshop CC 2017 image processing software developed by Adobe Systems Incorporated in the United States of America, both the primary eutectic carbides and the

DOI 10.12776/ams.v25i4.1361 p-ISSN 1335-1532
e-ISSN 1338-1156

background corresponding to the austenitic matrix were suppressed to improve the contrast and not to consider the measurement of primary carbides.

3 Results and discussion

As an example, in **Fig. 1** to **Fig. 4** it is shown, for each temperature, some optical micrographs for some aging times, which were used to measure the fraction in the area of secondary carbides oh HP40-Nb alloy.

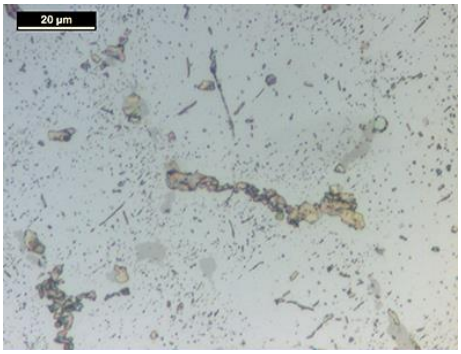

Fig. 1 Sample aged at 1073 K for 1 h

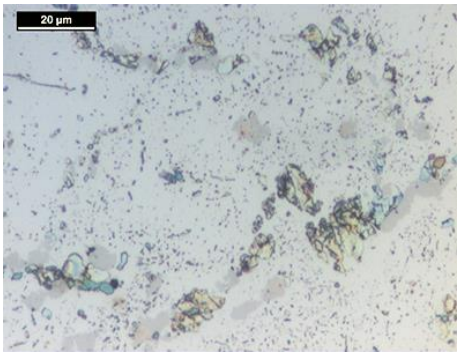

Fig. 2 Sample aged at 1073 K for 8 h

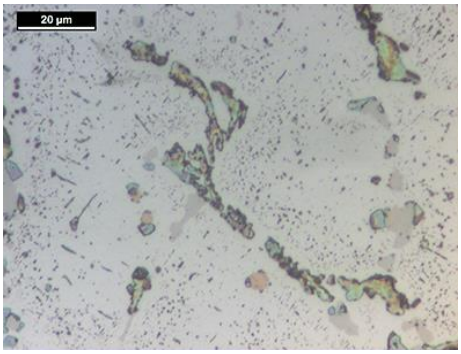

Fig. 3 Sample aged at 1173 K for 1 h

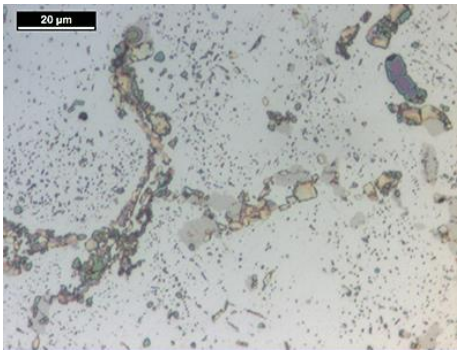

Fig. 4 Sample aged at 1173 K for 8 h

The dendritic type microstructure can be appreciated, as well as the network of primary eutectic carbides rich in Cr and Nb. In turn, secondary precipitation is observed, the amount of which as a function of time at the same temperature.

Applying JMAK model for an isothermal analysis, it can be obtained the transformed fraction of a certain phase, f, as a function of time. The model is exactly accurate for nucleation and growth reactions with linear growth, while it is a good approximation in cases of nucleation and growth with parabolic growth, i.e. as in the case of diffusion-controlled growth, if several hypotheses are met: random distribution of the precipitated phase, isotropic growth, uniform average growth rate throughout microstructure, the amount of a phase that can be transformed is independent of time, etc. [19-22]. In this case, secondary $M_{23}C_6$ precipitation is a thermally activated phenomenon controlled by diffusion.

The Avrami equation, relates the transformed fraction with aging time by:

$$f = 1 - \exp(-k.t)^n \quad (1.)$$

DOI 10.12776/ams.v25i4.1361 p-ISSN 1335-1532
e-ISSN 1338-1156

where: f - area fraction of secondary carbides
n - Avrami exponent
k [s-1] - pre-exponential factor
t [s] - aging time

The pre-exponential factor, k, is defined by an Arrhenius-type equation as:

$$k = k_0 . \exp\left(-\frac{Q}{R.T}\right) \quad (2.)$$

where: k_0 [s^{-1}] - constant
Q [kJ/mol] - activation energy of deformation
R [kJ/(K·mol)] - universal gas constant
T [K] - temperature

From the Avrami equation, it is possible to obtain a straight line function of slope n and intercept n.ln(k), which is plotted in **Fig. 5**, as a function of ln(t) for each aging temperature.

$$\ln(-\ln(1-f)) = n.\ln(t) + n.\ln(k) \quad (3.)$$

For 1073 K, the equation of the fitting function is:

$$\ln(-\ln(1-f)) = 0{,}88.\ln(t) - 8{,}72 \quad (4.)$$

In such a way, for 1173 K, the equation is:

$$\ln(-\ln(1-f)) = 0{,}79.\ln(t) - 6{,}73 \quad (5.)$$

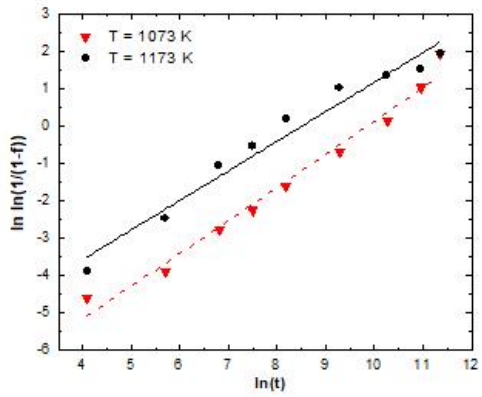

Fig. 5 Linear adjustment using the Avrami equation vs. aging time

The kinetic evolution of secondary carbides precipitation was characterized by occurs in a single step, which is in good agreement with other researches based on this kinetic model [10, 17]. On the other hand, other authors have found in similar alloys that this reaction occurs, in two steps [16]. Once the kinetic parameters of the Avrami equation have been calculated for each aging temperature, it is possible to compare these results with the experimental data of the transformed fraction, as it is shown in **Fig. 6**.

DOI 10.12776/ams.v25i4.1361 p-ISSN 1335-1532
e-ISSN 1338-1156

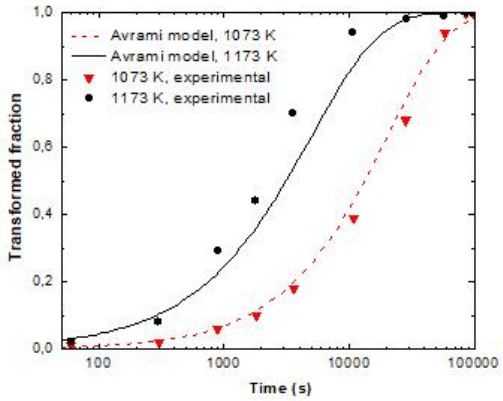

Fig. 6 Evolution of the experimental and calculated transformed fraction vs. aging time

Finally, the activation energy value of secondary precipitation, can be calculated by plotting n.ln(k) as a function of $(R.T)^{-1}$ (see **Fig. 7**), resulting in a linear function defined by the slope Q and intercept $\ln(k_0)$ and expressed with the following equation:

$$\ln(k) = \ln(k_0) - \frac{Q}{R.T} \rightarrow \ln(k) = 14{,}62 - \frac{208}{R.T} \quad (6.)$$

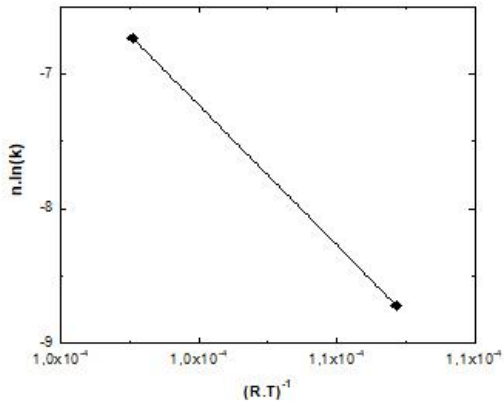

Fig. 7 Evolution of n.ln(k) vs. $(R.T)^{-1}$ in order to calculate the activation energy

In this way, the calculated activation energy Q of secondary $M_{23}C_6$ carbides precipitation is 208 kJ/mol and k_0 is $2{,}23 \times 10^6$ s^{-1}. This value of Q, allows to identify the mechanism that controls the precipitation of Cr-rich $M_{23}C_6$ carbides. In this case, as it is a phenomenon assisted by diffusion, it is important to know the activation energy for self-diffusion of C and Cr atoms. In the case of C, the self-diffusion energy in an austenitic matrix is of 142 kJ/mol [23] while some authors have found by JMAL kinetic analysis, an activation energy of 213 kJ/mol for a Fe-30.8Ni-26.6Cr alloy [16] and of 195 kJ/mol for a 45Ni-35Cr-Nb alloy [10]. As it can be seen, the calculated activation energy from JMAK model for a HP40-Nb heat resistant alloy would indicate that the mechanism

DOI 10.12776/ams.v25i4.1361 p-ISSN 1335-1532
e-ISSN 1338-1156

that controls the secondary precipitation is the diffusion of the Cr atom through the austenitic matrix.

4 Conclusions

After applying the classic Johnson-Mehl-Avrami-Kolmogorov kinetic model in order to describe the secondary precipitation reaction in a HP40-Nb heat resistant alloys, several conclusions can be enumerated. First, it was found that the phenomenon occurs in a single stage, and the calculated activation energy of $M_{23}C_6$ secondary precipitation was 208 kJ/mol. Moreover, this value is comparable to that corresponding to the self-diffusion of Cr in an austenitic matrix of Ni-Cr-Fe alloys. For this reason, the diffusion of Cr through the austenitic matrix would be the mechanism that controls the formation of $M_{23}C_6$-type secondary Cr-rich carbides. Finally, the Avrami exponent value has very low variation with aging temperature.

References

[1] A. Picasso, C. Lanz, M. Sosa Lissarrague, A. Garófoli: Journal of Minerals and Materials Characterization and Engineering, Vol. 4, 2016, p. 48-61, https://doi.org/10.4236/jmmce.2016.41006

[2] R. Song, S. Wu: Engineering Failure Analysis, Vol. 88, 2018, p. 63-72, https://doi.org/10.1016/j.engfailanal.2018.01.002

[3] I. Sustaita Torres et al.: Materials Chemistry and Physics, Vol. 133, 2012, p. 1018-1023, https://doi.org/10.1016/j.matchemphys.2012.02.010

[4] A. Reihani, R. Derakhshandeh Haghighi: Engineering Failure Analysis, Vol. 52, 2015, p. 97-108, https://doi.org/10.1016/j.engfailanal.2015.03.005

[5] K. Buchaman, M. Kral, C. Bishop: Metallurgical and Materials Transactions A, Vol. 45, 2014, p. 3373–3385, https://doi.org/10.1007/s11661-014-2285-2

[6] M. Attarian, A. Karimi Taheri: Materials Science & Engineering A, Vol. 659, 2016, p. 104-118, https://doi.org/10.1016/j.msea.2016.02.046

[7] MR. Andrade, C. Bolfarini, LAM. Ferreira, CD. Souza Filho, LHC. Bonazzi: Materials Science & Engineering A, Vol. 636, 2015, p. 48-52, https://doi.org/10.1016/j.msea.2015.03.085

[8] CJ. Liu, Y. Chen: Materials and Design, Vol. 32, 2011, p. 2507-2512, https://doi.org/10.1016/j.matdes.2010.08.031

[9] MH. Sosa Lissarrague, S. Limandri, F. Prado, AC. Picasso: Metallography, Microstructure, and Analysis, Vol. 7, 2018, No. 3, p. 356-362, https://doi.org/10.1007/s13632-018-0448-z

[10] MH. Sosa Lissarrague, A. Sepúlveda Buitrago, A. Picasso: Acta Metallurgica Slovaca, Vol. 25, 2019, No. 3, p. 180-185, https://doi.org/10.12776/ams.v25i3.1312

[11] J. Guo, T. Cao, C. Cheng, X. Meng, J. Zhao: Microscopy and Microanalysis, Vol. 24, 2018, p. 478-487, https://doi.org/10.1017/S1431927618015180

[12] AR. Andrade et al.: Materials Science & Engineering A, Vol. 628, 2015, p. 176-180, https://doi.org/10.1016/j.msea.2015.01.049

[13] F. Tancret, J. Laigo, J. Furtado: Materials Science and Technology, Vol. 35, 2019, No. 3, p. 1924-1931, https://doi.org/10.1080/02670836.2019.1648371

[14] IA. Sustaita Torres, S. Haro Rodriguez, R. Colás: High Temperature Materials Proceedia, Vol. 37, 2018, No. 2, p.133-139, https://doi.org/10.1515/htmp-2016-0112

[15] R. Ortega Reyes, S. Haro Rodriguez, IA. Sustaita Torres, FA. Pérez González, R. Colás: Ingenierías, Vol. 22, 2019, No. 82, p. 22-32

[16] G. Lothongkum, S. Ratanamahasakul, P. Wangyao: Acta Metallurgica Slovaca, Vol. 11, 2005, No. 1, p. 54-61
[17] A. Baltušnikas, I. Lukošiūtė, V. Makarevičius, R. Kriūkienė, A. Grybėnas: Journal of Materials Engineering and Performance, Vol. 25, 2016, No. 5, p. 1945-1951, https://doi.org/10.1007/s11665-016-2002-y
[18] R. Badji et al.: Materials Chemistry and Physics, Vol. 148, 2014, p. 664-672, https://doi.org/10.1016/j.matchemphys.2014.08.032
[19] MJ. Starink: Journal of Materials Science, Vol. 36, 2001, No. 18, p. 4433-4441, https://doi.org/10.1023/A:1017974517877
[20] F. Liu, F. Sommer, C. Bos, EJ. Mittemeijer: International Materials Reviews, Vol. 52, 2007, No. 4, p. 193–212, https://doi.org/10.1179/174328007X160308
[21] J. Xu, F. Liu, S. Song, K. Zhang: Journal of non-Crystalline solids, Vol. 356, 2010, p. 1236-1245, https://doi.org/10.1016/j.jnoncrysol.2010.04.034
[22] ATW. Kempen, F. Sommer, EJ. Mittemeijer: Journal of Materials Science, Vol. 37, 2002, No. 7, p. 1321-1332, https://doi.org/10.1023/A:1014556109351
[23] W. Smith, J. Hashemi: *Fundamentos de la ciencia e ingeniería de materiales*, fifth ed., Mc-Graw Hill, Mexico, 2014

Acknowledgements

This work was partially supported by IFISUR-CONICET, by Laboratorio de Metalurgia y Tecnología Mecánica of Departamento de Ingeniería (UNS) and Comisión de Investigaciones Científicas de la Provincia de Buenos Aires (CICPBA). In addition, the authors wish to acknowledge to Consejo Interuniversitario Nacional (CIN)

DIFFUSIVE AND DISPLACIVE PHASE TRANSFORMATIONS UNDER HIGH PRESSURE TORSION

Boris Straumal[1),2),3)], Askar Kilmametov[1), 3)], Andrey Mazilkin[1),3)], Olga Kogtenkova[1)], Brigitte Baretzky[3)], Anna Korneva[4)], Pawel Zięba[4)]*

[1]*Institute of Solid State Physics and Cheronogolovka Scientific Center of RAS, Chernogolovka, Russia*

[2]*National University of Science and Technology «MISIS», Moscow, Russia*

[3]*Karlsruhe Institute of Technology, Institute of Nanotechnology, Eggenstein-Leopoldshafen, Germany*

[4]*Institute of Metallurgy and Materials Science, Polish Academy of Sciences, 25 Reymonta Street, 30-059 Cracow, Poland*

Received: 12.08.2019
Accepted: 02.12.2019

[*]*Corresponding author: straumal@issp.ac.ru, Tel.: +7 9166768673, Institute of Solid State Physics RAS, Ac, Ossipyan str. 2, 142432 Chernogolovka, Russia*

Abstract

Severe plastic deformation (SPD) can induce various phase transformations. After a certain strain, the dynamic equilibrium establishes between defects production by an external force and their relaxation (annihilation). The grain size, hardness, phase composition etc. in this steady-state does not depend on the initial state of a material and is, therefore, equifinal. In this review we discuss the competition between precipitation and dissolution of precipitates, amorphization and (nano)crystallization, SPD-induced accelerated mass-transfer, allotropic and martensitic transitions and formation of grain boundary phases.

Keywords: severe plastic deformation, phase transformations, thermodynamics, kinetics

1 Introduction

Severe plastic deformation (SPD) is a novel class of mechanical treatment which permits to apply a very high strain to the material without its failure, which is not possible with traditional methods. SPD always leads to strong grain refinement or even to amorphization of a material. At the same time, SPD can drive the phase transformations [1–6]. In other words the phases in a material before and after SPD can be different. Frequently, after SPD a material contains such phases as if it was annealed at elevated temperature and then quickly quenched [3]. Thus, SPD opens completely new ways for tailoring microstructure and properties of materials. The understanding of SPD-driven phase transformations is the topic of this review.

2 Steady-state during SPD

The important feature of SPD is that the sample cannot break during straining, and its shape remains more or less unchanged. It is especially well pronounced in case of high pressure torsion (HPT). The small disk between two anvils conserves its shape independently on number of anvils rotations. The torsion can continue until the anvils (typically made of WC-Co alloy) break. For example, in case of HPT of Nd-Fe-B alloys the anvils withstand only about 20 rotations [7, 8] but

DOI 10.12776/ams.v25i4.1368 p-ISSN 1335-1532
e-ISSN 1338-1156

in case of soft aluminium-, magnesium- or copper-based alloys HPT can continue up to hundreds or even thousands anvil rotations [9–13]. When the straining starts, the amount of lattice defects (like vacancies, dislocations, grain boundaries) expectedly increases. However, it would be strange to anticipate that the number of defects would increase infinitely during endless anvil rotations. Even if the HPT proceeds at room temperature when the coefficients of bulk diffusion are below 10^{-30}-10^{-40} m^2/s, the relaxation starts. Its rate increases with increasing concentration of defects until the dynamic equilibrium establishes. In other words, the rate of defects production becomes equal to the rate of their annihilation (relaxation). Here it is appropriate to mention that usually HPT (and generally SPD) takes place at room temperature and the samples are almost not heated during HPT [14, 15]. After HPT treatment they are usually just a little bit warm. The direct temperature measurements between anvils witness that the temperature during SPD does not exceed about 40°C [16, 17].

Thus, after a certain number of anvil rotations, the rate of defects production becomes equal to the rate of their annihilation (relaxation) and the steady-state is reached [5, 18]. The easiest way to observe it is to measure the torsion torque during HPT. It increases during the transient stage, but quickly saturates after 1-1.5 rotations in case of Al-, Cu-, Mg- or even Ti-based alloys [1, 5, 13, 16, 19]. In case of harder alloys like Nd-Fe-B the torsion torques saturates after 2-2.5 anvil rotations [5, 7, 8]. Not only torsion torque, but also the values of the properties or structural parameters saturate in the steady state. For example, the most prominent feature of SPD is the grain refinement [13, 20–25]. If one starts to deform the material with grain size of several millimetres, it quickly decreases down to few hundreds of nanometers. Then, the grain size reaches the steady-state value, stabilises and does not decrease anymore [17, 26–29]. In the same material, the steady-state grain size depends first of all on the SPD mode. For example, the smallest grain size in copper and copper-based alloys of about 15 nm is reached by the ball milling (**Fig. 1**) [30]. The second strongest grain refiner is HPT [1, 31–36]. This is followed by planar twist channel angular extrusion (PTCAE) [37], equal channel angular pressing (ECAP) [34, 38], equal channel angular pressing with the subsequent HPT (ECAP+HPT) [34], equal channel angular pressing with following cold rolling (ECAP + CR) [39], simple shear extrusion (SSE) [40, 41], and constrained groove pressing (CGP) [42]. Same tendency is true also for aluminium and its alloys [43]. The steady-state grain size is also the function of HPT pressure, strain rate and temperature [5, 18]. It decreases with increasing melting temperature, atomic bond energy, specific heat capacity and activation energy for self-diffusion [18, 44]. One has to underline that the grain size in the dynamic equilibrium is a real steady-state value. It means that it is reached not only "from the top" but also "from the bottom". In other words, if one starts HPT of steel from the coarse-grained sample, one quickly reaches the grain size of 15-20 nm [28, 45–51] (**Fig. 2**). However, if one starts to deform the nanocrystalline steel sample with grain size of 10 nm produced by mechanical alloying, the grains do not become smaller. To the contrary, they grow during SPD up to the same steady-state value of 15-20 nm (**Fig. 2**) [9]. Similar phenomenon was observed also in nickel [52, 53] and copper [54].

Together with observation of grain refinement, a huge amount of experimental data is collected on the Vickers microhardness during and after SPD of copper, aluminium, titanium, magnesium alloys, steels etc. [10, 17, 29, 55–67]. Usually microhardness increases during SPD [10, 17, 29, 55–67]. It correlates also with tensile strength [13, 24, 25, 57, 60, 68–70]. It is true not only for rotation angle for HPT but also for number of passes during equal channel angular pressing (ECAP) [62]. The main mechanism here is the Hall-Petch hardening due to the grain refinement

DOI 10.12776/ams.v25i4.1368 p-ISSN 1335-1532
e-ISSN 1338-1156

[71]. Few exclusions only support this fact. For example, in Al–Zn alloys the Hall-Petch hardening competes with softening driven by the decomposition of (Al) solid solution, and after HPT the alloy is softer than before HPT (**Fig. 3**) [31, 56, 72, 73]. Similar to the grain size, the hardness value is also a function of material and SPD mode. So, by the increase of the purity of aluminium, one observes the transition from hardening to softening during HPT [74]. Thus, when the initial hardness of an alloy is higher than the steady-state one, then softening rather than hardening is observed during SPD [72].

The decrease of grain size and increase of Vickers microhardness after HPT, ECAP and alternating roll bonding (ARB) correlates with increase of electrical resistivity of copper [62]. It is important to underline that different properties (grain size, hardness, torsion torque, lattice parameter, resistivity etc.) reach steady state not at the same time.

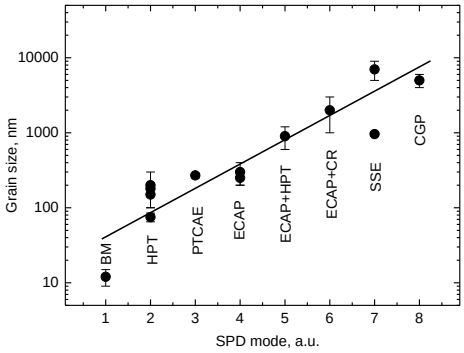

Fig. 1 Steady-state grain size in copper subjected to the different SPD modes: 1 – Ball milling (BM) [30], 2 – High pressure torsion (HPT) [1, 31–36], 3 – Planar twist channel angular extrusion (PTCAE) [37], 4 – Equal channel angular pressing (ECAP) [34, 38], 5 – ECAP+HPT [34], 6 – Equal channel angular pressing with following cold rolling (ECAP + CR) [39], 7 – Simple shear extrusion (SSE) [40, 41], 8 – Constrained groove pressing (CGP) [42]

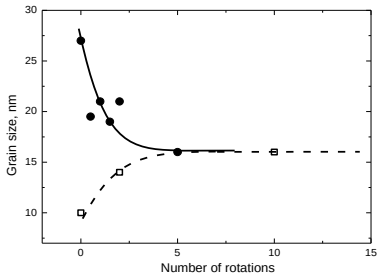

Fig. 2 Grain size plotted vs. number of torsions for pure coarse-grained steel sample (filled circles) [46] and nanocrystalline steel produced by mechanical alloying (open squares) [9]

3 Competition between dissolution of precipitates and decomposition of supersaturated solid solution

It has been long time generally believed that SPD always leads to the grain refinement [23, 75] and to the dissolution of precipitates and formation of supersaturated solid solution. However, we demonstrated above that the grain size decreased during SPD only in the case if the grains in the initial sample before SPD are larger than those in the steady-state. If the grains before SPD are smaller than in the steady state, they will grow during the deformation and reach the same steady-state grain size "from below" (see **Fig. 2**). This is true also for the SPD-induced

DOI 10.12776/ams.v25i4.1368 p-ISSN 1335-1532
e-ISSN 1338-1156

hardening/softening (see **Fig. 3**). Similar is the situation with dissolution/precipitation process. In the steady-state during SPD a certain concentration in the solid solution c_{ss} establishes. Its value is controlled by the dynamic equilibrium between competing dissolution and precipitation. If the initial concentration in a solid solution c_{init} is below c_{ss}, it increases during SPD and precipitates dissolve. Otherwise, if $c_{init} > c_{ss}$, the concentration of second component in a solid solution decreases and new precipitates appear (so-called dynamic ageing). For the first time such dynamic ageing has been observed in Al–Zn alloys [73]. Now it is an established topic for investigations and the instrument for the tailoring the properties of materials [76]. Below, the decomposition of the solid solution in all discussed cases leads to the formation of small particles of the second phase (i.e. to precipitation). Therefore, for this discussion we use the terms "decomposition" and "precipitation" as synonyms.

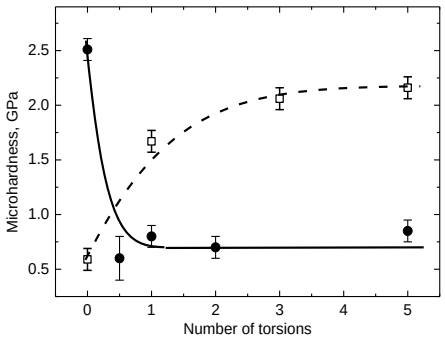

Fig. 3 Vickers microhardness plotted vs. number of torsions for pure Al–30 wt. % Zn (filled circles) [31] and Al– 8.8 wt. % Mg alloys (open squares) [55]

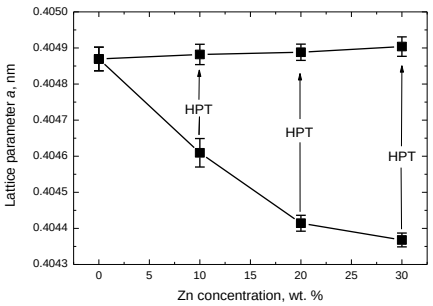

Fig. 4 Dependence of the lattice parameter in aluminium matrix on the total zinc concentration in the Al–Zn alloys before and after HPT [73]

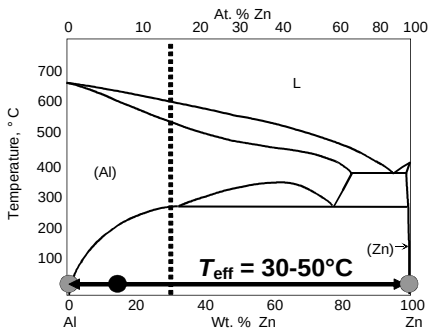

Fig. 5 Al–Zn phase diagram. Vertical dotted line shows the composition of Al–30 wt. % Zn alloy. Large black circle shows the composition of supersaturated (Al) solid solution in coarse-grained Al– 30 wt. % Zn alloy before HPT (it contained 15 wt. % Zn). Large grey circles show the composition of phases in ultra-fine-grained Al– 30 wt. % Zn alloy after HPT [73]. The value of T_{eff} = 30-50°C is also given

DOI 10.12776/ams.v25i4.1368 p-ISSN 1335-1532
e-ISSN 1338-1156

The as-cast Al–Zn alloys were subjected to HPT at 5 turns, 5 GPa and 1 rpm [73]. The coarse-grained supersaturated solid solution (Al) in the as-cast Al–30 wt. % Zn alloy contained about 15 wt.% Zn. Zn concentration in the solid solution for Al–20 wt. % Zn and Al–10 wt. % Zn alloys (measured locally by the electron-probe microanalysis) was 7 and 3 wt.% Zn, correspondingly. In **Fig. 4** the respective values for the lattice parameter in (Al) are given, they are well below the lattice parameter in pure aluminium. The HPT at room temperature produced nanograined pure Al and pure Zn particles [20, 73]. The supersaturated solid solution also completely decomposed, and the lattice parameter in all three alloys became non-distinguishable from that of pure aluminium (**Fig. 4**). The composition of the solid solutions in Al– 30 wt. % Zn before and after the HPT is shown by black and grey circles in **Fig. 5** correspondingly. The decomposition during SPD proceeds extremely quickly. Already after about 0.5 rotations of anvils the lattice spacing becomes equal to that of Al and microhardness reaches its steady-state value [73].

The competition between dissolution of precipitates and decomposition of supersaturated solid solution has been studied in details for the binary copper alloys [6]. Physically, it is the steady-state concentration in the solid solution c_{ss} which establishes during SPD. However, in order to compare different binary alloys with different maximal solubilities of a second component, an idea of a so-called effective temperature T_{eff} is very useful. Thus, after SPD the concentration c_{ss} of a second component in the matrix solid solution is as high as if the sample has been annealed at a certain (elevated) temperature T_{eff}. In other words, c_{ss} is equal to the solubility of a second component at T_{eff}. The solubility is defined by the solvus line in the equilibrium binary phase diagram.

Consider the example of competition between dissolution and precipitation in Cu–Co system [32, 77, 78]. The as cast Cu– 4.9 wt. % Co alloy contained grains of Cu-based solid solution (with grain size 10-20 μm), Co particles with size about 2 μm and fine dispersed Co precipitates with a size about 10-20 nm [32, 77, 78]. Cobalt fully dissolved in copper matrix after annealing at 1060°C for 10 h (sample 2). The grain size after this annealing was about 50 μm. During annealing at 570°C for 840 h (sample 1), the Cu-based solid solution almost fully decomposed: less than 0.5 wt. % Co remained dissolved in Cu (based on XRD measurements and phase diagram [29]).

After HPT of both samples the Cu grain size drastically decreased to about 200 nm, and that of Co-precipitates to only 10-20 nm (insets in **Fig. 6**). The lattice parameter of Sample 1 before deformation is very close to that of pure copper (diamond in **Fig. 6**). With an increasing number of rotations, the lattice parameter of Sample 1 decreased and that of Sample 2 increased. After 5 anvil rotations (1800 deg.) the lattice parameter in both samples becomes almost undistinguishable and corresponds to the solid solution of Co in Cu with nearly 2.5 wt.%. In other words, the composition of the solid solution in the Cu – 4.9 wt. % Co alloy after HPT does not depend on the initial state prior to HPT. This is a so-called *equifinal composition* $c_{eq} \approx 2.5$ wt. % Co. Thus, the steady-state with respect to the grain size, size of Co precipitates, torsion torque and concentration of Co in a solid solution during HPT is indeed *equifinal*. The composition of Cu-rich matrix in both alloys before and after HPT is shown in the Cu–Co phase diagram (**Fig. 7**). The solid solution in samples 1 and 2 after HPT contains as much Co $c_{eq} \approx 2.5$ wt. % Co, as if they would be annealed at $T_{eff1} = 920 \pm 30$°C and $T_{eff2} = 870 \pm 30$°C, respectively.

Here the analogy appears between thermodynamic *equilibrium* when the composition of phases does not depend on the starting state and *equifinality* when the composition of phases in a steady-state during SPD also does not depend on the phases in a starting state. The values like equivalent (effective) temperature T_{eff} and steady-state (equifinal) composition of solid solution c_{eq} are frequently called attractors in the thermodynamics of non-equlibrium (or open) systems [79].

DOI 10.12776/ams.v25i4.1368 p-ISSN 1335-1532
e-ISSN 1338-1156

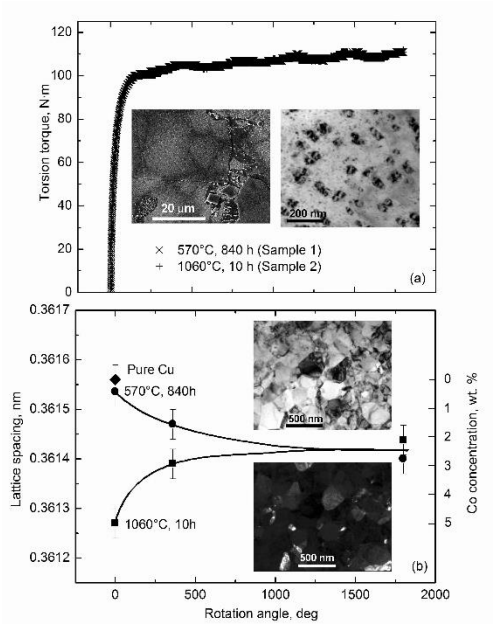

Fig. 6 (a) Dependence of torsion torque on the rotation angle. Insets: SEM (left) and bright-field TEM (right) micrographs of Cu– 4.9 wt. % Co alloy after annealing at 570°C for 840 h. (b) Dependence of lattice spacing on the rotation angle. Circles mark the lattice spacing in Sample 1 annealed at 570°C for 840 h. Squares correspond to the Sample 2 annealed at 1060°C for 10 h. Diamond shows the lattice spacing for pure copper. The respective Co concentration is shown on the right vertical axis, $c_{eq} \approx 2.5$ wt. % Co. Insets: Bright-field (top) and dark-field (bottom) TEM micrographs of Cu– 4.9 wt. % Co alloy after annealing at 570°C for 840 h and HPT (6 GPa, 5 rot, 1 rpm) [32]

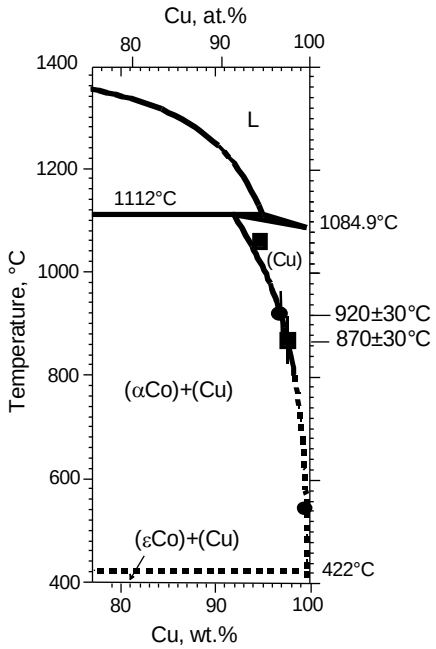

Fig. 7 The Cu-rich part of the Co–Cu phase diagram [29]. The composition of Cu-rich matrix in both alloys before and after HPT is shown. Circles mark the data for Sample 1 annealed before HPT at 570°C. Squares correspond to the Sample 2 annealed before HPT at 1060°C [31]. Steady-state (equifinal) composition of solid solution c_{eq} is about 2.5 wt. % C [32]

In [6] the values of T_{eff} were compared for several Cu-based alloys Cu–Ni [80], Cu–Co [32, 77, 78], Cu–Sn [81–83], Cu–In [84, 85], Cu–Cr [86], Cu–Ag [87–89], Cu–Al–Ni [90, 91] Cu–Hf [6] (**Fig. 8**). The T_{eff} linearly increases with increase of activation enthalpy of bulk tracer diffusion H_D. The correlation between activation enthalpy of bulk tracer diffusion H_D and melting

DOI 10.12776/ams.v25i4.1368 p-ISSN 1335-1532
e-ISSN 1338-1156

temperature T_m of diffusing alloying component also has been found. As a result, T_{eff} linearly increases with increase of melting temperature T_m of diffusing alloying component as well. The observed correlations allow one to predict the behaviour and phase transitions in the Cu-based alloys under high pressure torsion.

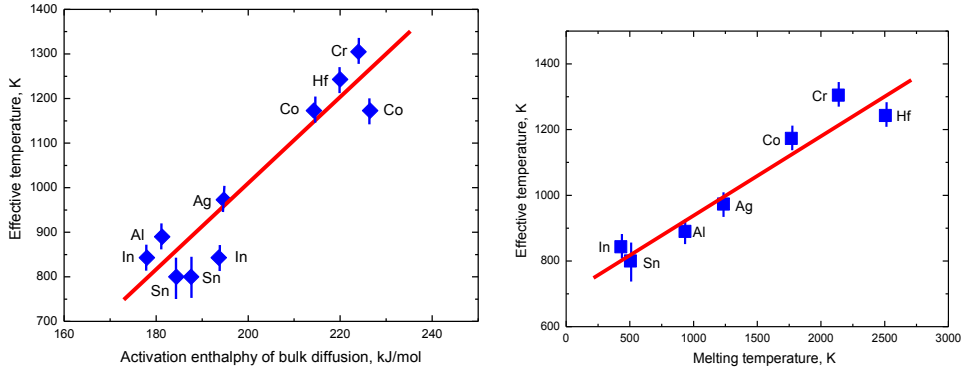

Fig. 8 (a) Dependence between effective temperature of HPT treatment T_{eff} of copper-based solid solutions and activation enthalpy of bulk tracer diffusion H_D of alloying element [6]. (b) Correlation between effective temperature T_{eff} and melting temperature T_m of alloying element in various Cu-based alloys. The values of H_D and T_m were taken from the handbook [85]

4 Amorphization and nanocrystalisation

SPD produces high amount of defects, thus the material is very far from equilibrium during SPD. Nevertheless, one can *use the equilibrium phase diagrams* as an instrument for the description of *phase transformations in the non-equilibrium conditions.* This idea goes back to the work of Georges Martin who developed it for the description of phase transformations under strong irradiation [92]. His main idea was that the forced mixing induced by irradiation emulates the increase of entropy and changes the thermodynamic potentials in the alloy. The equilibrium configuration of the solid under irradiation flux φ at temperature T is identical to the configuration at φ = 0 and a certain effective temperature T_{eff}:

$$T_{eff} = T(1+\Delta) \quad (1.)$$

If the irradiation-driven movements of atoms are similar in amplitude to conventional diffusion jumps, they can be described by the "ballistic" diffusion coefficient D_{ball} and $\Delta = D_{ball}/D_b$, where D_b is conventional bulk diffusion coefficient, possibly increased due to the non-equilibrium defect concentration [92]. It means that one can use the equilibrium phase diagram for the description of the system under irradiation, but at T_{eff} instead of the actual temperature T. For example, if the liquid phase is present in the phase diagram at T_{eff}, the amorphous phase would appear under irradiation [92]. Thus, G. Martin proposed to find a temperature T_{eff} (usually called effective temperature) in an equilibrium phase diagram where the given phase appears under irradiation. The composition of phases after SPD allows to localize those phases in the respective equilibrium phase diagram and to estimate the effective temperature T_{eff}. Such a schematic diagram is shown in **Fig. 9**. We already used this idea for description of the SPD influence (see Section 3). In our case we use the value of D_{HPT} for the diffusion-like mass-transfer induced by HPT instead of D_{ball}.

DOI 10.12776/ams.v25i4.1368 p-ISSN 1335-1532
e-ISSN 1338-1156

The obvious example for the T_{eff} approach is the amorphization. Let us consider first the HPT of Nb–Ni–Y alloys [93, 94]. The coarse-grained as-cast Ni–20 wt.% Nb–30 wt.% Y and Ni–18 wt.% Nb–22 wt.% Y alloys contained before high pressure torsion (HPT) the NiY, $NbNi_3$, Ni_2Y, Ni_7Y_2 and Ni_3Y phases (point *g*, **Fig. 9**) (**Fig. 10a**) [95, 96]. After HPT these alloys transformed into a mixture of two nanocrystalline NiY and $Nb_{15}Ni_2$ phases and two different amorphous phases (one was Y-rich and another Nb-rich) (point 6, **Fig. 9**). The Ni–Nb–Y phase diagram contains two immiscible melts above 1440°C (**Fig. 10a**) [96]. Therefore, the effective temperature is slightly above T_e = 1440°C and can be estimated as T_{eff} = 1450°C (**Fig. 10a**). It is remarkable that the rapid solidification of these alloys from the liquid state (point *f*, **Fig. 9**) also allows obtaining the mixture of two amorphous phases.

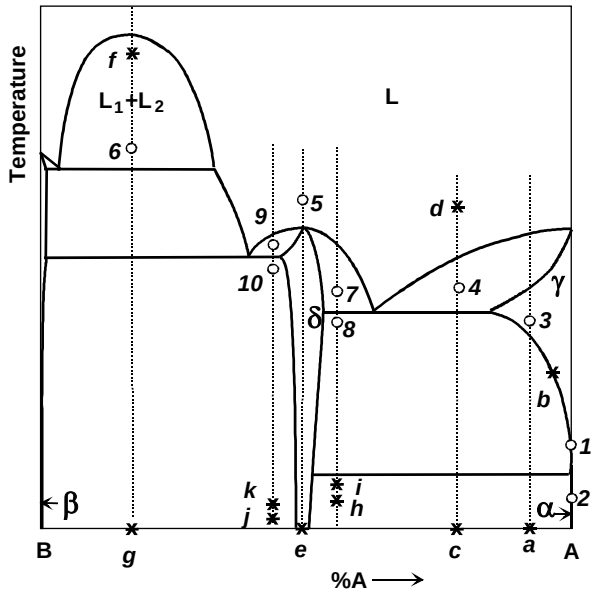

Fig. 9 The schematic binary phase diagram showing the points of HPT deformation or other thermal treatments (stars) and respective configuration points at the (increased) effective temperatures. The dashed vertical lines denote compositions of various alloys. Figurative points corresponding to the effective temperature of the alloys are indicated by an open circle and numbered. Each star point with a letter indicates the composition and temperature of an alloy's treatment (normal cooling, SPD or rapid quenching)

In [7, 8] the HPT has been used for the treatment of liquid-phase sintered hard magnetic NdFeB-based alloy (5 GPa, 1 rpm, 5 rot, ambient temperature). The amorphization of the crystalline alloy took place under the action of HPT. This permitted to obtain for the first time the mixture of two different amorphous phases with embedded grains of the ferromagnetic $Nd_2Fe_{14}B$ phase. The SPD-treatment at ambient temperature T_{SPD} = 300 K is frequently equivalent to the heat treatment at a certain elevated temperature T_{eff} > 300 K. The composition of phases in the studied NdFeB-based alloy after HPT corresponds to the state at T_{eff} ~1170°C (**Fig. 11**).

DOI 10.12776/ams.v25i4.1368 p-ISSN 1335-1532
e-ISSN 1338-1156

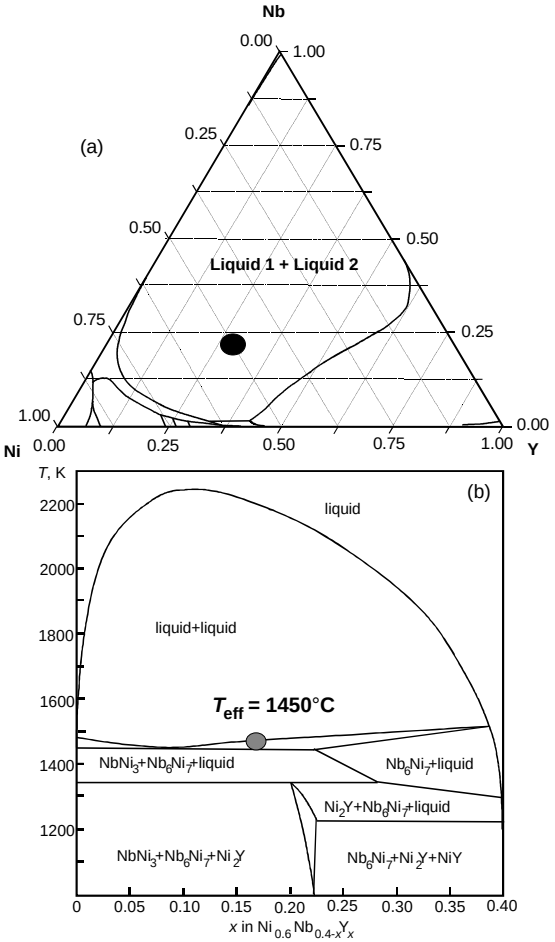

Fig. 10 (a) Liquidus projection obtained by the CALPHAD method of the Y–Ni–Nb ternary phase diagram at [95]. The composition of the triple $Ni_{50}Nb_{20}Y_{30}$ alloy used for HPT investigations is marked by the large black circle. (b). Calculated pseudo-binary section of the ternary phase diagram $Ni_{60}Y_{40}$–$Ni_{60}Nb_{40}$ [96]. Large grey circle shows the composition of phases in ultra-fine-grained alloy after HPT (two amorphous phases and two crystalline ones). The value of T_{eff} = 400°C is also given

Especially valuable data on the effective temperature at SPD can be extracted from the results on HPT treatment of Ti–48.5 at.% Ni, Ti–50.0 at.% Ni and Ti–50.7 at.% Ni alloys [97]. The HPT of equiatomic Ti–50.0 at.% Ni alloy at room temperature (point *e*, **Fig. 9**) resulted in the fully amorphous state (point 5, **Fig. 9**, T_{eff} = 1350°C, respectively). The HPT of the non-equiatomic Ti–48.5 at.% Ni alloy at 270°C (point *h*) produced the mixture of amorphous and nanocrystalline phases (point 7, T_{eff} = 1050°C). When the HPT temperature of the Ti–48.5 at.% Ni alloy increased up to 350°C (point *h*), only the mixture of nanocrystaline phases formed, without amorphous phase. It means that the corresponding point moved from the position 7 in the δ+L region into position 8 in the two-phase δ+γ region and the effective temperature decreased to T_{eff} = 950°C.

DOI 10.12776/ams.v25i4.1368 p-ISSN 1335-1532
e-ISSN 1338-1156

The HPT of another non-equiatomic Ti–50.7 at.% Ni alloy at 200°C (point *j*) produced the mixture of amorphous and nanocrystalline phases (point 9, T_{eff} = 1250°C). When the HPT temperature of the Ti–50.7 at.% Ni alloy increased up to 250°C (point *k*), only the mixture of nanocrystaline phases formed, without amorphous phase. It means that the corresponding point moved from the position 9 in the δ+L region into position 10 in the two-phase δ+β region and the effective temperature decreased to T_{eff} = 1100°C. Therefore, it can be clearly seen from the data obtained by Prokoshkin et al. [97] that the increase of the HPT treatment temperature leads to the decrease of T_{eff}. It is in full accordance with the equation (1) because the increase of T leads to increase of D_b, and at the same time the amount of deformation-driven atomic movements characterized by D_{HPT} remains unchanged. Other examples of amorhization under the action of SPD can be found in Refs. [98–103]. Nanocrystallization is a process which is opposite to the amorphization. If one applies SPD to the initially amorphous sample, one can observe that the small nanocrystals start to appear [104–112]. Obviously, the nanocrystallization and amorphization are also coupled and competing processes like precipitation/dissolution (see Section 3 above).

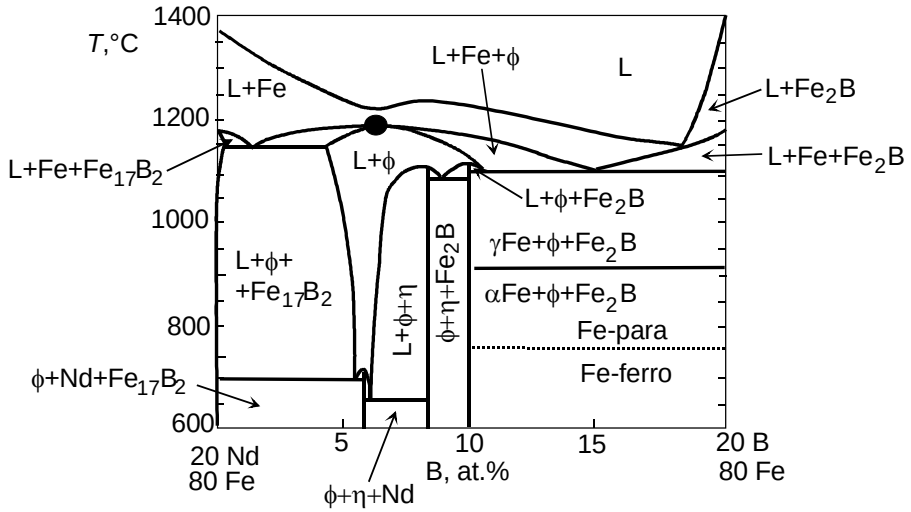

Fig. 11 The 80 at.% Fe section of the Fe–Nd–B phase diagram. Large filled circle shows the effective temperature T_{eff} = 1170±30°C [7, 8]

5 SPD-driven accelerated mass-transfer

The discussed SPD-driven phase transformations are connected with redistribution of components and, therefore, with mass transfer. This SPD-driven mass transfer is diffusion-like, in other words by the SPD-driven jump of an atom from one lattice position to another this atom has to overcome the same energetic barrier as during the conventional diffusion.

In [87, 80] we developed a mass-transfer model for the description of dynamic equilibrium in competitive precipitation and dissolution by the HPT in copper-silver system. This model assumes that HPT fixes the composition at interfaces between copper matrix and silver precipitate. It has been shown that the observed steady-state composition in the matrix and precipitate size are controlled by the HPT-enhanced diffusion-like mass-transfer. We succeeded to calculate the steady-state concentration c_{ss} using only the value of bulk diffusion coefficient *D*. Afterwards we found the T_{eff} value supposing that c_{ss} is equal to the silver solubility in copper at T_{eff}. As in the cases discussed above in Sections 3 and 4, T_{eff} in Cu–Ag alloys was higher than the HPT

DOI 10.12776/ams.v25i4.1368 p-ISSN 1335-1532
e-ISSN 1338-1156

temperature T_{HPT}. The fact that usually $T_{eff} > T_{HPT}$ means simply that the steady-state concentration of vacancies during HPT is higher than the equilibrium one at T_{HPT}. It could be close to the equilibrium vacancy concentration at T_{eff} [113, 114].

If one substitutes cobalt or silver in the copper-based solid solution, the bulk diffusion coefficient D of an impurity also changes. According to the Eq (1), the higher D would lead to the lower T_{eff} and lower D requires higher T_{eff}. **Fig. 8a** contains the plot showing nearly linear correlation between activation enthalpy of bulk diffusion H_D and T_{eff}. Physically, such correlation is easy to understand because the high H_D means also high energy barrier for the jumps of alloying atoms between lattice positions in copper. Increased energy barrier for atomic jumps decreases the diffusivity and relaxation rate in the dynamic equilibrium between precipitation and dissolution during HPT. In turn, slow relaxation, increases the steady-state concentration of non-equilibrium lattice defects (vacancies). As a result, T_{eff} would increase as well.

The SPD-driven mass transfer proceeds extremely quickly and in ambient conditions without substantial increase of sample temperature [115]. Usually, the time for establishment of steady-state by HPT is about 2-5 minutes. It varies by change of pressure, strain rate and HPT temperature, but not more than one order of magnitude. One can estimate the observed SPD-driven mass-transfer using the effective diffusion coefficient and compare it with "conventional" diffusion coefficients at temperature of HPT-treatment and at T_{eff}.

The SPD-driven phase transformations can also be analyzed when assuming [1] that the *steady-state* concentration of lattice defects during SPD is higher than that in the equilibrium at the temperature of SPD-treatment, T_{SPD}, and pressure of the SPD-treatment, P_{SPD}. It has been indeed observed in the direct measurements of vacancy concentration during HPT [115, 117]. This concentration would be equal to the *equilibrium* concentration of lattice defects at a certain effective temperature T_{eff} [1]. In case of Cu–Co system T_{eff} amounts to T_{eff} = 900°C (Fig. 7). Fig. 7 shows the composition of Cu-rich matrix in both alloys before and after HPT in the Cu–Co phase diagram. The Cu-rich solid solution in both alloys after HPT contains as much Co $c_{eq} \approx 2.5$ wt. % Co, as if they would be annealed at T_{eff} = 900°C.

The extrapolation of bulk diffusion coefficients to T_{eff} gives $D = 5x10^{-14}$ m^2/s for diffusion of Co in Cu [118] and $D = 10^{-13}$ m^2/s for self-diffusion in Cu [119]. Indeed, the deformation driven mechanisms can ensure the mass-transfer rate which is comparable to the bulk diffusion fluxes at T_{eff} = 900°C. The bulk diffusion fluxes at 900°C could ensure the decomposition/precipitation rates even if the effect of pressure is taken into account [120, 121].

6 Allotropic and martensitic transformations

Many elements exist in different allotropic modifications at different temperature and pressure. The most prominent examples are iron, cobalt, titanium. For example, the Co–Cu alloys before HPT contain the (metastable at room temperature) fcc α-Co phase, but after HPT the ε-Co phase appears in the samples [1, 59, 60, 122]. Even more interesting is the situation in Ti, Zr and Hf where the high-pressure ω-phase exists [123]. The Ti, Zr and Hf possess also two different allotropic modifications at ambient pressure, namely the low-temperature hcp α-phase and high-temperature β-phase. HPT leads to the transitions of α- and β-phases to the ω-phase which remain in the samples after pressure release [123–126]. The alloying of titanium with β-stabilizers (like Fe, Co or Nb) strongly modifies the α-β-ω-transformations [126–130]. For example, the β-to-ω-transformation in Ti-alloys is martensitic [126–128]. There are special orientation relationships between β and ω lattices which ensure the diffusionless martensitic transformations where long-

DOI 10.12776/ams.v25i4.1368 p-ISSN 1335-1532
e-ISSN 1338-1156

range mass transfer is not needed and the atoms conserve more or less their neighbors before and after transition [131]. It has been observed, for example, that iron addition changes the lattice parameters in β and ω phases in such a way that in the Ti – 4 wt. % Fe alloy the orientation relationship fulfils optimally. At this concentration the amount of ω phases transformed from the β one reaches almost 100% and decreases by lower and higher Fe concentration [126, 127]. The metastable ω-phase disappears by heating around 150°C in pure titanium. However, the alloying can stabilize it up to 500°C [131, 132].

HPT of silicon and germanium also leads to the formation of metastable high pressure phases [133, 134]. In [135] the single crystalline Si(100) was subjected to HPT at 24 GPa at room temperature. The HPT-processed samples contained lattice defects such as dislocations and nanotwins in diamond-cubic Si-I, and metastable phases such as body-centered-cubic Si-III and hexagonal-diamond Si-IV. In [134] crystalline Ge disks were subjected to HPT under the nominal pressure of 24 GPa. The samples processed at room temperature consisted of diamond-cubic Ge-I and simple tetragonal Ge-III nanograins in addition to amorphous regions. The samples processed at 77K consisted of Ge-I as well as residual Ge-III nanograins and some amorphous phase. No other metastable phases such as body-centered-cubic Ge-IV or hexagonal-diamond Ge-V were observed in the cryogenic HPT-processed sample.

Similar to the semiconductors Si and Ge, plastic deformation of oxides is generally very difficult due to their hard and brittle nature resulting from their covalent or ionic bonding. However, the HPT technique allows one to keep the silicon, germanium or oxide samples in the confined space, the samples cannot break or "escape" from the volume between the HPT anvils. This unique feature allows one to reach the high strains in the oxides. Moreover, one can start from powder samples. HPT first compact the powder and then ensures the deformation. Thus, the opportunity to strain oxides and/or metal/oxide composites is very general [136]. However, here we discuss only the cases where oxides possess different crystal lattices and respective phase transitions can take place.

Crystalline VO_2 transformed from the coarse-grained monoclinic phase to a nanograined triclinic phase with insulating electrical properties by plastic strain effect [137]. The anatase-to-rutile phase transformation in TiO_2 usually occurrs at 1173 K. During HPT of titania ceramic nanopowder the anatase-to-rutile transformation took place at 473–573 K [138]. The formation of rutile phase was accompanied with dynamic recrystallization and an unusual grain growth. A high-pressure TiO_2-II phase (columbite) with the orthorhombic structure was formed by HPT under pressures of 1 and 6 GPa. Fraction of TiO_2-II increased with increasing the plastic strain and remained stable at ambient pressure. TiO_2-II was stabilized in grains with sizes less than ~15 nm because of high energy barrier for reverse phase transformation, while larger grains had the anatase structure [139].

Barium titanate, $BaTiO_3$ belongs to the group of perovskite oxides with the general ABO_3 formula. $BaTiO_3$ transforms under ambient pressure from a rhombohedral structure to an orthorhombic phase at −90°C, to a ferroelectric tetragonal phase at 5°C, and to a paraelectric cubic phase at 120°C [140–143]. At ambient temperature, it exhibits a tetragonal-to-cubic phase transformation at 2 GPa [140–143] and it disorders at 5 GPa [144]. HPT of tetragonal $BaTiO_3$ powders leads to the formation of cubic phase and to strong grain refinement [145].

ZrO_2 has a monoclinic phase at room temperature under ambient pressure, and transforms to a tetragonal phase at 1373 K, a cubic phase at 2673 K, a liquid phase at 2963 K and an orthorhombic phase under pressures above 10 GPa [146]. However, addition of specific elements such as Y to ZrO_2 stabilizes the tetragonal phase at room temperature [147]. This partially stabilized ZrO_2

DOI 10.12776/ams.v25i4.1368 p-ISSN 1335-1532
e-ISSN 1338-1156

exhibits a phase transformation from tetragonal to monoclinic [148]. During HPT the transformation with a coherent interface occurs from the metastable tetragonal phase to the monoclinic phase [149].

7 Grain boundary phase transitions

Severe plastic deformation drives not only phase transformations between 3-dimensional or bulk phases discussed above. SPD can also lead to the various grain boundary (GB) phase transitions. The most prominent GB phase transformations like wetting-dewetting ones take place in the two-phase (or multiphase) regions of the bulk phase diagrams [150]. In case of complete wetting, the second phase (liquid or even solid one) forms the continous layer between two grains in the matrix [13, 24, 151]. In this case the contact angle between GB and second phase is zero [152]. In case of incomplete (or partial) wetting, the second phase (liquid or solid) forms the chain of individual particles along GB with a certain non-zero contact angle [153, 154]. If the amount of wetting phase is small, the continous layer between two grains can become very thin, it contains few monolayers of a second component and is just a couple of nanometers thick [155–157]. If the amount of a second component in GB is below one monolayer, one speaks about conventional GB adsorption [157, 158]. If the GB contact angle is high, but the GB between individual particles of a second phase contains few monolayers of a second component, one speaks about pseudopartial (or psedoincomplete, or constrained complete) GB wetting [159–161]. The transitions between these different GB states (phases) are called GB transitions, and they also can be driven by SPD, similar to the bulk (or volume) ones.

The grain size after SPD is very small. In other words, the specific area of grain boundaries in a volume unit increases. Therefore, the "conventional" grain boundary phase transitions become more pronounced then in the coarse-grained materials. For example, the usage of the ultrafine-grained polycrystals made it possible to observe and measure the thermal effect of the GB premelting phase transformations [162–165]. In other words, the liquid-like GB layers form well below the bulk solidus line. As a result, the melting in GBs begins during heating 10-15 °C earlier than in the bulk [162–165]. Between bulk and GB solidus the (generally solid) polycrystal contains thin liquid GBs. Such a materials possesses extremely high plasticity [166–170]. The high specific density of GBs in the SPD-treated alloys allowed one also to observe the thermal effect of phase transition from incomplete to complete GB wetting [163–165]. It takes place between bull solidus and liquidus lines.

Even in case of one-layer GB adsorption (i.e. when the concentration of a second component per GB unit area is below one monolayer), the specific area of GBs in SPD-treated polycrystals is so high that a big amount of a second component is needed to fill all GB adsorption layers. These adsorbed GB atoms are taken away from the bulk second phase. As a result, the amount of bulk second phase decreases, it can disappear completely (like, for example, disappears cementite in steels). In such a way, the GB adsorption can apparently shift the lines in the bulk phase diagrams for the ultra-fine grained materials in comparison with their coarse-grained counterparts [170–173].

The HPT of the Al–Zn, Al–Mg and Al–Zn–Mg alloys leads to the formation of 2-5 nm thin GB layers of Zn-rich phase [75, 174–182]. The contact angle between Zn particles and GB is high, the GB between individual particles of a second phase contains few monolayers of a second component. In other words, here one can speaks about pseudopartial GB wetting [159–161]. The presence of "soft" Zn-rich GB layers between grains of "hard" phase leads to a kind of lubricating

DOI 10.12776/ams.v25i4.1368 p-ISSN 1335-1532
e-ISSN 1338-1156

during GB sliding. As a result, the ultrafine-grained Al-based alloys become superductile [175–177, 179–182]. The opposite effect can also take place. Thus, the second solid phase can form before HPT the continous layers in GBs of a matrix (so-called complete GB wetting). If this phase is hard (like for example in case of Cu–Sn or Mg-based alloys), the soft matrix deform during HPT and its grains are refined, but the hard skeleton of intermetallics in the initial GBs remain more or less intact and ensure the high hardness of an alloy [13, 24, 76, 79]. All these SPD-driven GB phenomena are now under intensive investigations.

8 Conclusions

It is frequently observed that the phases in the materials after severe plastic deformation differ from those in the initial state. During SPD established a steady-state, and structure and properties of a material in this steady state do not depend on the initial state and are, therefore, equifinal. The SPD-induced phase transformations proceed very quickly, they include precipitation and dissolution of precipitates, amorphization and (nano) crystallization, allotropic and martensitic transitions and formation of grain boundary phases.

References

[1] B. B. Straumal, A.A. Mazilkin, B. Baretzky, E. Rabkin, R.Z. Valiev: Materials Transactions, Vol. 53, 2012, p. 63–71, https://doi.org/10.2320/matertrans.MD201111
[2] X. Sauvage, A. Chbihi, X. Quelennec: Journal of Physics, Vol. 240, 2010, p. 012003, https://doi.org/10.1088/1742-6596/240/1/012003
[3] B. Straumal, A. Korneva, P. Zięba: Archives of Civil and Mechanical Engineering, Vol. 14, 2014, p. 242–249, https://doi.org/10.1016/j.acme.2013.07.002
[4] E. I. Teitel', L. S. Metlov, D. V. Gunderov, A. V. Korznikov: Physics of Metals and Metallography 113, 2012, p. 1162–1168, https://doi.org/10.1134/S0031918X12120095
[5] B. B. Straumal et al.: International Journal of Materials Research, Vol. 106, 2015, p. 657–664, https://doi.org/10.3139/146.111215
[6] B. B. Straumal, A. R. Kilmametov, A. Korneva, A. A. Mazilkin, P. B. Straumal, P. Zięba, B. Baretzky: Journal of Alloys and Compounds, Vol. 707, 2017, p. 20–26, https://doi.org/10.1016/j.jallcom.2016.12.057
[7] B. B. Straumal et al.: Materials Letters, Vol. 145, 2015, p. 63–66, https://doi.org/10.1016/j.matlet.2015.01.041
[8] B. B. Straumal, A. A. Mazilkin, S. G. Protasova, D. V. Gunderov, G. A. López, B. Baretzky: Materials Letters, Vol. 161, 2015, p. 735–739, https://doi.org/10.1016/j.matlet.2015.09.076
[9] C. Borchers et al.: Acta Materialia, Vol. 97, 2015, p. 207–215, https://doi.org/10.1016/j.actamat.2015.06.049
[10] S. Lee, Z. Horita: Materials Transactions , Vol. 53, 2012, p. 38–45, https://doi.org/10.2320/matertrans.MD201109
[11] K. Edalati, S. Toh, M. Watanabe, Z. Horita: Scripta Materialia, Vol. 66, 2012, p. 386–389, https://doi.org/10.1016/j.scriptamat.2011.11.039
[12] J. M. Cubero-Sesin, Z. Horita: Materials Transactions, Vol. 53, 2012, p. 46–55, https://doi.org/10.2320/matertrans.MD201110
[13] K. Bryła, J. Morgiel, M. Faryna, K. Edalati, Z. Horita: Materials Letters, Vol. 212, 2018, p. 323–326, https://doi.org/10.1016/j.matlet.2017.10.113
[14] A. A. Mazilkin, B. B. Straumal, S. G. Protasova, O. A. Kogtenkova, R. Z. Valiev: Physics of Solid State, Vol. 49, 2007, p. 868–873, https://doi.org/10.1134/S1063783407050113

[15] B. B. Straumal et al.: Journal of Materials Sciencs, Vol. 46, 2011, p. 4243–4247, https://doi.org/10.1007/s10853-011-5257-6
[16] K. Edalati et al.: Materials Transactions, Vol. 57, 2016, p. 533–538, https://doi.org/10.2320/matertrans.M2015374
[17] K. Edalati, Y. Hashiguchi, P.H.R. Pereira, Z. Horita, T. G. Langdon: Materials Science and Engineering A, Vol. 714, 2018, p. 167–171, https://doi.org/10.1016/j.msea.2017.12.095
[18] K. Edalati, Z. Horita: Acta Materialia, Vol. 59, 2011, p. 6831–6836, https://doi.org/10.1016/j.actamat.2011.07.046
[19] K. Edalati, Z. Horita, T. Furuta, S. Kuramoto: Materials Science and Engineering A, Vol. 559, 2013, p. 506–509, https://doi.org/10.1016/j.msea.2012.08.132
[20] A.A. Mazilkin, O.A. Kogtenkova, B.B. Straumal, R.Z. Valiev, B. Baretzky: Defect and Diffusion Forum, Vol. 237–240, 2005, p. 739–744, https://doi.org/10.4028/www.scientific.net/DDF.237.739
[21] A. A. Mazilkin et al.: Defect and Diffusion Forum, Vol. 249, 2006, p. 155–160, https://doi.org/10.4028/www.scientific.net/DDF.249.155
[22] R. Kulagin, Y. Beygelzimer, Yu. Ivanisenko, A. Mazilkin, B. Straumal, H. Hahn: Materials Letters, Vol. 222, 2018, p. 172–175, https://doi.org/10.1016/j.matlet.2018.03.200
[23] R. Z. Valiev, R. K. Islamgaliev, I. V. Alexandrov: Progress in Materials Science, Vol. 45, 2000, p. 103–189, https://doi.org/10.1016/S0079-6425(99)00007-9
[24] K. Bryła et al.: Materials Science and Engineering A, Vol. 737, 2018, p. 318–327, https://doi.org/10.1016/j.msea.2018.09.070
[25] E. A. Lukyanova et al.: Russian Metallurgy (Metally), Vol. 11, 2017, p. 912–921, https://doi.org/10.1134/S0036029517110088
[26] P. Kral et al.: Materials Science and Engineering A, Vol. 723, 2018, p. 287–295, https://doi.org/10.1016/j.msea.2018.03.059
[27] S. Sabbaghianrad, S.A. Torbati-Sarraf, T.G. Langdon: Materials Science and Engineering A, Vol. 712, 2018, p. 373–379, https://doi.org/ 0.1016/j.msea.2017.11.090
[28] K. Tirsatine et al.: Journal of Alloys and Compounds, Vol. 753, 2018, p. 46–53, https://doi.org/10.1016/j.jallcom.2018.04.194
[29] M. Y. Alawadhi, S. Sabbaghianrad, Y. Huanga, T.G. Langdon: Journal of Materials Research and Technology, Vol. 6, 2017, p. 369–377, https://doi.org/10.1016/j.jmrt.2017.05.005
[30] M. Azabou et al.: The International Journal of Advanced Manufacturing Technology, Vol. 87, 2016, p. 981–987, https://doi.org/10.1007/s00170-016-8551-2
[31] A. A. Mazilkin et al.: Acta Materialia, Vol. 54, 2006, p. 3933–3939, https://doi.org/10.1016/j.actamat.2006.04.025
[32] B. Straumal et al.: Materials Letters, Vol. 118, 2014, p. 111–114, https://doi.org/10.1016/j.matlet.2013.12.042
[33] Y. Huang, S. Sabbaghianrad, A.I. Almazrouee, K.J. Al-Fadhalah, S.N. Alhajeri, T.G. Langdon: Materials Science and Engineering A, Vol. 656, 2016, p. 55–66, https://doi.org/10.1016/j.msea.2016.01.027
[34] N. Lugo, N. Llorca, J.M. Cabrera, Z. Horita: Materials Science and Engineering A, Vol. 477, 2008, p. 366–371, https://doi.org/10.1016/j.msea.2016.01.027
[35] J. Čížek et al.: Acta Materialia, Vol. 59, 2011, p. 2322–2329, https://doi.org/10.1016/j.actamat.2010.12.028
[36] X. Z. Liao, Y. H. Zhao, Y. T. Zhu, R. Z. Valiev, D. V. Gunderov: Journal of Applied Physics, Vol. 96, 2004, p. 636–640, https://doi.org/10.1063/1.1757035

[37] M. Shamsborhan, M. Ebrahimi: Journal of Alloys and Compounds, Vol. 682, 2016, p. 552–556, https://doi.org/ 10.1016/j.jallcom.2016.05.012
[38] C. L. Tang, H. Li, S. Y. Li: The Transactions of Nonferrous Metals Society of China, Vol. 26, 2016, p. 1736−1744, https://doi.org/10.1016/S1003-6326(16)64286-3
[39] Z. N. Mao et al.: Materials Science and Engineering A, Vol. 674, 2016, p. 186–192, https://doi.org/10.1016/j.msea.2016.07.050
[40] E. Bagherpour, F. Qods, R. Ebrahimi, H. Miyamoto: Materials Science and Engineering A, Vol. 674, 2016, p. 221–231, https://doi.org/10.1016/j.msea.2016.08.001
[41] E. Bagherpour, F. Qods, R. Ebrahimi, H. Miyamoto: Materials Science and Engineering A, Vol. 666, 2016, p. 324–338, https://doi.org/10.1016/j.msea.2016.04.080
[42] P.C. Yadav, A. Sinhal, S. Sahu, A. Roy, S. Shekhar: Journal of Materials Engineering and Performance, Vol. 25, 2016, p. 2604–2614, https://doi.org/10.1007/s11665-016-2142-0
[43] C. Xu, Z. Horita, T.G. Langdon: Materials Science and Engineering A, Vol. 528, 2011, p. 6059–6065, https://doi.org/10.1016/j.msea.2011.04.017
[44] K. Edalati, Z. Horita: Materials Science and Engineering A, Vol. 528, 2011, p. 7514– 7523, https://doi.org/10.1016/j.msea.2011.06.080
[45] A. V. Korznikov, Y. V. Ivanisenko, D. V. Laptionok, I. M. Safarov, V. P. Pilyugin, R. Z. Valiev: Nanostructured Materials, Vol. 4, 1994, p. 159–167, https://doi.org/10.1007/s11665-016-2142-0
[46] Y. Ivanisenko, W. Lojkowski, R. Z. Valiev, H.-J. Fecht: Acta Materialia, Vol. 51, 2003, p. 5555–5570, https://doi.org/ 10.1016/S1359-6454(03)00419-1
[47] Y. Ivanisenko, R.K. Wunderlich, R.Z. Valiev, H.-J. Fecht: Scripta Materialia, Vol. 49, 2003, p. 947–952, https://doi.org/10.1016/S1359-6462(03)00478-0
[48] J. Zrnik, R. Pippan, S. Scheriau, L. Kraus, M. Fujda: Journal of Materials Science 45, 2010, p. 4822–4826, https://doi.org/10.1007/s10853-010-4482-8
[49] S. Bayramoglu, C. H. Gür, I. V. Alexandrov, M. M. Abramova: Materials Science and Engineering A, Vol. 527, 2010, p. 927–933, https://doi.org/10.1016/j.msea.2009.09.006
[50] J. Ningn et al.: Materials Science and Engineering A, Vol. 581, 2013, p. 8–15, https://doi.org/10.1016/j.msea.2013.05.008
[51] Y. Todaka, Y. Miki, M. Umemoto, C. Wang, K. Tsuchiya: Materials Science Forum, Vol. 584–586, 2008, p. 597–604, https://doi.org/10.4028/www.scientific.net/DSF.584.597
[52] X. Z. Liao et al.: Applied Physics Letters, Vol. 88, 2006, p. 021909, https://doi.org/10.1063/1.2159088
[53] R. Pippan, S. Scheriau, A. Taylor, M. Hafok, A. Hohenwarter, A. Bachmaier: Annual Review of Materials Research, Vol. 40, 2010, p. 319–343, https://doi.org/ 10.1146/annurev-matsci-070909-104445
[54] H. Wen, R.K. Islamgaliev, K.M. Nesterov, R.Z. Valiev, E.J. Lavernia: Philosophical Magazine Letters, Vol. 93, 2013, p. 481–489, https://doi.org/10.1080/09500839.2013.805268
[55] K. Edalati et al.: Acta Materialia, Vol. 69, 2014, p. 68–77, https://doi.org/10.1016/j.actamat.2014.01.036
[56] R. Tejedora, K. Edalati, J.A. Benito, Z. Horita, J. M. Cabrera: Materials Science and EngineeringA , Vol. 743, 2019, p. 597–605, https://doi.org/10.1016/j.msea.2018.11.127
[57] I. F. Mohamed et al.: Materials Science and Engineering A, Vol. 704, 2017, p. 112–118, https://doi.org/10.1016/j.msea.2017.07.083

[58] K. Edalati, H. Shao, H. Emami, H. Iwaoka, E. Akiba, Z. Horita: International Journal of Hydrogen Energy, Vol. 41, 2016, p. 8917–8924, https://doi.org/10.1016/j.ijhydene.2016.03.146
[59] M. Isika et al.: Journal of the Mechanical Behavior of Biomedical Materials, Vol. 59, 2016, p. 226–235, https://doi.org/10.1016/j.jmbbm.2015.11.015
[60] M. Isik et al.: Materials Transactions, Vol. 57, 2016, p. 1109–1118, https://doi.org/10.2320/matertrans.M2016052
[61] T. Hongo et al.: Materials Science and Engineering A, Vol. 618, 2014, p. 1–8, https://doi.org/10.1016/j.msea.2014.08.074
[62] K. Edalati, K. Imamura, T. Kiss, Z. Horita: Materials Transactions, Vol. 53, 2012, p. 123–127, https://doi.org/10.2320/matertrans.MD201109
[63] A. Hanna et al.: Journal of Alloys and Compounds, Vol. 778, 2019, p. 61–71, https://doi.org/10.1016/j.jallcom.2018.11.109
[64] Y. I. Bourezg et al.: Materials Science and Engineering A, Vol. 724, 2018, p. 477–485, https://doi.org/10.1016/j.msea.2018.03.114
[65] P. Bazarnik, Y. Huang, M. Lewandowska, T. G. Langdon: Materials Science and Engineering A, Vol. 712, 2018, p. 513–520, https://doi.org/10.1016/j.msea.2017.12.007
[66] D. M. M. Cardona, J. Wongsa-Ngam, H. Jimenez, T. G. Langdon: Journal of Materials Research and Technology, Vol. 6, 2017, p. 355–360, https://doi.org/10.1016/j.jmrt.2017.05.002
[67] S. A. Torbati-Sarraf, S. Sabbaghianrad, R. B. Figueiredo, T. G. Langdon: Journal of Alloys and Compounds, Vol. 712, 2017, p. 185–193, https://doi.org/10.1016/j.jallcom.2017.04.054
[68] M. Diez, H.-E. Kim, V. Serebryany, S. Dobatkin, Y. Estrin: Materials Science and Engineering A, Vol. 612, 2014, p. 287–292, https://doi.org/10.1016/j.msea.2014.06.061
[69] E. A. Lukyanova, N. S. Martynenko, I. Shakhova, A. N. Belyakov, L. L. Rokhlin, S. V. Dobatkin, Y. Z. Estrin: Materials Letters, Vol. 170, 2016, p. 5–9, https://doi.org/10.1016/j.matlet.2016.01.106
[70] N. S. Martynenko, E. A. Luk'yanova, M. M. Morozov, V. S. Yusupov, S. V. Dobatkin, Y. Z. Estrin: Metal Science and Heat Treatment, Vol. 60, 2018, p. 253–258, https://doi.org/10.1007/s11041-018-0269-3
[71] C. C. Koch, T. G. Langdon, E. J. Lavernia: Metallurgical and Materials Transactions A, Vol. 48, 2017, p. 5181–5199, https://doi.org/s11661-017-4298-0
[72] A. A. Mazilkin, B. B. Straumal, M. V. Borodachenkova, R. Z. Valiev, O. A. Kogtenkova, B. Baretzky: Materials Letters, Vol. 84, 2012, p. 63–65, https://doi.org/10.1016/j.matlet.2012.06.026
[73] B. B. Straumal et al.: Acta Materialia, Vol. 52, 2004, p. 4469–4478, https://doi.org/10.1016/j.actamat.2004.06.006
[74] Y. Ito, K. Edalati, Z. Horita: Materials Science and Engineering A, Vol. 679, 2017, p. 428–434, https://doi.org/ 0.1016/j.msea.2016.10.066
[75] X. Sauvage, M. Yu. Murashkin, B. B. Straumal, E. Bobruk, R. Z. Valiev: Advanced Engineering Materials , Vol. 17, 2015, p. 1821–1827, https://doi.org/10.1002/adem.201500151
[76] V. D. Sitdikov, P. S. Chizhov, M. Yu. Murashkin, R. Z. Valiev: Reviews on Advanced Materials Science, Vol. 47, 2016, p. 59–65
[77] A. Korneva et al.: Inżynieria Materiałowa, Vol. 34, 2013, p. 306–309, https://doi.org/10.15199/34.2013.4.6

[78] B. B. Straumal et al.: Materials Letters, Vol. 98, 2013, p. 217–221, https://doi.org/10.1016/j.matlet.2013.02.058
[79] L. von Bertalanffy, Science, Vol. 111, 1950, p. 23–29, https://doi.org/10.1126/science.111.2872.23
[80] B. B. Straumal et al.: Journal of Materials Science, Vol. 47, 2012, p. 360–367, https://doi.org/10.1007/s10853-011-5805-0
[81] B. B. Straumal et al.: JETP Letters, Vol. 100, 2014, p. 376–379, https://doi.org/10.1134/S0021364014180106
[82] A. Korneva et al.: Materials Letters, Vol. 179, 2016, p. 12–15, https://doi.org/10.1016/j.matlet.2016.05.059
[83] A. Korneva, B. Straumal, A. Kilmametov, G. Cios, P. Bała, P. Zięba: Materials Characterisation, Vol. 118, 2016, p. 411–416, https://doi.org/10.1016/j.matchar.2016.06.019
[84] A. Korneva et al.: IOP Conference Series: Materials Science and Engineering, Vol. 63, 2014, p. 012093, https://doi.org/10.1088/1757-899X/63/1/012093
[85] B.B. Straumal et al.: Materials Letters, Vol. 138, 2015, p. 255–258, https://doi.org/10.1016/j.matlet.2014.10.009
[86] A. Korneva, B. Straumal, A. Kilmametov, R. Chulist, P. Straumal, P. Zięba: Materials Characterisation, Vol. 114, 2016, p. 151–156, https://doi.org/10.1016/j.matchar.2016.02.017
[87] B. B. Straumal, V. Pontikis, A. R. Kilmametov, A. A. Mazilkin, S. V. Dobatkin, B. Baretzky: Acta Materialia, Vol. 122, 2017, p. 60–71, https://doi.org/10.1016/j.actamat.2016.09.024
[88] A. Korneva et al.: Materials , Vol. 12, 2019, p. 447, https://doi.org/10.3390/ma12030447
[89] B. B. Straumal et al.: International Journal of Materials Research , Vol. 110, 2019, p. 608–613, https://doi.org/10.3139/146.111784
[90] G. A. López et al.: Materials Today: Proceedings, Vol. 2S, 2015, p. S747–S750, https://doi.org/10.1016/j.matpr.2015.07.390
[91] B. B. Straumal et al.: Acta Materialia, Vol. 125, 2017, p. 274–285, https://doi.org/10.1016/j.actamat.2016.12.003
[92] G. Martin: Physical Review B, Vol. 30, 1984, p. 1424–1436, https://doi.org/10.1103/PhysRevB.30.1424
[93] B. B. Straumal et al.: Kovove Materialy-Metallic Materials, Vol. 49, 2011, p. 17–22, https://doi.org/10.4149/km-2011-1-17
[94] A. A. Mazilkin et al.: Journal of Materials Science, Vol. 46, 2011, p. 4336–4342, https://doi.org/10.1007/s10853-011-5304-3
[95] U. R. Kattner: Journal of Materials (JOM), Vol. 49, 1997, p. 14–19, https://doi.org/10.1007/s11837-997-0024-5
[96] N. Mattern, U. Kühn, A. Gebert, A. Schoeps, T. Gemminga, L. Schultz: Materials Science and Engineering A, Vol. 449/451, 2007, p. 207–210, https://doi.org/ 0.1016/j.msea.2006.02.269
[97] S. D. Prokoshkin et al.: Acta Materialia, Vol. 53, 2005, p. 2703–2714, https://doi.org/ 0.1016/j.actamat.2005.02.032
[98] A. V. Sergueeva, C. Song, R. Z. Valiev, A. K. Mukherjee: Materials Science and Engineering A, Vol. 339, 2003, p. 159–165, https://doi.org/10.1016/S0921-5093(02)00122-3
[99] X. Sauvage, L. Renaud, B. Deconihout, D. Blavette, D. H. Ping, K. Hono: Acta Materalia, Vol. 49, 2001, p. 389–394, https://doi.org/10.1016/S1359-6454(00)00338-4
[100] T. Miyazaki et al.: Journal of Materials Science, Vol. 46, 2011, p. 4296–4301, https://doi.org/10.1007/s10853-010-5240-7

[101] V.V. Stolyarov, D.V. Gunderov, A.G. Popov, V.S. Gaviko, A. S. Ermolenko: Journal of Alloys and Compounds, Vol. 281, 1998, p. 69–71, https://doi.org/10.1016/S0925-8388(98)00774-9
[102] Y. Matsuura, S. Hirosawa, H. Yamamoto, S. Fujimira, M. Sagawa, K. Osamura: Japanese Journal of Applied Physics Part 2 – Letters, Vol. 24, 1985, p. L635– L637, https://doi.org/10.1143/JJAP.24.L635
[103] Á. Révész, S. Hóbor, J. L. Lábár, A. P. Zhilyaev, Zs. Kovácz: Journal of Applied Physics, Vol. 100, 2006, p. 103522, https://doi.org/10.1063/1.2388868
[104] A. M. Glezer, M. R. Plotnikova, A. V. Shalimova, S. V. Dobatkin: Bulletin of the Russian Academy of Sciences. Physics, Vol. 73, 2009, p. 1233–1236, https://doi.org/10.3103/S1062873809090123
[105] S. Hóbor, Á. Révész, A. P. Zhilyaev, Zs. Kovácz: Reviews of Advanced Materials Science, Vol. 18, 2008, p. 590–592
[106] Zs. Kovács, P. Henits, A. P. Zhilyaev, Á. Révész: Scripta Materialia, Vol. 54, 2006, p. 1733–1737, https://doi.org/10.1016/j.scriptamat.2006.02.004
[107] G. E. Abrosimova et al.: Journal of Metastable and Nanocrystalline Materials, Vol. 24, 2005, p. 69–72, https://doi.org/10.4028/www.scientific.net/JMNM.24-25.69
[108] Á. Révész, E. Schafler, Zs. Kovács: Applied Physics Letters, Vol. 92, 2008, p. 011910, https://doi.org/10.1063/1.3064125
[109] S. Hóbor, Zs. Kovács, A. P. Zhilyaev, L. K. Varga, P. J. Szabó, Á. Révész: Journal of Physics, Vol. 240, 2010, p. 012153, https://doi.org/10.1088/1742-6596/240/1/012153
[110] S. Hóbor et al.: Journal of Applied Physics, Vol. 104, 2008, p. 033525, https://doi.org/10.1063/1.2964115
[111] P. Henits, Á. Révész, A. P. Zhilyaev, Zs. Kovács: Journal of Alloys and Compounds, Vol. 461, 2008, p. 195–199, https://doi.org/10.1016/j.jallcom.2007.07.049
[112] Zs. Kovács, P. Henits, A.P. Zhilyaev, N.Q. Chinh, Á. Révész: Materials Science Forum, Vol. 519-521, 2006, p. 1329–1334, https://doi.org/10.4028/www.scientific.net/DDF.519.1329
[113] B. Oberdorfer et al.: Physical Review Letters, Vol. 105, 2010, p. 146101, https://doi.org/10.1103/PhysRevLett.105.146101
[114] J. Čížek, O. Melikhova, Z. Barnovská, I. Procházka, R. K. Islamgaliev: Journal of Physics: Conference Series, Vol. 443, 2013, p. 012008, https://doi.org/10.1088/1742-6596/443/1/012008
[115] B. B. Straumal, O. A. Kogtenkova, R. Z. Valiev, P. Zięba, B. Baretzky: Diffusion Fundamentals, Vol. 5, 2015, p. 95–108, https://doi.org/10.4028/www.scientific.net/DF.5.95
[116] T. Ungar, E. Schafler, P. Hanak, S. Bernstorff, M. Zehetbauer: Materials Science and Engineering A, Vol. 462, 2007, p. 398–401, https://doi.org/10.1016/j.msea.2006.03.156
[117] T. Ungár, E. Schafler, P. Hanák, S. Bernstorff, M. Zehetbauer: Zeitschrift für Metallkunde, Vol. 96, 2005, p. 578–583, https://doi.org/10.3139/146.101073
[118] C. A. Mackliet: Physical Review, Vol. 109, 1958, p. 1964–1970, https://doi.org/10.1103/PhysRev.109.1964
[119] S. Fujikawa, K.I. Hirano, in: Proc. of Yamada Vth Conf. on Point Defects, Defect Interactions in Metals, J.I. Takamura, M. Doyama, M. Kiritani (Eds.) University of Tokyo Press, 1982, p. 554–558.

[120] D. A. Molodov, B. B. Straumal, L. S. Shvindlerman: Scripta Metallurgica, Vol. 18, 1984, p. 207–211, https://doi.org/10.1016/0036-9748(84)90509-X
[121] B. B. Straumal, L. M. Klinger, L. S. Shvindlerman: Scripta Metallurgica, Vol. 17, 1983, p. 275–279, https://doi.org/10.1016/0036-9748(83)90156-4
[122] B. B. Straumal et al.: Philosophical Magazine Letters, Vol. 89, 2009, p. 649–654, https://doi.org/10.1080/09500830903246268
[123] B. B. Straumal et al.: Materials Letters, Vol. 81, 2012, p. 225–228, https://doi.org/10.1016/j/matlet.2012.04.153
[124] B. B. Straumal, A. S. Gornakova, O. B. Fabrichnaya, M. J. Kriegel, A. A. Mazilkin, B. Baretzky, A. M. Gusak, S. V. Dobatkin: High Temp. Mater. Proc. , Vol. 31, 2012, p. 339–350, https://doi.org/10.1515/htmp-2012-0057
[125] A. Kilmametov et al.: Scripta Materialia, Vol. 136, 2017, p. 46–49, https://doi.org/10.1016/j.scriptamat.2017.04.010
[126] A. Kilmametov et al.: Acta Materialia, Vol. 144, 2018, p. 337–351, https://doi.org/10.1016/j.actamat.2017.10.051
[127] B. B. Straumal et al.: Journal of Alloys and Compounds, Vol. 735, 2018, p. 2281–2286, https://doi.org/10.1016/j.jallcom.2017.11.317
[128] A. R. Kilmametov, Yu. Ivanisenko, B. B. Straumal, A. S. Gornakova, A. A. Mazilkin, H. Hahn: Metals, Vol. 8, 2018, p. 1–12, https://doi.org/10.3390/met8010001
[129] A. S. Gornakova et al.: Journal of Applied Physics, Vol. 125, 2019, p. 082522, https://doi.org/10.1063/1.5053937
[130] B. B. Straumal et al.: Materials, Vol. 12, 2019, p. 426, https://doi.org/10.3390/ma12030426
[131] B. B. Straumal et al.: Advanced Engineering Materials, Vol. 17, 2015, p. 1835–1841, https://doi.org/10.1002/adem.201500143
[132] M. J. Kriegel et al.: Advanced Engineering Materials, Vol. 20, 2018, p. 1700933, https://doi.org/10.1002/adem.201700933
[133] B. Chon et al.: Scripta Materialia, Vol. 157, 2018, p. 120–123, https://doi.org/10.1016/j.scriptamat.2018.08.011
[134] Y. Ikoma, K. Kumano, K. Edalati, M. R. McCartney, D. J. Smith, Z. Horita: Materials Characterization, Vol. 132, 2017, p. 132–138, https://doi.org/10.1016/j.matchar.2017.08.011
[135] Y. Fukushima, Y. Ikoma, K. Edalati, B. Chon, D. J. Smith, Z. Horita: Materials Characterization, Vol. 129, 2017, p. 163–168, https://doi.org/10.1016/j.matchar.2017.04.025
[136] Y. Qi, A. Kosinova, A. R. Kilmametov, B. B. Straumal, E. Rabkin: Materials Characterization, Vol. 145, 2018, p. 389–401, https://doi.org/10.1016/j.matchar.2018.09.001
[137] K. Edalati, I. Fujita, X. Sauvage, M. Arita, Z. Horita: Journal of Alloys and Compounds, Vol. 779, 2019, p. 394–398, https://doi.org/10.1016/j.jallcom.2018.11.086
[138] K. Edalati, Q. Wang, H. Razavi-Khosroshahi, H. Emami, M. Fuji, Z. Horita: Scripta Materialia, Vol. 162, 2019, p. 341–344, https://doi.org/10.1016/j.scriptamat.2018.11.044
[139] H. Razavi-Khosroshahi, K. Edalati, M. Arita, Z. Horita, M. Fuji: Scripta Materialia, Vol. 124, 2016, p. 59–62, https://doi.org/10.1016/j.scriptamat.2016.06.022
[140] W. Zhong, D. Venderbilt, K.M. Rabe: Physical Review Letters, Vol. 73, 1994, p. 1861–1864, https://doi.org/10.1103/PhysRevLett.73.1861

[141] T. Ishidate, S. Abe, H. Takahashi, N. Mori: Physical Review Letters, Vol. 78, 1997, p. 2397–2400, https://doi.org/ 10.1103/PhysRevLett.78.2397
[142] S. A. Hayward, E. K. H. Salje: Journal of Physics: Condensed Matter, Vol. 14, 2002, p. L599–L604, https://doi.org/10.1088/0953-8984/14/36/101
[143] J. J. Wang, P. P. Wu, X. Q. Ma, L. Q. Chen: Journal of Applied Physics, Vol. 108, 2010, p. 114105, https://doi.org/10.1063/1.3504194
[144] U. D. Venkateswaran, V. M. Naik, R. Naik: Physical Review B, Vol. 58, 1998, p. 14256–14260, https://doi.org/10.1103/PhysRevB.58.14256
[145] K. Edalati et al.: Materials Research Letters, Vol. 3, 2015, p. 216–221, https://doi.org/10.1080/21663831.2015.1065454
[146] R. C. Garvie, R. H. J. Hannink, R. T. Pascoe: Nature, Vol. 258, 1975, p. 703–704, https://doi.org/10.1038/258703a0
[147] R. H. J. Hannink, P. M. Kelly, B. C. Muddle: Journal of American Ceramic Society, Vol. 83, 2000, p. 461–487, https://doi.org/10.1111/j.1151-2916.2000.tb01221.x
[148] J. M. Leger, P. E. Tomaszewski, A. Atouf, A. S. Pereira: Physical Review B, Vol. 47, 1993, p. 14075–14083, https://doi.org/ 10.1103/PhysRevB.47.14075
[149] K. Edalati, S. Toh, Y. Ikoma, Z. Horita: Scripta Materialia, Vol. 65, 2011, p. 974–977, https://doi.org/10.1016/j.scriptamat.2011.08.024
[150] E. I. Rabkin, L. S. Shvindlerman, B. B. Straumal: International Journal of Modern Physics B, Vol. 5, 1991, p. 2989–3028, https://doi.org/10.1142/S0217979291001176
[151] B. B. Straumal, O. I. Noskovich, V. N. Semenov, L. S. Shvindlerman, W. Gust, B. Predel: Acta Metallurgica et Materialia, Vol. 40, 1992, p. 795–801, https://doi.org/10.1016/0956-7151(92)90021-6
[152] B. B. Straumal, W. Gust, T. Watanabe: Materials Science Forum, Vol. 294/296, 1999, p. 411–414, https://doi.org/10.4028/www.scientific.net/DDF.294.411
[153] B. B. Straumal et al.: Reviews of Advanced Materials Science, Vol. 38, 2014, p. 17–28
[154] A. B. Straumal, K. V. Tsoi, I. A. Mazilkin, A. N. Nekrasov, K. Bryła: Archives of Metallurgy and Materials, 64, 2019, p. 869–873, https://doi.org/10.24425/amm.2019.129463
[155] L.-S. Chang, B.B. Straumal, E. Rabkin, W. Gust, F. Sommer: Journal of Phase Equilibria, Vol. 18, 1997, p. 128–135, https://doi.org/10.1007/BF02665694
[156] L. S. Chang, E. Rabkin, B. Straumal, P. Lejcek, S. Hofmann, W. Gust: Scripta Materialia, Vol. 37, 1997, p. 729–735, https://doi.org/10.1016/S1359-6462(97)00171-1
[157] L. S. Chang, E. Rabkin, B. B. Straumal, S. Hoffmann, B. Baretzky, W. Gust: Defect and Diffusion Forum, Vol. 156, 1998, p. 135–146, https://doi.org/10.4028/www.scientific.net/DDF.156.135
[158] B. B. Straumal, P. Zięba, W. Gust: International Journal of Inorganic Materials, Vol. 3, 2001, p. 1113–1115, https://doi.org/10.1016/S1466-6049(01)00108-8
[159] B. B. Straumal, A. O. Rodin, A. E. Shotanov, A. B. Straumal, O. A. Kogtenkova, B. Baretzky: Defect and Diffusion Forum, Vol. 333, 2013, p. 175–192, https://doi.org/10.4028/www.scientific.net/DDF.333.175
[160] B. B. Straumal, A. A. Mazilkin, S. G. Protasova, G. Schütz, A. B. Straumal, B. Baretzky: Journal of Materials Engineering and Performance, Vol. 25, 2016, p. 3303–3309, https://doi.org/10.1007/s11665-015-1872-8
[161] B. B. Straumal, A. A. Mazilkin, B. Baretzky: Current Opinion in Solid State & Materials Science, Vol. 20, 2016, p. 247–256, https://doi.org/10.1016/j.cossms.2016.05.006

[162] B. Straumal et al.: Acta Materialia, Vol. 56, 2008, p. 6123–6131, https://doi.org/10.1016/j.actamat.2008.08.021
[163] O. A. Kogtenkova et al.: Journal of Materials Science, Vol. 47, 2012, p. 8367–8371, https://doi.org/10.1007/s10853-012-6786-3
[164] O. A. Kogtenkova, B. B. Straumal, S. G Protasova, A. S. Gornakova, P. Zięba, T. Czeppe: JETP Letters, Vol. 96, 2012, p. 380–384, https://doi.org/10.1134/S0021364012180063
[165] O. A. Kogtenkova, P. Zieba, T. Czeppe, L. Lityn'ska-Dobrzynska, B.B. Straumal, A.N. Nekrasov: Bulletin of the Russian Academy of Sciences: Physics, Vol. 77, 2013, p. 1386–1390, https://doi.org/10.3103/S1062873813110166
[166] K. Higashi, T. G. Nieh, M. Mabuchi, J. Wadsworth: Scripta Metallurgica et Materialia, Vol. 32, 1995, p. 1079–1084, https://doi.org/10.1016/0956-716X(94)00003-Z
[167] Y. Takayama, T. Tozawa, H. Kato: Acta Materialia, Vol. 47, 1999, p. 1263–1270, https://doi.org/10.1016/S1359-6454(98)00416-9
[168] H. Iwasaki, T. Mori, M. Mabuchi, K. Higashi: Acta Materialia, Vol. 46, 1998, p. 6351–6360, https://doi.org/10.1016/S1359-6454(98)00330-9
[169] B. Baudelet, M. C. Dang, F. Bordeaux: Scripta Metallurgica et Materialia, Vol. 26, 1992, p. 573–578, https://doi.org/10.1016/0956-716X(92)90286-N
[170] B. B. Straumal et al.: Materials Science and Engineering A, Vol. 503, 2009, p. 185–189, https://doi.org/10.1016/j.msea.2008.03.052
[171] B. B. Straumal et al.: Defect and Diffusion Forum, Vol. 309–310, 2011, p. 51–62, https://doi.org/10.4028/www.scientific.net/DDF.309.319
[172] B. B. Straumal et al.: Advanced Engineering Materials, Vol. 13, 2011, p. 463–469, https://doi.org/10.1002/adem. 201000312
[173] Yu. Ivanisenko, X. Sauvage, A. Mazilkin, A. Kilmametov, J.A. Beach, B.B. Straumal: Advanced Engineering Materials, Vol. 20, 2018, p. 1800443, https://doi.org/10.1002/adem.201800443
[174] B. Straumal et al.: Acta Materialia, Vol. 56, 2008, p. 6123–6131, https://doi.org/10.1016/j.actamat.2008.08.021
[175] R. Z. Valiev, M. Yu. Murashkin, B. B. Straumal: Materials Science Forum, Vol. 633-634, 2009, p. 321–332, https://doi.org/10.4028/www.scientific.net/DSF.633.321
[176] R. Z. Valiev, M. Y. Murashkin, A. Kilmametov, B. B. Straumal, N. Q. Chinh, T. G. Langdon: Journal of Materials Science, Vol. 45, 2010, p. 4718–4724, https://doi.org/10.1007/s10853-010-4588-z
[177] N. Q. Chinh, T. Csanádi, J. Gubicza, R. Z. Valiev, B. B. Straumal, T. G. Langdon: Materials Science Forum, Vol. 667-669, 2011, p. 677–682, https://doi.org/10.4028/www.scientific.net/DSF.667.677
[178] O. A. Kogtenkova et al.: Journal of Materials Science, Vol. 48, 2013, p. 4758–4765, https://doi.org/10.1007/s10853-013-7266-0
[179] B. B. Straumal, X. Sauvage, B. Baretzky, A. A. Mazilkin, R. Z. Valiev: Scripta Materialia, Vol. 70, 2014, p. 59–62, https://doi.org/10.1016/j.scriptamat.2013.09.019
[180] N. Q. Chinh et al.: Advanced Engineering Materials, Vol. 16, 2014, p. 1000–1009, https://doi.org/10.1002/adem.201300450
[181] B. B. Straumal, A. A. Mazilkin, X. Sauvage, R. Z. Valiev, A. B. Straumal, A. M. Gusak: Russian Journal of Non-Ferrous Metals, Vol. 56, 2015, p. 44–51, https://doi.org/10.3103/S1067821215010198
[182] N. Q. Chinh et al.: Materials Science and Engineering A, Vol. 543, 2012, p. 117–120, https://doi.org/10.1016/j.msea.2012.02.056

Acknowledgements

The authors are deeply grateful to Profs. H. Hahn, P. Zięba, Drs. Yu. Ivanisenko, and A. Gornakova for valuable suggestions and discussion. The work is partially supported by the state task of ISSP and CSC RAS, the National Science Centre of Poland (grant OPUS 2014/13/B/ST8/04247), by the Russian Foundation for Basic Research (grants 18-03-00067, 19-58-06002). The part of research has been performed within the Accredited Testing Laboratories with certificate No. AB 120 issued by the Polish Centre of Accreditation according to European standard PN-ISO/IEC 17025:2005 and EA-2/15.

ENHANCED MICROSTRUCTURE AND MECHANICAL PROPERTIES OF SiC PARTICLE REINFORCED ALUMINIUM ALLOY COMPOSITE MATERIALS

Manoj Kumar Pal[1)], Arnav Vikram[2)], Vineet Bajaj[3)]*
[1)] Institute of Physical Metallurgy, Metal Forming, and Nanotechnology, University of Miskolc, Hungary-3515
[2)] Department of Mechanical Engineering, IST, Delhi-NCR Campus, Modinagar, India-201204
[3)] Department of Civil Engineering, SRM University, Delhi-NCR, Sonipat, Haryana, India-131029

Received: 21.06.2019
Accepted: 24.09.2019

[*]Corresponding author: e-mail: manojsantosh2002@gmail.com Tel.: +36204467103, Institute of Physical Metallurgy, Metal Forming, and Nanotechnology, University of Miskolc, Hungary

Abstract
Aluminium6061 alloy composites containing various volume fractions of Silicon Carbide (SiC) particles (0, 5%, 10%, 15%, 20% and 25%) were prepared by stir casting method. In the current study, microstructures and mechanical properties of cast silicon carbide (SiC) reinforced aluminum matrix composites (AMCs) were investigated. Optical microscopic examination, SEM, tensile strength test, hardness test and elongation test were carried out. The results showed that with the addition of SiC reinforcements in Aluminum6061 matrix increased hardness and tensile strength however, decreased elongation at 25% SiC reinforced AMC. Hardness and tensile strength were observed to be are maximum at 25% SiC and elongation is minimum at 25% SiC. Microstructural observation confirmed clustering and homogeneous distribution of SiC particles in the Al6061 matrix.

Keywords: Metal Matrix Composites, Aluminium Alloy 6061, Silicon Carbide, SEM

1 Introduction

High strength, low specific density and good wear resistance are the main keys of the Aluminium matrix composites with incorporation of fourth alloying materials fibers or particles and whiskers. The metal reinforced aluminium matrix composites are economical but also have good mechanical properties [1]. Many methods are available for fabrication of particulate reinforced metal matrix composites (MMCs) such as powder metallurgy [1, 2], casting method [3], squeeze casting [4] and compo-casting.

Several researchers have reported that the use of hard particles (Al_2O_3 or SiC) in aluminum alloys improve the mechanical properties of these alloys **[**5**].** Tensile strength, hardness and elongation are main big problem for aluminium alloy matrix. There is no general relationship established between mechanical properties (Tensile strength, hardness and elongation) microstructural factors and processing parameters. Recent studies revealed that the strength of matrix interface and mechanical properties of matrix materials affected by the addition in the volume fraction, and spatial distribution of second phase particles [6].

A non-metallic ceramic such as SiC, Al_2O_3, SiO_2, B_4C, Al-N are used in an AMC matrix because of pure aluminium or an alloy of it. Aluminium alloys are used in AMC due to high corrosion resistivity, high damping capacity, low density and good electrical and thermal conductivities [7]**.** SiC, Boron and Al_2O_3 particles are affected in tensile strength, hardness and elongation behavior

DOI 10.12776/ams.v25i4.1359 p-ISSN 1335-1532
e-ISSN 1338-1156

of MMCs. However, a limited number of researches have been reported on the abrasion behavior of ceramic particle reinforced aluminium alloy composites [1].
The purpose of the current study is to: (a) produce particle-reinforced metal matrix composites by stir casting method and; (b) measure the density, hardness and ultimate tensile strength, elongation and microstructure of the composites.

2 Experimental Procedures

Aluminum metal matrix composites were prepared at various volume fractions of SiC particles fabricated by stir casting method. Aluminium6061 alloy was used as the matrix material and SiC particles were used as the reinforcement material. The SiC in the experiments was supplied by Norton Co. The composite was prepared by stir casting method for fabrication which gives the uniform distribution of reinforcement particle. Silicon carbide, which is used as a mesh with the particle size of 200/+300 (particle size is below 74μm and above 53μm). It is a very fine powder in appearance and has high hardness value therefore; silicon carbide is used for reinforcement purpose in powdered form. In the present study, the chemical composition of Aluminium 6061 alloy used is presented in **Table 1**.

Table 1 Nominal Chemical Composition of Aluminium Alloy (Al6061)

Elements	Si	Cu	Ni	Zn	Sn	Mn	Mg	Pb	Fe	Cr	Ti	Al
%	0.43	0.24	0.05	0.25	0.001	0.139	0.802	0.24	0.7	0.25	0.15	Balance

In this process of fabrication, a dispersed phase and a molten metal matrix are mixed together with the help of mechanical stirring. Firstly, Aluminium6061 is taken in the form of plates. These plates were then placed in a graphite crucible chamber and heated using the electrical resistance furnace. The temperature of the furnace is set at 750°C. Once Aluminium6061 is completely melted, silicon carbide which is in form of powder was poured into the same crucible chamber with different percentages and temperature was gradually increased to 1000°C. While pouring the reinforcing material into the matrix material; a constant speed of 300 rpm with the help of mechanical stirrer was maintained to create a vortex. The stir was carried out for approximately 30 minutes to obtain a uniform mixture. Afterwards, molten MMC is poured into a sand cast to obtain MMC pipe. The cast was quenched with water in order to cool down MMC quickly. This procedure was repeated for silicon carbide at various volume fractions of 5%, 10%, 15%, 20% and 25% [6, 8, 9, 10].
To investigate the microstructure of the specimens, 1000 and 1200 grit papers were used in grinding for preparing the specimen surfaces. Then 3μm diamond paste was used for the polishing [10]. Etching was done with the help of Keller's reagent in order to conduct micro structural testing and the mechanical characterization. The etched specimen was observed under both, optical microscope as well as scanning electron microscope.

3 Results and Discussion

3.1 Microstructure

The grain size of the aluminium composites was smaller than that of the aluminum alloy and the grain size of composites decreases with the increase of volume fraction of SiC. It was observed that major portion of SiC particles segregated along the grain boundaries. At the melting stage and the solidification stage, the microstructures of the composites were investigated. The ultrasonic treatment dispersed SiC particles at the melting stage [9].

DOI 10.12776/ams.v25i4.1359 p-ISSN 1335-1532
e-ISSN 1338-1156

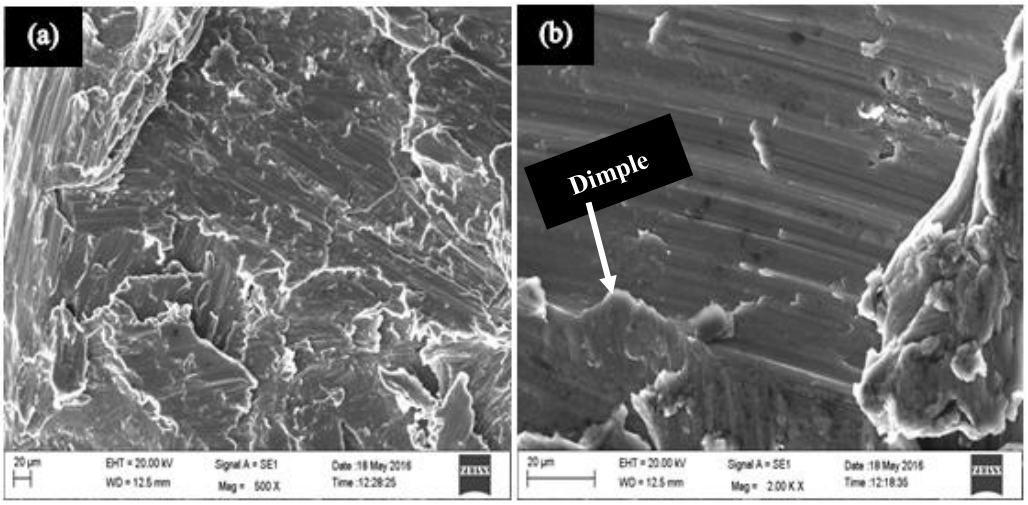

Fig. 1 SEM micrograph (a) Distribution of Al6061/5%SiC composite (b) Fractured surface of Al6061/10%SiC composite

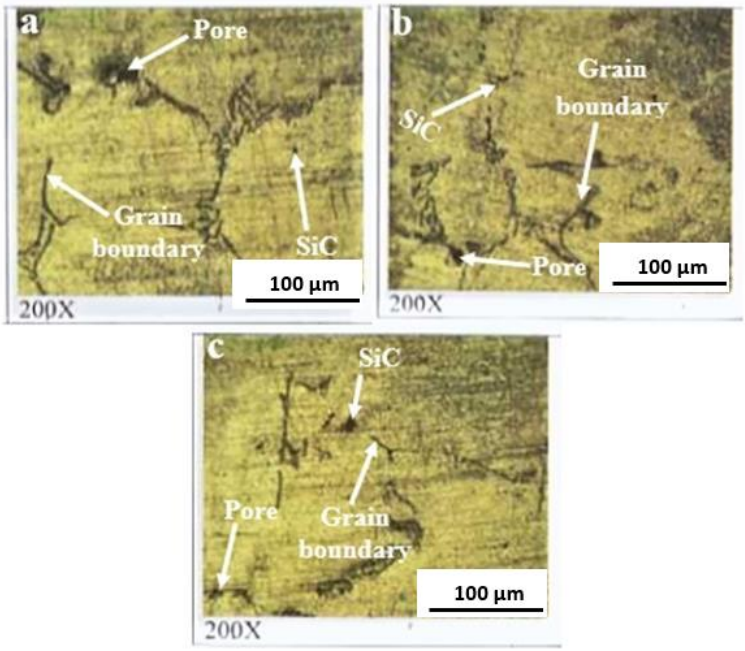

Fig. 2 Optical images (a) Al6061/5%SiC composite (b) Al6061/10%SiC composite (c) Al6061/15%SiC

It is clearly observed that most of SiC particles are dispersed in the aluminium i.e. uniform distribution of the SiC on each composite particle surface. When composite powders are used for the melting, Al6061 start to melt, firstly on the outer surface and then on from the inside while gradually releasing the SiC particles into the molten mix which is evident from a good distribution in the melt [11].

DOI 10.12776/ams.v25i4.1359 p-ISSN 1335-1532
e-ISSN 1338-1156

Fig. 1 depicts SEM fracture surfaces of the composite with the volume fraction of the SiC particles of 5% and 10%, respectively. A typical ductile fracture can be observed in the **Fig. 1** with numerous dimples over the entire surface are visible and it shows both the ductile and brittle fracture. All these fracture surfaces have dimples in the matrix and de-cohesion of SiC particles in the matrix. The reason of dimples is the void nucleation and subsequent coalescence because of a strong shear deformation and fracture on the shear plane are the primary reasons for cause of such dimples. It can also be seen that increasing the volume fraction of the SiC particles decreases the ductility of the material while it increases the brittle behavior of material. This is the major difference between the fracture surfaces [12, 13].

Fig. 2 shows the optical microstructures of the composites with 5%, 10% and 15% volume fractions of the SiC particles. It is evident from the **Fig. 2** shows that 5%, 10% and 15% volume fractions of the SiC particles are uniformly distributed in the Al matrix. Also, SiC pores and grain boundaries can be observed in the aluminum composites as evident in **Fig. 2**, the pores are evident and there is an increase in the pore percentage with an increase in the SiC particles which indicates that the interfacial cohesion is weak between the SiC particles and matrix [9].

3.2 Mechanical properties

Table 2 shows the mechanical properties of the composite as a function of the volume fraction of the SiC particles. It also illustrates that with an increase in the volume fraction of the SiC particles, there is an increase in both tensile strength as well as hardness. While the elongation decreases with an increase in the volume fraction of the SiC particles. Increase in the strength of the composites but degradation the plasticity of the composites with increase in SiC particles has been reported earlier [14, 15, 16]**.**

Table 2 Mechanical properties of composites (Al6061/vol% SiC)

Volume fraction of SiC particles (%)	Tensile Strength (MPa)	Vickers Hardness (VH)	Elongation (%)
0	82	23.50	24.3
5	93	37.25	15.2
10	99.5	42.3	11.4
15	113	44.10	9.1
20	128	46.23	6.9
25	145	47.3	5.7

In general, a decrease in the plasticity but an increase in the strength of composites with addition of SiC particles can be related to formation of micro crack formed during deformation. Also SiC has high strength but is brittle in nature. It was observed that two types of the micro cracks were initiated by the addition of SiC particles. First interfacial cohesion is strong while the second interfacial cohesion is weak between SiC and matrix. In first condition, at high stress concentration, the local strain and dislocation density reached the critical values and the SiC particles fractured to nucleate micro-cracks while in second condition, before the SiC particles could fracture, the SiC particles and matrix happened to nucleate micro-cracks. SONG et al [9] reported similar kind of results from 2008 to 2015.

Table 2 shows the experimental data and it can be seen from the data that elongation of the composites decreases with the volume fraction of the SiC particles. Decrease in the elongation of the composites can be achieved by the decrease in the dislocation slip distance with the increase in the volume fraction of SiC particles [10].

DOI 10.12776/ams.v25i4.1359 p-ISSN 1335-1532
e-ISSN 1338-1156

Fig. 1 shows a typical SEM image of the fabricated composite with 5% and 10% SiC volume fraction. In this composite, pores are uniformly distributed in the matrix. Appearance of pores in the matrix (due to the low die-pressing pressure) reduced the plasticity of the composites and is predominant in initiation of the micro crack formed during deformation [17, 18]**.**

There is an increase in the average hardness of composite with an increase the amount of SiC particulate. But this SiC can be allocated to (a) the presence of harder SiC particles and (b) during indentation, higher restrictions to the localized matrix deformation. So the presence of stronger and stiffer particles accommodate in preventing localized plastic deformation of the matrix during micro-hardness indentation [19].

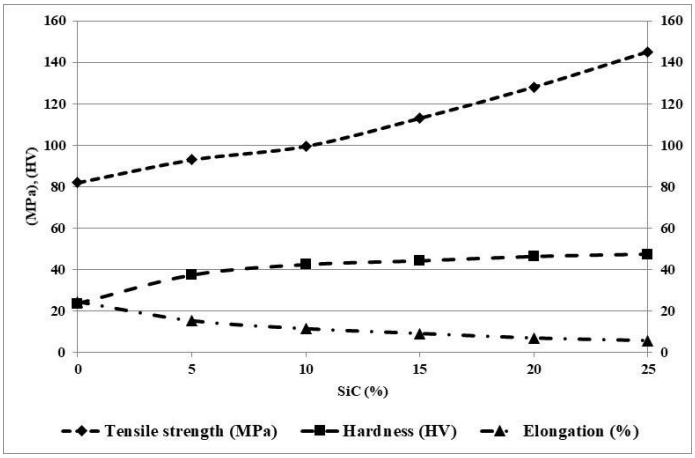

Fig. 3 Mechanical properties of composites (Al6061/vol% SiC)

The micro hardness of composite means the interface bonding between reinforcing particles and matrix. **Table.1** shows the Vickers hardness values of composite for varying volume fraction of SiC reinforcement. **Table.1** also shows the addition of SiC particles in Al6061 matrix composites and **Fig. 3** shows that the hardness is increased with an increase in volume fraction of SiC. The presence of harder and well bonded SiC particles in Al matrix that impede the movement of dislocations increases the hardness of AMCs [20, 21]**.**

4 Conclusions

Al6061 with varying SiC content (0%, 5%, 10%, 15%, 20% and 25% volume fraction) were prepared by stir casting method. Microstructure and mechanical properties (hardness, tensile strength and elongation) characteristics of the prepared composites were investigated. Based on experimental evaluation, following conclusions are evaluated:

1. A stir casting route was developed for the metal matrix composites by adding SiC particles. Various sizes of MMCs could be produced successfully by stir casting method consisting of 10% and 25% volume fraction of SiC particles.
2. Clustering and homogenous distribution of SiC particles in Al6061 matrix were observed in the microstructures.
3. The increase in compressive strength hardness of composite due to the addition of SiC particles because SiC is harder than Al6061 matrix.
4. Mechanical properties (tensile strength and Vickers hardness) of composites increased and elongation is decreased as increased of volume fraction of SiC. **Fig. 3** confirmed that

DOI 10.12776/ams.v25i4.1359 p-ISSN 1335-1532
e-ISSN 1338-1156

tensile strength and Vickers hardness are maximum 25% SiC content and elongation is lower at 25% SiC content AMC.

References

[1] M. O. Bodunrin, K. K. Alaneme, L. H. Chown: J. Mater. Res. Technol., Vol. 4, 2015, p. 434–445, https://doi.org/10.1016/j.jmrt.2015.05.003
[2] M. K. Pal, G. Gergely, D. K. Horvath, Z. Gacsi: Arch. Metall. Mater., Vol. 64, No. 2, 2019, p. 603-606, http://dx.doi.org/10.24425/amm.2019.127585
[3] M. K. Pal, G. Gergely, D. K. Horvath, Z. Gacsi: Powder Metallurgy Progress, Vol. 18, No. 1, 2018, p. 049-057, http://dx.doi.org/10.1515/pmp-2018-0006
[4] M. T. Sijo, K. R. Jayadevan: Procedia Technol., Vol. 24, 2016, p. 379–385, https://doi.org/10.1016/j.protcy.2016.05.052
[5] S. Gopalakrishnan, N. Murugan: Compos. Part B Eng., Vol. 43, No. 2, 2012, p. 302–308, https://doi.org/10.1016/j.compositesb.2011.08.049
[6] Y. Sahin: Materials & Design, Vol. 24, 2003, p. 671–679, https://doi.org/10.1016/S0261-3069(03)00156-0
[7] H. Kala, K. K. S. Mer, S. Kumar: Procedia Mater. Sci., Vol. 6, 2014, p. 1951–1960, https://doi.org/10.1016/j.mspro.2014.07.229
[8] H. Uzun: Mater. Des., Vol. 28, 2007, p. 1440–1446, https://doi.org/10.1016/j.matdes.2006.03.023
[9] M. Song and B. Huang: Mater. Sci. Eng. A, Vol. 488, 2008, p. 601–607, https://doi.org/10.1016/j.msea.2008.03.022
[10] H. R. Ezatpour, S. A. Sajjadi, M. H. Sabzevar, Y. Huang: Mater. Des., Vol. 55, 2014, p. 921–928, https://doi.org/10.1016/j.matdes.2013.10.060
[11] L. J. Zhang, F. Qiu, J. G. Wang, Q. C. Jiang: Mater. Sci. Eng. A, Vol. 626, 2015, p. 338–341, https://doi.org/10.1016/j.msea.2014.12.089
[12] M. J. Shen, X. J. Wang, T. Ying, K. Wu, W. J. Song: J. Alloys Compd., Vol. 686, 2016, p. 831–840, https://doi.org/10.1016/j.jallcom.2016.06.232
[13] M. Kok: J. Mater. Process. Technol., Vol. 161, 2005, p. 381–387, https://doi.org/10.1016/j.jmatprotec.2004.07.068
[14] M. H. Rahman, H. M. M. Al Rashed: Procedia Eng., Vol. 90, 2014, p. 103–109, https://doi.org/10.1016/j.proeng.2014.11.821
[15] N. Parvin, R. Assadifard, P. Safarzadeh, S. Sheibani, P. Marashi: Mater. Sci. Eng. A, Vol. 492, 2008, p. 134–140, https://doi.org/10.1016/j.msea.2008.05.004
[16] H. Abdizadeh, R. Ebrahimifard, M. A. Baghchesara: Compos. Part B Eng., Vol. 56, 2014, p. 217–221, https://doi.org/10.1016/j.compositesb.2013.08.023
[17] R. Taherzadeh Mousavian, R. Azari Khosroshahi, S. Yazdani, D. Brabazon, A. F. Boostani: Mater. Des., Vol. 89, 2016, p. 58–70, https://doi.org/10.1016/j.matdes.2015.09.130
[18] G. B. Veeresh Kumar, C. S. P. Rao, N. Selvaraj: Compos. Part B Eng., Vol. 43, 2012, p. 1185–1191, https://doi.org/10.1016/j.compositesb.2011.08.046
[19] X. L. Zhong, M. Gupta: Journal of Physics D, Vol. 41, 2008, p. 1-7, http://iopscience.iop.org/0022-3727/41/9/095403
[20] K. C. Mohanakumara, H. Rajashekar, S. Ghanaraja, S. L. Ajitprasad: Procedia Mater. Sci., Vol. 5, 2014, p. 934–943, https://doi.org/10.1016/j.mspro.2014.07.381
[21] X. J. Wang et al.: Mater. Des., Vol. 57, 2014, p. 638–645, https://doi.org/10.1016/j.matdes.2014.01.022

DOI 10.12776/ams.v25i4.1359 p-ISSN 1335-1532
e-ISSN 1338-1156

VISCOSITY AND ELECTRICAL RESISTIVITY OF LIQUID CuNiAl, CuNiAlCo, CuNiAlCoFe ALLOYS OF EQUIATOMIC COMPOSITIONS

Olga Chikova[1)], Vladimir Tsepelev[1)], Vladimir V'yukhin[1)], Kseniya Shmakova[1)], Vadim Il'in[1)]*
[1)] *Ural federal university, Yekaterinburg, Russia*

Received: 25.09.2019
Accepted: 31.10.2019

[*]*Corresponding author:e-mail:chik63@mail.ru, Department of Physics, Ural federal university, Mira str., 19, Yekaterinburg, Russia*

Abstract
The kinematic viscosity and electrical resistivity of equiatomic liquid alloys CuNiAl, CuNiAlCo, CuNiAlCoFe has measured during heating of the sample to 2070 K and subsequent cooling. We consider CuNiAl, CuNiAlCo, CuNiAlCoFe alloys of equiatomic compositions as the multi-principal element alloys (MPEAs), the complex concentrated alloys (CCAs), the high-entropy alloys (HEAs). The measuring results of the vickosity and the resistivity are discussed on base the available microgeterogenity concept. We searched the temperatureT*of the heating a melt for destroy of microheterogeneity. T* is the temperature of the beginning of the matching portion of the temperature dependence of the viscosity and resistivity which is obtained by heating and cooling. All the investigated melts demonstrated different temperature dependence of viscosity for heating and cooling. The temperature T*=1800 K were determined only for liquid alloy CuNiAl of equiatomic composition. For alloys CuNiAlCo, CuNiAlCoFe the coinciding part of the temperature dependences of the viscosity which are obtained by heating and cooling is absent. The results of viscosity are discussed within the theory of absolute reaction rates. Entropy of activation of viscous flow and free activation energy of viscous flow were determined by analyzing the temperature dependences of kinematic viscosity. The increasing of components quantity in the alloy leads to the increasing of the free activation energy of viscous flow and the volume per structural unit of the melt (ion, atom, or cluster). The measuring results of resistivity were interpreted using the Nagel-Tauc model. The temperature coefficient of resistivity (characteristic of the structural state of the melt) was determined. The temperature dependences of the CuNiAl liquid alloy resistivity measured upon heating to 2070 K and subsequent cooling do not coincide.The value of T*temperature for alloy CuNiAl of equiatomic composition is 1850 K. For CuNiAlCo, CuNiAlCoFe alloys the temperature dependences of the resistivity which are obtained by heating and cooling are coinciding. This means that destroy of microheterogeneity for melts after heating up to 2070K did not occur. The temperature coefficient of resistivity of the CuNiA liquid alloy irreversibly decreases when it heated to a temperature of 1850 K.This is evidence of the destruction of microheterogeneity with the formation of a homogeneous solution at the atomic level. The increasing of components quantityin the alloy leads to a decreasingof thetemperature coefficient of the resistivity (in cooling moda). According to the ideas of Nagel and Tauk, an irreversible decrease of the temperature coefficient of the specific resistance of the melt indicates an increase in the volume per structural unit of the melt (ion, atom, or cluster)

Keywords: multi-principal element alloys (MPEAs), complex concentrated alloys (CCAs), high-entropy alloys (HEAs), melts, microheterogeneity, viscosity, resistivity

DOI 10.12776/ams.v25i4.1358 p-ISSN 1335-1532
e-ISSN 1338-1156

1 Introduction

CuNiAl, CuNiAlCo, CuNiAlCoFe alloys of equiatomic compositions are the multi-principal element alloys (MPEAs), the complex concentrated alloys (CCAs), the high-entropy alloys (HEAs). The fields of MPEA, CCA, HEAs have expanded and now include microstructures with any number of phases and phases of any type.The scope of their application includes both structural and functional materials [1-6]. Regardless of classification, the researchers are based on the study of structure-properties and processing relations in these multicomponent alloys with the aim to surpass the physical properties of conventional materials [7]. Currently, two concepts HEA are being formulated: the 'entropy effect' and the 'sluggish diffusion' [1,2]. The effects of entropy on the structure and properties of alloys are summarized in terms of thermodynamics, kinetics, and size and position of atoms [1,3]. "The sluggish diffusion effect" of the HEA leads to the low coarsening rate of solid phase compared with other conventional alloys [2]. A rationale for the HEAs is that the configurational entropy contribution to the total free energy in alloys with five or more major elements can stabilize the solid-solution state relative to multiphase microstructures. It is important factor in the obtaining of high-entropy alloys is the high cooling rate of metal during crystallization which makes it impossible to disintegration of solid solution and formation of chemical compounds.

Most of the HEA research focused on alloy design, microstructural characterization, and mechanical testing rather than manufacturing, processing, and industrialization, although the properties, microstructures, and performance are strongly dependent on processing. The manufacturing process of HEAs can be classified into three main routes: liquid processing, mechanical alloying, and mixing elements of the vapour state [8]. In this article, we aim to describe the liquid of processing, the cast manufacturing processes applied to HEAs. High-entropy alloys (HEAs) can have either high strength or high ductility; a simultaneous achievement of both at the same time is still a difficult task. The inferior cast ability and compositional segregation of HEAs are also obstacles for their technological applications. To solve these problems we proposed a novel strategy to design HEAs using the microgeterogenity concept. This concept is basedon numerous experimental data which indicate that at temperatures higher than the liquidus temperatures multicomponent metallic alloys can have microheterogeneities, the chemical composition of which differs from the composition of the surrounding melt for a long time [9]. To destroy of the microheterogeneity a liquid metal should be overheated to the temperature that is certain for each composition. After this action the melt irreversibly transforms into the state of the true solution which substantially changes the conditions of its solidification.Thehighcooling rate of metal which is technically difficult to ensure can be replaced by the destruction of the microinhomogeneity of the liquid HEA before crystallization. It is known that subsequent cooling and crystallization even at relatively low cooling rates (1-10 K/s) enables to obtain a microstructure similar to the microstructure that is formed at high cooling rates.

Alloys of the Cu – Ni – Al – Co – Fe system are the subject of extensive structural studies [10-11], nevertheless, the properties of the liquid state of these alloys [12-14] associated with their processing arelittlestudied. For example, the density of the liquid equiatomic AlCoCrCuFeNi alloy as well as the quaternary AlCoCuFe alloy was determined over a wide temperature range [12]. The viscosity of CuNiAl liquid alloys was studied using the oscillating crucible method [13] and the enthalpy of mixing ΔH of liquid ternary CuNiAl alloys at 1700 K was measured using a high-temperature mixing calorimeter [14]. The values the electrical resistivity and viscosity of liquid Cu-Nibinary alloys were measured [15-16].Similar results for the ternary system Cu-Ni-Al are not known to the authors.

DOI 10.12776/ams.v25i4.1358 p-ISSN 1335-1532
e-ISSN 1338-1156

In this work we based on the available microgeterogenity concept. The liquid AlCuNi, AlCuNiCo, AlCuNiCoFe alloys have been qualitatively studied by measuring the viscosity and resistivity during the heating/cooling process. The results of viscosity and resistivity measurements of the CuNiAl, CuNiAlCo, CuNiAlCoFe melts equiatomic composition are important for cast industry also.

2 Experimental material(s) and methods

The samples CuNiAl, CuNiAlCo and CuNiAlCoFe alloys equiatomic composition were obtained by vacuum arc melting at laboratory. High purity metals, i.e., aluminum of A999 special purity grade, 99.9%, copper of the Mk00 brand (99.98%) and carbonyl iron (special purity grade, 99.98%) were applied as initial materials.

The kinematic viscosity was measured using by the oscillating cylinder method during heating and subsequent cooling. The measurements were carried out in the liquidus temperature range up to 2070 K with an isothermal delay at least 30 min with relatively small (50 K) stepwise temperature changes. A set temperature was maintained accurate to 1K using a high-precision controller. The vibration parameters were measured optically using aphoto recording system of vibrations. We used BeO crucibles in all experiments. All the experiments were carried out in a high-purity helium atmosphere at a pressure of 10^5 Pa.We did not observe signs of melt evaporation and a decrease in the sample mass. The kinematic viscosity was measured using the unit described in [17]. The systematic error of measuring viscosity was 3%, including a random error of no higher 1.5% at a confidence level 95%.

The resistivity ρ of liquid CuNiAl, CuNiAlCo and CuNiAlCoFe alloys equiatomic composition were measured using the rotating magnetic field method during heating to 1830K and subsequent cooling. A working chamber was initially evacuated to 0,001 Pa, and then filled with helium to a pressure of 10^5 Pa. Samples were kept in the chamber with an inert atmosphere for 5-8 min at the melting temperature and then heated to 1830K at a step of 30-50K. Isothermal holding at the measurement points was at least 15 minutes. The electrical resistivity was measured using the unit described in [18]. The estimation of the error in the measurementof resistivity by the technique described in [1] showed that the total relative error was about 3% when using BeO crucibles. The systematic error in theresistivity measurement was 5%, including the random error no higher 2% at a confidence level of 95%.

3 Results and discussion

Figures 1-3 show the results of a viscosimetric study of liquid alloys CuNiAl, CuNiAlCo, CuNiAlCoFe of equiatomic composition. All the studied melts demonstrate different temperature dependences of viscosity when heated to 2070 K and cooled, i.e., a hysteresis. The temperature T* is the temperature of the beginning of the coinciding part of the temperature dependence of the viscosity which is obtained by heating and cooling. The value of temperature T* for alloy CuNiAl of equiatomic composition is 1800 K (**Fig. 1**). For CuNiAlCo, CuNiAlCoFe alloys, the coinciding part of the temperature dependences of the viscosity obtained during heating and cooling is absent (**Fig. 2-3**). We showed that the hysteresis appears only when the CuNiAlCo alloy is heated to 2070 K (**Fig. 2**). This means that destruction of microheterogeneity and the transition of the melt state intothe true solution after heating to 2070 K for CuNiAlCo, CuNiAlCoFe alloys did not occur. It is interesting to note that viscosity values for all studied melts during cooling were equal to or higher than the corresponding values recorded during heating (**Fig. 1-3**). The most significant

DOI 10.12776/ams.v25i4.1358 p-ISSN 1335-1532
e-ISSN 1338-1156

increase in the viscosity at low temperatures (near liquidus) is characteristic for CuNiAlCoFe melt. An increase in melt viscosity during cooling in a microinhomogeneous state can explained by process of dispersion of microheterogeneities. The changes in viscosity occurred non monotonically when heating of the liquid alloys CuAlNi, CuNiAlCoFe. The temperature dependency of viscosity for cooling is monotonic and obeys an Arrhenius law $\nu = A\exp(E/RT)$ for all alloys (**Fig. 4**). Our attention was focused on changing the characteristics of the viscous flow of melts. The activation energy of viscous flow E and the entropy factor A in the Arrhenius equation change when a liquid alloy is heated to the temperature T* (T*- is temperature of structural transformations).

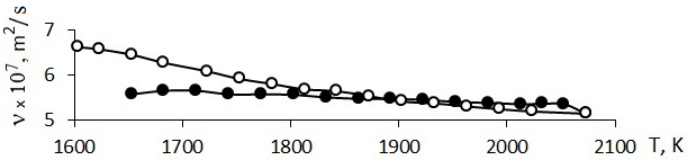

Fig. 1 The temperature dependences of the kinematic viscosity of the CuNiAl melts (●- heating, ○ – cooling)

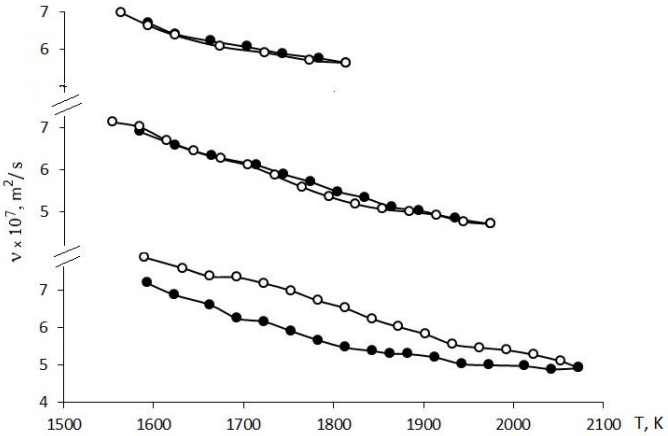

Fig. 2 The temperature dependences of the kinematic viscosity of the CuNiAlCo melts (●- heating, ○ – cooling)

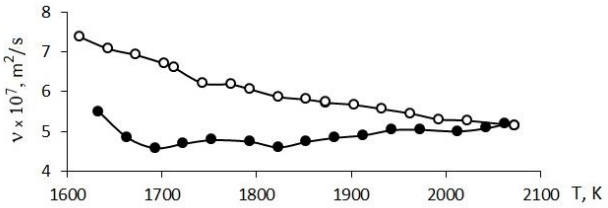

Fig. 3 The temperature dependences of the kinematic viscosity of the CuNiAlCoFe melts (●- heating, ○ – cooling)

According to absolute reaction rate theory [19], themelt viscosity is described by the equation: $\nu = \frac{hN_A}{\mu}\exp(\Delta G^{\neq}/RT) = \frac{hN_A}{\mu}\exp(-\frac{\Delta S^{\neq}}{R})\exp(\frac{\Delta H^{\neq}}{RT})$, where h-Planck's constant,N_a-Avogadro, $\Delta G^{\#}$-the

DOI 10.12776/ams.v25i4.1358 p-ISSN 1335-1532
e-ISSN 1338-1156

free activation energy ofviscous flow, μ-Molar mass, $\Delta H^{\#}$-the enthalpy of activation of viscous flow, $\Delta S^{\neq}$-the entropy of activation of viscous flow, R-the universal gas constant andT-temperature. The Entropy factor in the Arrhenius equation $A = \frac{hN_A}{\mu}\exp(-\frac{\Delta S^{\neq}}{R})$ depends on the entropy of viscous flow$\Delta S^{\#}$. We calculated the free activation energy of viscous flow$\Delta G^{\#}$and the entropy of activation $\Delta S^{\#}$ of viscous flow for all liquid alloys upon cooling (**Table 1**).Increasing of components quantity in melt leads to increasing of the free activation energy of viscous flow$\Delta G^{\#}$ and the entropy of activation of the viscous flow $\Delta S^{\#}$. In accordance [16, 20] entropy factor A in the Arrhenius equation is presented in this work as a function of volume per melt structural unit (ion, atom, or cluster) υ: $A = \frac{h}{\upsilon \cdot d}$. The volume per structural unit of the melt (ion,atom, or cluster) is in this case $\upsilon = \frac{h}{A \cdot d} = \frac{\mu}{N_A \cdot d} \cdot \exp(\frac{\Delta S^{\#}}{R})$, where d is the density of the melt.Thus, an increase in the number of components in the alloy leads to an increase in the free activation energy of viscous flow $\Delta G^{\neq}$ and volume per structural unit of the melt (ion, atom, or cluster) υ.

Table 1 The free activation energy of viscous flow $\Delta G^{\neq}$, and the entropy of activation of viscous flow $\Delta S^{\#}$ for melts upon cooling

The alloy	The entropyof activation of viscousflow $\Delta S^{\#}$(J·K^{-1})	The free activation energy of viscous flow $\Delta G^{\#}$, (kJ·mol^{-1}K^{-1})
CuNiAl	-26.65	15.96
CuNiAlCo	-24.30	22.05
CuNiAlCoFe	-21.48	27.29

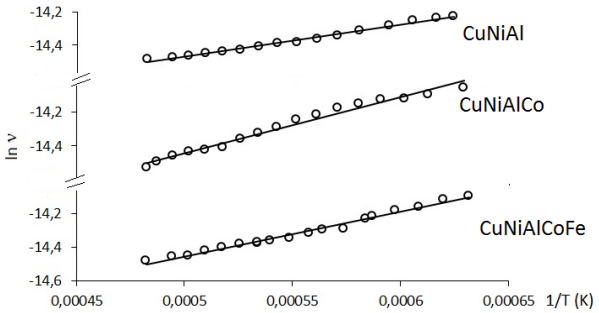

Fig. 4 The dependences of lnν (1/T) for melts upon cooling

Fig. 5 shows results of the resistivity study of liquid alloys CuNiAl, CuNiAlCo, CuNiAlCoFe equiatomic composition. The liquid alloy CuNiAl demonstrates a different temperature dependence of the resistivityfor heating and cooling, i.e., a hysteresis (**Fig. 5**).The temperature value T* for the CuNiAlalloy of equiatomic composition is 1850 K (**Fig. 5**). For CuNiAlCo, CuNiAlCoFe alloys the temperature dependences of the resistivity obtained by heating and cooling coincide. This means that the transition of the state of the melt intothe true solution does

DOI 10.12776/ams.v25i4.1358 p-ISSN 1335-1532
e-ISSN 1338-1156

not occur after heating to 2070K. When the liquid alloy CuNiAl is heated, the resistivity ρ does not always linearly increase with temperature. The CuNiAl melt shoes a change in the temperature coefficient of resistivity for heating (**Fig 6, dotted line**). The reliability of approximation R^2 of the dependence ρ(T) in the heating mode from 1570 to 1770 K for CuNiAl alloy is anomalous - 0.17, and for the other dependences ρ(T), thevalues of $R^2$are 0.98-0.83. The value of R^2 characterizes the reliability of the approximation: the closer the value of R^2 to unity, the more reliable the trend line shows the process under study. The temperature range in which the destruction of microheterogeneity occurs was defined as1770 -1870 K.

The temperature coefficient of the resistivity dρ/dT for the CuNiAl alloy of equiatomic composition upon heating to the melt to the temperature of T* = 1850 K, accompanied by destruction of microheterogeneity and mixing components at the atomic level, irreversibly decreased from $0.025 \cdot 10^{-8}$ to $0.012 \cdot 10^{-8}$ Om·m·K^{-1} (**Fig. 6**).

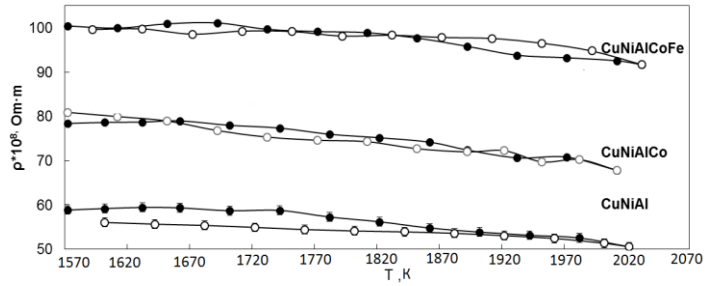

Fig. 5 The temperature dependences of the resistivity of CuNiAl, CuNiAl, CuNiAlCoFe equiatomic composition liquid alloys (●- heating, ○ – cooling)

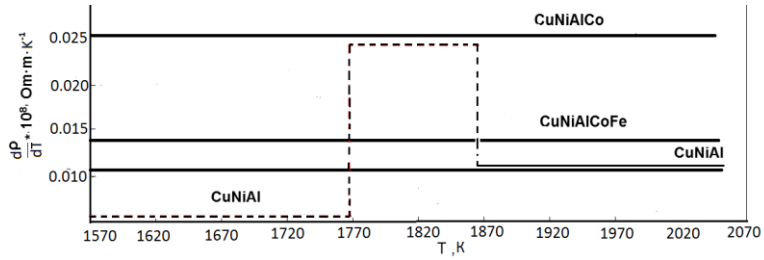

Fig. 6 The dependences of dρ/dT(T) for melts upon cooling. The dependences of dρ/dT(T) for CuNiAl melt upon heating (dotted line).

Also the increasing of components quantityin the alloy leads to a decreasing of the temperature coefficient of the resistivity (in cooling moda). A similar result was obtained earlier whenthe measuring electrical resistivity of liquid steel [18, 20]. As microheterogeneity is destroyed and components are mixed on an atomic scale in a liquid alloy, the number of conduction electrons z increases and, consequently, Fermi wave number $k_F = (3\pi^2 z/\Omega)^{1/3}$, where Ω is the crystallite volume. In this case, according to the Faber-Ziman theory, the determining factor is an increase in structure factor a($2k_F$). When doubled Fermi wave vector $2k_F$ becomes equal to the wave number corresponding to the position of the first peak of the structure factor ($2k_F$ =Kp), the resistivity becomes maximal. According to the Ziman theory, the temperature coefficient of resistivity is close to zero or negative in the region where $2k_F$ = Kp, since the height of the first

DOI 10.12776/ams.v25i4.1358 p-ISSN 1335-1532
e-ISSN 1338-1156

structure factor peak decreases with increasing temperature.It is remarkable that the $2k_F$=Kp condition is the basis of the Nagel-Tauc model which explains the high tendency of eutectic alloys to supercooling and the glass transition. According to this model when the condition $2k_F$ = Kp is fulfilled, a potential barrier appears fornucleation of crystallite, the melting temperature (eutectic temperature) of the alloy decreases, and the glass transition temperature increases [18, 20]. An increase in the supercooling of a liquid alloy is caused by an increase in the volume per structural unit of the melt (ion, atom, or cluster).

4 Conclusion

A promising method forproducing multicomponent alloys with a homogeneous structure is heating the melt for destroy microheterogeneity and mixing components at the atomic level, i.e. more than temperature T* for each composition. This method makes it possible to produce the bulk ingots with the required structure under conditions of natural gravitation even at fairly low cooling rates. After such overheating, the melt irreversibly goes into the state of the true solution, which substantially changes the solidificationconditions. Based on the available microgeterogenity concept the liquid CuNiAl, CuNiAlCo, CuNiAlCoFe alloys were qualitatively studied by measuring the viscosity and resistivity during the heating/cooling.

The results of viscosimetric study of CuNiAl, CuNiAlCo, CuNiAlCoFe liquid alloys of equiatomic composition show that temperature T* value for the CuNiAl alloy of equiatomic composition is 1800 K. For CuNiAlCo, CuNiAlCoFe alloys, the coinciding part of the temperature dependences of viscosity which are obtained upon heating to 2070 K and cooling, is absent. The results of the studyof resistivity of the liquid alloys CuNiAl, CuNiAlCo, CuNiAlCoFe of equiatomic composition show that the value of temperature T* for alloy CuNiAl of equiatomic composition is 1850 K. The temperature dependences of the resistivity of the liquid alloys CuNiAlCo, CuNiAlCoFe by heating and cooling is coincide. Heating of liquids alloys CuNiAlCo, CuNiAlCoFe above 2070 K is impossible,since intense evaporation of metal begins. Based on the available microgeterogenity concept of multicomponent liquid alloys and results of the measuring viscosity and resistivity, we assume that the heating the CuNiAl liquid alloy up to 1800 K and subsequent crystallization, even at relatively low speeds, provide witha more homogeneous structure volumetric ingots.

References

[1] D. B. Miracle, O. N. Senkov: Acta Materialia, Vol. 122, 2017, p. 448-511, http://dx.doi.org/10.1016/j.actamat.2016.08.081

[2] T. R. Paul, I. V. Belov, G. E. Murch: Materials Chemistry and Physics, Vol. 210, 2018, p. 301-308, http://dx.doi.org/10.1016/j.matchemphys.2017.06.039

[3] R.-X. Li, Y. Zhang,: Acta Physica Sinica. Vol.66, 2017, № 17, No. 177101, http://dx.doi.org/10.7498/aps.66.177101

[4] B. Cantor, I. T. H. Chang, P. Knight, A. J. B Vincent: Materials Science and Engineering A. Vol. 375-377, 2004, No. 1-2, p. 213-218, http://dx.doi.org/10.1016/j.msea.2003.10.257

[5] W. L. Wanget al: Liquid Scientific Reports, Vol. 6, 2016, № art. 37191, http://dx.doi.org/10.1038/srep37191

[6] W. L. Wang et al: Intermetallics, Vol. 77, 2016. p. 41-45, http://dx.doi.org/10.1016/j.intermet.2016.07.003

[7] N. Derimow, R. Abbaschian: Entropy, Vol. 20, 2018, No.11, No.890, http://dx.doi.org/10.3390/e20110890

DOI 10.12776/ams.v25i4.1358 p-ISSN 1335-1532
e-ISSN 1338-1156

[8] D. Yim, H. S. Kim: Journal of Korean Institute of Metals and Materials, Vol. 55, 2017, No. 10, p. 671-683, http://dx.doi.org/10.3365/KJMM.2017.55.10.671
[9] U. Dahlborg, M. Calvo-Dahlborg, D. G. Eskin, P. S. Popel: Springer Series in Materials Science, Vol. 273, 2018, p. 277-315, http://dx.doi.org/10.1007/978-3-319-94842-3_8
[10] Q. Zhang et al: Journal of Alloys and Compounds, Vol. 693,2017, p. 1061-1067, http://dx.doi.org/10.1016/j.jallcom.2016.09.271
[11] Y. X. Zhuang, W. J. Liu, Z. Y. Chen, H. D. Xue, J. C. He: Materials Science and Engineering A,Vol. 556, 2012, p. 395-399, http://dx.doi.org/10.1016/j.msea.2012.07.003
[12] Y. Plevachuk, J. Brillo, A. Yakymovych: Metallurgical and Materials Transactions A: Physical Metallurgy and Materials Science, Vol. 49, 2018,No.12, p. 6544-6552, http://dx.doi.org/10.1007/s11661-018-4925-4
[13] S. Mudry, V. Vus, A. Yakymovych: High Temperature Materials and Processes, Vol. 36,2017, No.7. p. 711-715, http://dx.doi.org/10.1515/htmp-2015-0190
[14] U. K. Stolz, I. Arpshofen, F. Sommer: ZeitschriftfuerMetallkunde/Materials Research and Advanced Techniques,Vol. 84, 1993, No.8. p. 552-556
[15] O. A. Chikova, G. A. Tkachuk, V.V. V'yukhin: Russian Journal of Physical Chemistry A, Vol. 93, 2019, No. 2, p. 198-203, http://dx.doi.org/10.1134/S0036024419020067
[16] F. Guo, T. Lu, J. Qin, H. Zheng, X. Tian: Physica B, Vol. 407, 2012, p. 4108–4113, http://dx.doi.org/10.1016/j.physb.2012.06.024
[17] O. A. Chikova, K. Y. Shmakova, V. S. Tsepelev: Russian Metallurgy (Metally), 2016, No. 3,p. 218-222, http://dx.doi.org/10.1134/S003602951603006X
[18] M. A. Borovykh, O. A. Chikova, V.S.Tsepelev, V. V. V'yukhin: Russian Metallurgy (Metally), Vol. 3, 2017, p. 175–178, http://dx.doi.org/10.1134/S0036029517030041
[19] O. A.Chikova, V. S. Tsepelev, O. P. Moskovskikh: Russian Journal of Physical Chemistry A. Vol.91, 2017, No. 6, p. 979–983, http://dx.doi.org/10.1134/S0036024417060061
[20] O. A. Chikova, N. I. Sinitsin, V.V. V'yukhin: Russian Journal of Physical Chemistry A. Vol. 93, 2019, No. 8,p. 1435–1442, http://dx.doi.org/10.1134/S0036024419080065

Acknowledgement

Authors are grateful for the support of experimental works by Act 211 Government Russian Federation, contract № 02.A03.21.0006.

FEATURES OF TEXTURE FORMATION IN POLYMORPHIC METALS BEING ELECTRODEPOSITED

Oleg B. Girin [1)], Volodymyr I. Ovcharenko [1)], Dmytro G. Korolyanchuk [1)]*
[1)] *Ukrainian State University of Chemical Technology, Materials Science Department, Dnipro, Ukraine*

Received: 30.05.2019
Accepted: 02.12.2019

[*]*Corresponding author: e-mail:* girin@ua.fm, *Materials Science Department, Ukrainian State University of Chemical Technology, 8 Gagarin Ave, Dnipro 49005, Ukraine*

Abstract
The aim of this work was further experimental verification of the existence of the phenomenon of electrochemical phase formation in metals and alloys via a supercooled liquid state stage. According to proposed idea the slowing down of the process of polymorphic transformation in a metal being electrodeposited should be accompanied by an intensive formation of the texture of the metastable modification and suppression of the texture development of the stable modification. The results of the texture analysis of electrodeposited cobalt as a model metal showed that under slowing down the polymorphic transformation process in a metal being electrodeposited, the texture formation is intensified in the metastable modification, but suppressed in the stable modification. The finding is another proof of the existence of the phenomenon of electrochemical phase formation in metals and alloys through a supercooled liquid state stage.

Keywords: electrochemical phase formation, electrodeposited cobalt, polymorphic transformation, texture

1 Introduction

The search for new methods and options for obtaining electrodeposited metals and alloys in the form of electrochemical coatings with improved physical-mechanical or chemical properties is hardly possible without information about their structure, texture, substructure, surface morphology and structural defects. Control of these structural characteristics that affect the properties of the resulting electrodeposited coatings is based on the concepts of the electrochemical phase formation of metals and alloys.

A previously unknown phenomenon of electrochemical phase formation in metals and alloys through a supercooled liquid state stage has been found relatively recently [1, 2]. The phenomenon occurs during the electrochemical deposition of metals or alloys in an aqueous medium onto a solid cathode, when a deeply supercooled metal liquid evolves in the form of multitude liquid atomic clusters that appear in an avalanche-like manner at various places near the cathode or the growing deposit, and then solidifies ultra-rapidly at the deposition temperature.

The discovered phenomenon is due to an extremely rapid, burst-like liberation of the metal or alloy, resulting from a chain reaction of electrochemical formation of atoms and transition of the atomic clusters or their associations from a liquid to a more stable solid state [1].

Later, numerous works ([3-6] are the most recent) were published, in which the occurrence of this phenomenon was experimentally proved.

DOI 10.12776/ams.v25i4.1357 p-ISSN 1335-1532
e-ISSN 1338-1156

The proposed concept is fundamentally different from the existing ones, according to which, the phase formation in electrodeposited metal or alloy occurs by embedding ions from an aqueous solution, or atoms formed on their surfaces, into their crystal lattice [7-11]. These concepts have received theoretical development in recent publications [12-15] on the electrochemical phase formation in metals and alloys.
Since the proposed concept of electrochemical phase formation in metals and alloys through a supercooled liquid state stage [1-6] has not yet received any objections or refutations, the authors continue to develop it with the introduction and implementation of new hypotheses and ideas.

2 Principal Hypothesis

It is known that in the process of solidification from the liquid state, the metallurgical polymorphic metals go through metastable phase states and crystallize as a modification that is stable under given thermodynamic conditions [16, 17]. If the phase transformation of a metastable modification into a stable one is slowed down or partially suppressed, a dual-phase state of the metal will eventually be formed. In the case of complete prevention of this phase transition, the solidified metal will stay in the metastable phase state.
The basic hypothesis of the experiments performed was that, in accordance with the phenomenon under discussion, the crystallization of a polymorphic metal being electrodeposited from the supercooled liquid state should be viewed as its sequential going through metastable modifications and, at the last stage of phase formation, emerging a modification that is stable under given deposition conditions.

3 Idea of Experiment

If polymorphic metals, being electrodeposited, indeed crystallize from the supercooled metallic liquid formed in the micro volumes near the surface of a deposit, then one can expect quite predictable features of the oriented grain growth in metastable and stable modifications in case the process of polymorphic transformation slows down during electrochemical phase formation. Specifically, in this case, the texturing of metastable modification of a polymorphic metal should intensify, while the texture development of a stable modification should be hindered.
The above texturing features in the metastable and stable modifications in the electrodeposits of polymorphic metals will testify to the phenomenon of electrochemical phase formation in metals and alloys through a supercooled liquid state stage.

4 The Aim and Objectives of the Study

The aim of this study was to further experimentally verify the existence of the phenomenon under discussion by investigating the features of texture formation in polymorphic metals. To achieve the object, the following tasks were set:

- qualitatively and quantitatively assess the crystallographic texture of metastable and stable modifications of a model polymorphic metal;
- investigate the change in the degree of texture perfection in each modification of the polymorphic metal under aggravating the conditions that slow down the phase transformation of the metastable modification into a stable one;
- compare the obtained dependences with the predicted changes in the texture of various modifications of the polymorphic metal in the case of slowing down the process of polymorphic transformation during the electrochemical phase formation;

DOI 10.12776/ams.v25i4.1357 p-ISSN 1335-1532
e-ISSN 1338-1156

- perform additional verification experiments to make sure that the obtained results were correctly interpreted.

5 Materials and Methods

5.1 Obtaining electrodeposited polymorphic metals

As a model polymorphic metal, cobalt was used that exists in two modifications: a metastable β-modification with a face-centered cubic lattice (β-Co), and a stable α-modification with a hexagonal close-packed lattice (α-Co). Cobalt coatings 20 μm thick were obtained by the method of electrodeposition at a temperature of 25 °C in a solution of the composition (g/l): $CoSO_4 \cdot 7H_2O$ – 300, H_3BO_3 – 40, NaCl – 20. The current density was changed over the interval from 0.5 to 10.0 A/dm^2, with the conventional adoption of 0.5-1.0 as mild, 1.5-6.5 as average and 7.0-10.0 A/dm^2 as hard electrodeposition conditions.

With an increase in the current density, the rate of electrochemical crystallization of cobalt increases [18], which in the case of an insignificant change in the current yield of cobalt leads to an increase in the amount of the metastable β-Co phase. Given the β-Co → α-Co polymorphic transformation in cobalt through the shear mechanism, an increase in the amount of the metastable β-Co modification will contribute to slowing down the process of polymorphic transformation.

5.2 Study of the textural and structural characteristics

The crystallographic texture of the electrodeposited cobalt was investigated using a modernized X-ray diffractometer DRON-2 (Russia) in Cr-K_α radiation. Preliminary experiments revealed that the cobalt coatings under study featured both the stable α-Co phase and metastable β-Co phase.

Given the two-phase structure of cobalt coatings, the preferred grain orientation in each phase was determined by a combination of direct pole figures. The technique involved recording texture-relevant curves of interference by {111} for β-Co and {10.1} for α-Co, which were then used to plot (111) and (10.1) direct pole figures for β- and α-modifications of cobalt, respectively. For the quantitative estimation of the degree of texture perfection of two-phase cobalt coatings, the average scattering angle of the texture in each modification was used.

The surface morphology of the coatings was studied using a scanning electron microscope REM-106I (Ukraine), operating in the mode of image formation by secondary electrons.

6 Results

As a result of the experiments performed, it was established that in all the modes of obtaining the coatings, both modifications of electrodeposited cobalt are textured. Moreover, a comparative analysis of texture-relevant curves of interferences by {111} for β-Co (**Fig. 1, a, c, e**) and interferences by {10.1} for α-Co (**Fig. 1, b, d, f**) shows that the texture axes do not change with an increase in the rate of cobalt coating deposition; it is only the degree of perfection of the preferred grains orientation that undergoes changes in each phase.

The analysis of direct pole figures (111) for β-modification (**Fig. 2, a**) and (10.1) for α-modification (**Fig. 2, b**) of electrodeposited cobalt showed that its texture is described by two axial orientations with [110] axis for β-Co and [11.0] for α-Co, perpendicular to the sample surface, and by a random component.

Indeed, the presence of the textural maximum of the axial orientation of the grains with the [110] axis at an angle of 35.3º in pole figure (111) for the β-modification of a two-phase cobalt sample (**Fig. 2, a**) in combination with the texture maximum of the axial orientation of the grains with the

DOI 10.12776/ams.v25i4.1357 p-ISSN 1335-1532
e-ISSN 1338-1156

[11.0] axis at an angle of 40.1° in (10.1) pole figure for the α-modification of the same sample (**Fig. 2, b**) allowed this conclusion. It should be noted that in the hexagonal close-packed system, where α-Co belongs, the [11.0] crystallographic direction and the (11.0) crystallographic plane are mutually perpendicular.

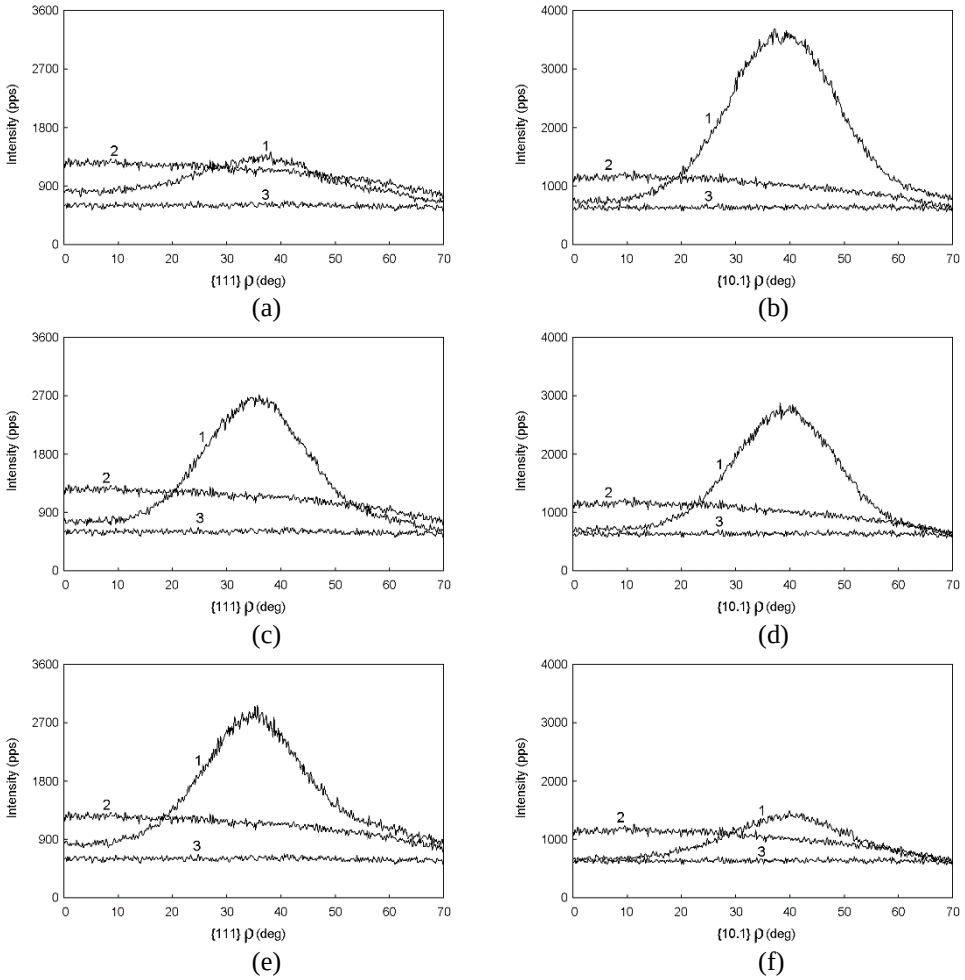

Fig. 1 Texture-relevant curves of interference by {111} for β-modification (a, c, e) and {10.1} for α-modification (b, d, f) of cobalt electrocoatings, obtained at a current density of 0.5 (a, b); 2.5 (c, d) and 10.0 A/dm^2 (e, f): 1 and 2 – texture curves for the coating and reference, respectively, 3 – background curve

Indeed, the presence of the textural maximum of the axial orientation of the grains with the [110] axis at an angle of 35.3° in pole figure (111) for the β-modification of a two-phase cobalt sample (**Fig. 2, a**) in combination with the texture maximum of the axial orientation of the grains with the [11.0] axis at an angle of 40.1° in (10.1) pole figure for the α-modification of the same sample (**Fig. 2, b**) allowed this conclusion. It should be noted that in the hexagonal close-packed system, where α-Co belongs, the [11.0] crystallographic direction and the (11.0) crystallographic plane are mutually perpendicular.

DOI 10.12776/ams.v25i4.1357 p-ISSN 1335-1532
e-ISSN 1338-1156

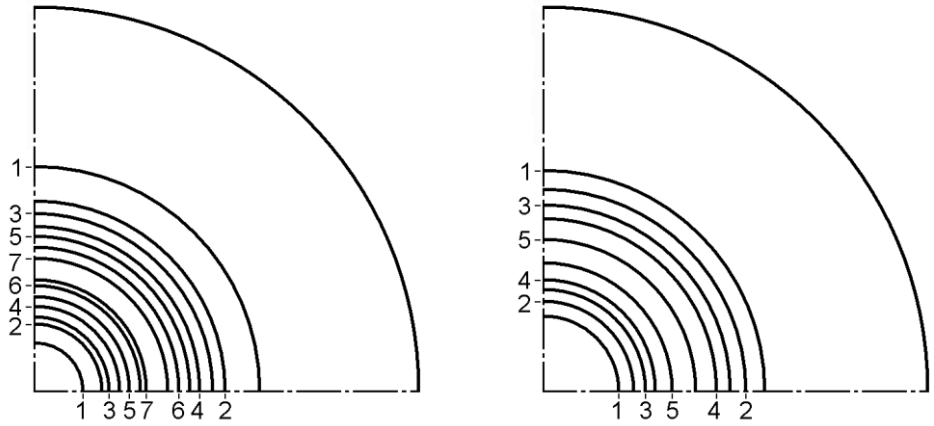

(a) (b)

Fig. 2 Direct pole figures (111) (a) and (10.1) (b) of cobalt electrodeposited at a temperature of 25 °C and current density of 2.5 A/dm^2: 1-7 - isointensity levels for diffracted X-rays

The results obtained from a qualitative assessment of the preferred grain orientations in various modifications of electrodeposited cobalt are consistent with the data in [19, 20], where the axial texture with [110] and [11.0] axes is reported as characteristic of electrodeposited cobalt.

A quantitative assessment of the degree of texture perfection in various modifications of electrodeposited cobalt showed that with an increase in deposition rate (corresponding to a 5fold increase in the current density: from 0.5 to 2.5 A/dm^2), the average scattering angle of the axial grain orientation in β-Co with the [110] axis decreases significantly (from 12.9 to 10.9 degrees) (**Table 1**), which indicates a more ordered crystallographic orientation of the grains in the [110] direction. A further fourfold increase in the current density (from 2.5 to 10.0 A/dm^2) is also accompanied by the improvement of the β-Co texture, but to a lesser degree. On the whole, it can be stated that slowing down the process of polymorphic transformation during the electrochemical phase formation of cobalt leads to intense texturing of its metastable β-modification.

Table 1 Effect of current density on the average scattering angle of axial orientations [110] for β-modification and [11.0] for α-modification of electrodeposited cobalt

Current density [A/dm^2]	**The average scattering angle of the texture [degrees]**	
	[110]	**[11.0]**
0.5	12.9	9.5
2.5	10.9	10.9
10.0	10.7	13.1

A different nature of the change in the degree of texture perfection with an increase in current density is exhibited by the stable α-modification of the electrodeposited cobalt (**Table 1**). Here, over the entire studied range of current density, the degree of perfection of the axial orientation with the [11.0] axis of the α-Co phase grains gradually decreases with increasing the deposition rate of the coatings.

The coatings obtained at a current density of 0.5 A/dm^2 featured intense axial orientation [11.0] of the α-Co phase grains with an average scattering angle of 9.5 degrees, while the formation of

DOI 10.12776/ams.v25i4.1357 p-ISSN 1335-1532
e-ISSN 1338-1156

the same phase at a current density of 10.0 A/dm^2 was accompanied by a more significant scattering of texture: the average scattering angle of the axial orientation with the [11.0] axis increased 1.4 times (to 13.1 degrees). Therefore, it can be concluded that slowing down the process of polymorphic transformation during the electrochemical phase formation of cobalt leads to hindering the oriented grain growth in its stable α-modification.

7 Discussion

The observed change in the degree of texture perfection exhibited by various modifications of cobalt being electrodeposited under slowing down the polymorphic β-Co → α-Co transformation can be explained as follows. Since polymorphic cobalt, in a process of its electrochemical phase formation from a liquid state, goes through a metastable β-Co phase state and crystallizes in the form of a stable α-Co modification, slowing down the phase transformation of the metastable modification into a stable one will result in a dual-phase state of the cobalt deposit on the cathode. Slowing down the β-Co → α-Co phase transformation caused by an increase in the amount of the metastable β-Co phase due to an increase in its formation rate, leads to the texturing of the resulting β-phase. The preferred orientation of the crystal lattices of the grains of the forming β-phase in the [110] crystallographic direction is primarily due to the tendency of the emerging system of randomly oriented lattices to reduce its internal energy. Therefore, with the slowing down of the process of polymorphic transformation during the electrochemical phase formation of cobalt, an intense texturing of its metastable β-modification occurs.

Since the β-Co → α-Co phase transformation occurs through a shear mechanism, an excessive amount of the β-phase, continuously forming during electrochemical crystallization, inhibits the phase transition of the metastable β-phase into a stable α-phase. This contributes to slowing down the process of polymorphic transformation, which leads to the formation of a more scattered axial texture with the [11.0] axis in the stable α-modification of electrodeposited cobalt.

The above features of texture formation during electrochemical crystallization of polymorphic cobalt were observed experimentally. Indeed, under slowing down the β-Co → α-Co phase transition proportionally to an increase in the current density, the preferred orientation of crystal lattices of the cobalt β-phase occurs in the [110] close-packed direction perpendicular to the coating surface (**Table 1**). At the same time, a disordering of the crystal lattices of the cobalt α-phase is observed in the [11.0] close-packed direction perpendicular to the coating surface (**Table 1**).

The findings are in conflict with the existing concepts about the electrochemical phase formation in metals and alloys [7-15]. Indeed, it is not possible to explain the observed effect of formation of a metastable β-modification of cobalt during room temperature electrodeposition, while it is known to exist in the temperature range from 700 to 1768 K; or emergence of a two-phase β-Co + α-Co structure by "incorporating" the ions from the aqueous solution or forming atoms into the crystal lattice of the cobalt being electrodeposited.

8 Additional Verification Experiments

If the proposed explanation of the above features of the texture formation in various modifications of electrodeposited cobalt is valid, then the addition into the electrolyte of substances, leading to the disordering of the crystal lattices of the forming grains of various modifications, should be accompanied by the formation of a more scattered texture. At the same time, the revealed features of the texture formation in various modifications of cobalt should generally be maintained.

DOI 10.12776/ams.v25i4.1357 p-ISSN 1335-1532
e-ISSN 1338-1156

To verify the assumption experimentally, the texture of cobalt electrodeposited from the electrolyte of the initial composition with an addition of carbon particles (fraction < 100 nm) at a concentration of 1.0 g/l was studied. Since carbon nanoparticles entering into the forming clusters of the liquid phase of electrodeposited cobalt can be considered as modifiers, one should expect the formation of not only a more scattered texture, but also a more fine-grained structure of the deposits.

The results of texture analysis (**Table 2**) of cobalt, electrodeposited in the presence of nanocarbon particles, clearly demonstrate a compliance with the identified texture features of the interrelated formation of cobalt modifications. Thus, while the degree of texturing of the stable α-modification of electrodeposited cobalt gradually decreases with an increase in the rate of its formation (**Table 2**), the perfection of the texture of the metastable β-modification increases rapidly (**Table 2**). At the same time, as follows from a comparative analysis of the data in **Table 1** and **Table 2**, the obtaining of the coatings from an electrolyte with an addition of nanocarbon particles leads to a significant scattering of the crystallographic texture for both metastable and stable cobalt modifications.

Table 2 Effect of current density on the average scattering angle of axial orientations [110] for β-modification and [11.0] for α-modification of cobalt electrodeposited in the presence of carbon nanoparticles

Current density [A/dm^2]	**The average scattering angle of the texture [degrees]**	
	[110]	**[11.0]**
0.5	15.8	11.2
2.5	12.4	12.7
10.0	11.9	13.8

A comparison of the surface morphology of the cobalt deposits obtained from electrolytes of different compositions (**Fig. 3**) indicates the finer grain aggregates of cobalt electrodeposited in the presence of carbon nanoparticles.

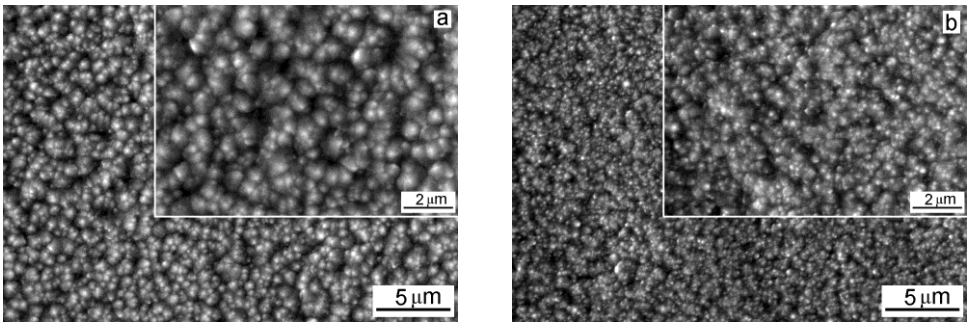

Fig. 3 SEM images of cobalt deposits obtained at a temperature of 25 °C and a current density of 2.5 A/dm^2 from an electrolyte without additives (a) and with the addition of carbon nanoparticles at a concentration of 1 g/l (b)

The above results confirm the validity of explaining the observed effects based on the concept of electrochemical phase formation in metals and alloys through a supercooled liquid state stage.

Hence, another proof of the existence of the phenomenon of electrochemical phase formation in metals and alloys through a supercooled liquid state stage is an intensive formation of the

DOI 10.12776/ams.v25i4.1357 p-ISSN 1335-1532
e-ISSN 1338-1156

metastable modification texture and simultaneous hindering of the development of the stable modification texture under the conditions of slowing down the polymorphic transformation in the metal being electrodeposited.

9 Conclusions

1. A hypothesis has been put forward to consider the crystallization of a polymorphic metal, being electrodeposited from the supercooled liquid state, as its sequential going through metastable modifications and the formation of a modification that is stable under the given deposition conditions as the last stage of phase formation.
2. An idea has been proposed, according to which the slowing down of the process of polymorphic transformation in a metal being electrodeposited should be accompanied by an intensive formation of the texture of the metastable modification and suppression of the texture development of the stable modification.
3. The results of the texture analysis of electrodeposited cobalt as a model metal showed that under slowing down the polymorphic transformation process in a metal being electrodeposited, the texture formation is intensified in the metastable modification, but suppressed in the stable modification. The finding is another proof of the existence of the phenomenon of electrochemical phase formation in metals and alloys through a supercooled liquid state stage.

References

[1] O. B. Girin: Phenomenon of Precipitation of Metal Being Electrodeposited, Occurring via Formation of an Undercooled Liquid Metal Phase and its Subsequent Solidification. Part 1. Experimental Detection and Theoretical Grounding. In: Materials Development and Processing, edited by J.V. Wood, L. Schultz, D.M. Herlach, WILEY-VCH Verlag Gmbh, Weinheim, Vol. 8, 2000, p. 183-188, http://dx.doi.org/10.1002/3527607277.ch30
[2] O. B. Girin: Phenomenon of Precipitation of Metal Being Electrodeposited, Occurring via Formation of an Undercooled Liquid Metal Phase and its Subsequent Solidification. Part 2. Experimental Verification. In: Materials Development and Processing, edited by J.V. Wood, L. Schultz, D.M. Herlach, WILEY-VCH Verlag Gmbh, Weinheim, Vol. 8, 2000, p. 189-194, http://dx.doi.org/10.1002/3527607277.ch31
[3] O. B. Girin: Journal of Chemical Technology and Metallurgy, Vol. 54, 2019, No. 2, p. 391-396
[4] O. B. Girin: Surface Engineering and Applied Electrochemistry, Vol. 53, 2017, No. 2, p. 137-143, http://dx.doi.org/10.3103/S1068375517020041
[5] O. B. Girin: Surface Engineering and Applied Electrochemistry, Vol. 53, 2017, No. 3, p. 233-239, http://dx.doi.org/10.3103/S1068375517030048
[6] O. B. Girin: Surface Engineering and Applied Electrochemistry, Vol. 53, 2017, No. 4, p. 339-344, http://dx.doi.org/10.3103/S1068375517040056
[7] A. Milchev: Electrocrystallization. Fundamentals of nucleation and growth, Springer US, New York, 2002, http://dx.doi.org/10.1007/b113784
[8] M. Paunovic M., M. Schlesinger: Fundamentals of electrochemical deposition, second ed., WILEY-INTERSCIENCE, Hoboken, 2006, http://dx.doi.org/10.1002/aic.11636
[9] E. B. Budevski, G. T. Staikov, W. J. Lorenz: Electrochemical phase formation and growth: an introduction to the initial stages of metal deposition, WILEY-VCH, Weinheim, 2008, http://dx.doi.org/10.1002/9783527614936

DOI 10.12776/ams.v25i4.1357 p-ISSN 1335-1532
e-ISSN 1338-1156

[10] W. Plieth: Electrochemistry for materials science, Elsevier B. V., Amsterdam, 2008, http://dx.doi.org/10.1016/B978-0-444-52792-9.X5001-5
[11] Yu. D. Gamburg, G. Zangari: Theory and practice of metal electrodeposition, Springer Science, New York, 2011, http://dx.doi.org/10.1007/978-1-4419-9669-5
[12] A. Milchev: ChemTexts, Vol. 2, 2016, No. 4, p. 1-9, http://dx.doi.org/10.1007/s40828-015-0021-1
[13] G. Staikov: Nanoscale, Vol. 8, 2016, No. 29, p. 13880-13892, http://dx.doi.org/10.1039/C6NR01547F
[14] T. Mehmood et al.: International Journal of Electrochemical Science, Vol. 12, 2017, p. 1203-1215, http://dx.doi.org/10.20964/2017.02.45
[15] S. R. Brankovic: Electrochemical Society Interface, Vol. 27, 2018, No. 2, p. 57–63, http://dx.doi.org/10.1149/2.F05182if
[16] D. A. Porter, K. E. Easterling, M. Y. Sherif: Phase transformations in metals and alloys, third ed., CRC Press, Boca Raton, 2009, http://dx.doi.org/10.1201/9781439883570
[17] M. J. Q. Hernandez, J. A. Pero-Sanz, L. F. Verdeja: Solidification and solid-state transformations of metals and alloys, first ed., Elsevier B. V., Amsterdam, 2017
[18] L. Mentar et al.: Transactions of the IMF, Vol. 89, 2011, No. 3, p. 143-150, http://dx.doi.org/10.1179/174591911X13013911711888
[19] S. Armyanov: Electrochimica Acta, Vol. 45, 2000, No. 20, p. 3323-3335, http://dx.doi.org/10.1016/S0013-4686(00)00408-4
[20] A. Vicenzo, P. L. Cavallotti: Electrochimica Acta, Vol. 49, 2004, No. 24, p. 4079-4089, http://dx.doi.org/10.1016/j.electacta.2004.04.001

DOI 10.12776/ams.v25i4.1357 p-ISSN 1335-1532
e-ISSN 1338-1156

EFFECTS OF BIAS VOLTAGE ON ADHESION AND PROPERTIES OF CHROMIUM NITRIDE THIN FILMS

Trung Van Trinh[1)], Tuan Hong Pham[2)], Hop Thanh Nguyen[2)], Thanh Van Nguyen[1,3)]*
[1)]Hanoi University of Science and Technology, Ha Noi, Viet Nam
[2)]National Center for Technological Progress, Ha Noi, Viet Nam
[3)]Research Institute of Technology for Machinery, Ha Noi, Viet Nam

Received: 21.05.2019
Accepted: 02.12.2019

[*]Corresponding author: e-mail: trung.trinhvan@hust.edu.vn, Tel.: +84 24 3868 0409, School of Materials Science and Engineering, Hanoi University of Science and Technology, No.1 Dai Co Viet, Hai Ba Trung, Hanoi, Vietnam

Abstract
Thin films were deposited on SUS440 stainless steel samples by arc plasma evaporation at bias voltage range from -10 to -100 V. X-ray diffraction, optical microscopy, field emission scanning electron microscopy, energy dispersive spectroscopy, microhardness test, and electrochemical test were used to investigate the morphology and properties of the thin films. Particularly, the thin films were composed of chromium nitride (CrN, phases of CrN + Cr) and 0.76 μm thick. They were deposited with microdroplets on the samples. The surface hardness of these films reached the highest value of 1492 HV at the bias of -20 V. As the bias voltage increased, the adhesion of the CrN thin films decreased. The excessively high bias voltage of -100 V led to the delamination of the CrN thin films. The electrochemical test demonstrated that the corrosion resistance in the 3% NaCl solution of CrN coating can be improved.

Keywords: CrN, adhesion, bias voltage, SUS440, hard coating, corrosion resistant

1 Introduction

Chromium nitride (CrN) is a bright silver-grey-colored coating that has a high hardness [1] and a good resistance to oxidation and corrosion [2, 3]. It is widely used as an alternative for coating material to TiN in applications involving cutting, forming, and die casting of aluminum and zinc. Many techniques have been used to deposit CrN coatings, such as magnetron sputtering [4, 5], pulsed laser deposition [6], arc plasma evaporation [6 - 8], and ion assisted deposition [9 -11]. Among these techniques, arc plasma evaporation is the most popular in the industry due to its high deposition rate. The properties of coatings by this method strongly depend on the technological parameters of deposition, such as bias voltage, nitrogen pressure, substrate temperature, and arc current. Bias voltage and gas pressure are the key parameters that control deposition [11]. Meanwhile, pressure affects the chemical composition, phase structure, preferred orientation, and deposition rate of coatings. Chang deposited CrN coatings by arc ion plating. He reported that the microhardness of the CrN coatings by arc ion plating method increased from 1550 HK_{50g} to 2100 HK_{50g} (2638 HV to as nitrogen pressure increased from 0.4 Pa to 1.2 Pa primarily due to the variation in composition and structure [12]. The bias voltage can influence the nucleation and growth kinetics during coating growth and subsequently modify the microstructure and properties of coatings. Wang and Oki investigated how substrate bias voltage influences the orientation, morphology, and microhardness of reactive ion-plated CrN films using an ion plating. They

DOI 10.12776/ams.v25i4.1356 p-ISSN 1335-1532
e-ISSN 1338-1156

reported a decrease in the microhardness of the films deposited at high bias voltages caused by a change in the microstructure from a dense columnar structure to a columnar structure with voided grain boundaries [13]. The adhesion and properties of coatings also strongly depend on the deposition method. Hence, the effects of bias voltages in arc plasma evaporation on the adhesion and properties of CrN are still further investigated.

In this study, CrN thin films were deposited on the SUS440 substrate under various bias voltages using an arc plasma evaporation system to improve the surface hardness and corrosion resistance of the SUS440 steel that can be applied for molds made of this steel. The effects of the bias voltages on the properties of the CrN thin films, such as surface morphology, adhesion, and surface hardness, were studied. The corrosion resistance of the CrN coatings was also investigated.

2 Experimental procedures

A SUS440 stainless steel bar with a composition of Fe-0.95C-17.20Cr-1.00Mn-1.00Si in wt.% was cut into small samples with 18 mm diameter and 6 mm thickness. Then, it was austenitized at 1030 °C for 60 min, quenched by oil, and tempered at 160 °C for 3 h. After tempering, the hardness of the samples was 677 HV (≅ 59 HRC), which is the normal hardness value for molds.

Prior to deposition, the SUS440 samples were ground by 1000 grit abrasive papers, polished, ultrasonically cleaned with acetone and alcohol, and then dried.

The SUS440 samples were mounted on a sample holder in the middle of the chamber of the arc plasma evaporation system (Dreva-400, Germany) to form the CrN thin films. A Cr target with a purity of 99.99% was used as the source for evaporation. The average distance between the Cr target and the SUS440 sample was 200 mm. The temperature inside the chamber was increased to 300 °C by two lateral heaters. The working chamber was vacuumed to a pressure of 2.0×10^{-2} Pa. Then, Ar gas was introduced into the chamber at a flow rate of 60 sccm. The surfaces of the SUS440 samples were sputter-cleaned in a hollow cathode mode with a current of 120 A and a substrate bias of -200 V for 15 min. The flow rate of the Ar gas was reduced to 10 sccm. Then, N_2 gas was introduced at a flow rate of 600 sccm as the reactive gas. The target current was maintained at 120 A to deposit CrN thin films on the SUS440 samples. Deposition duration was set to 15 min. The bias voltages were varied as -10, -20, -30, -50, and -100 V.

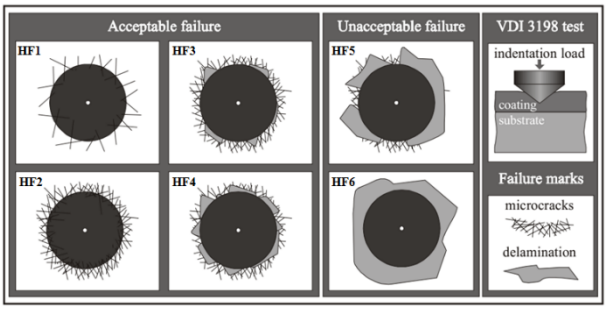

Fig. 1 Principle of the VDI 3198 indentation test [14]

The surface morphology of the CrN thin films was examined by field emission scanning electron microscopy (FESEM, JSM-7600F, JEOL) and optical microscopy (AxioVert 25A). The phase composition of these films were determined by X-ray diffraction with Cu-Kα (X'Pert PRO,

DOI 10.12776/ams.v25i4.1356 p-ISSN 1335-1532
e-ISSN 1338-1156

PANalytical). The Cu-K_α line at 0.15405 nm was used as the source for diffraction pattern analyses. Hardness testing was performed on a Vickers microindenter (Duramin 2, Struers) under a load of 10 g for 15 s. The adhesion of the coatings to the substrates was studied in accordance with VDI 3198 standard procedures using Rockwell-C indenters with a load of 150 kg; the adhesion was compared with adhesion strength quality maps via optical microscopy. The principle of this quality test is presented in **Fig. 1**. A conical diamond indenter penetrated the coated surface to induce massive plastic deformation to the coated film on the substrate and extreme shear stresses at the interface, thereby fracturing the coating. Good adhesion coatings will withstand these shear stresses and prevent extended delamination circumferentially. The four different textures from HF1 to HF4 illustrate the indentation shapes that guarantee strong adhesion of the coating on the substrate (HF is the German short form of adhesion strength.). However, the delamination (HF5 and HF6) at the vicinity of the indentation depicts poor interfacial adhesion [14]. The electrochemical measurements were performed in a standard three-electrode cell with 1 cm^2 platinum counter electrode and a saturated calomel electrode as the reference electrode. The electrolyte was a 3.5% NaCl solution. After each potentiodynamic polarization test, the corrosion potential (E_{corr}) and the corrosion current density (I_{corr}) can be determined by a Tafel plot.

3 Results and discussion

Fig. 2 shows the analytical results of a deposited CrN thin film with at -20 V bias on one SUS440 sample. A featureless surface morphology of this film examined by SEM is shown in **Fig. 2a** with microdroplets. These microdroplets seem to be Cr particles that cannot be ionized totally from the target. The Cr phase is attributed to incorporated microdroplets, which have previously been reported to have a core consisting of pure metal phase [15, 16]. **Fig. 2b** presents a cross-sectional SEM image of the CrN thin films. These films are dense and compact. According to the SEM measurements, the thickness of these films is approximately 0.76 μm. **Fig. 2c** shows the diffraction patterns of the CrN thin films deposited on the SUS440 samples. The peaks at $2\theta = 37.4^o$ and 43.6^o correspond to CrN phase (ICSD card #11-0065). A CrN thin film is formed after deposition on the SUS440 substrate. The peaks at $2\theta = 44.6^o$, 50.5^o, and 64.6^o correspond to the SUS440 substrate. The diffraction peaks of Cr at $2\theta = 44.4^o$ and 64.6^o overlap with those of the substrate. This result is confirmed by the too high concentration (98.8 wt. %) of Cr as depicted in **Fig. 2d** than that by stoichiometry in CrN phase (~78.8 wt. %). Besides that EDS would not detect the Cr in the substrate cause of other elements such as Fe with an even higher concentration in the substrate also could not be detected. Therefore, the Cr target is not completely transformed to CrN during the film formation. Hence, the film consists of CrN + Cr phases.

Fig. 3 shows the effects of bias voltages on the surface hardness of the CrN thin films deposited on the SUS440 samples. The surface hardness of these films increases initially and then decreases as the bias voltage increases. The highest hardness of approximately 1492 HV is observed at the bias voltage of -20 V. High negative bias voltages generally increase the energy of incident particles. Hence, a high value of surface hardness of the CrN films is archived in this study. As the bias voltage increases, the bombardment energy of the incident particles on the substrate increases also, thereby causing internal stress and increasing surface hardness. However, the hardness decreases rapidly when the bias voltage exceeds -20 V probably due to the lattice relaxation and recrystallization of the superfluous bombarding energies [11] and/or defects, damage the film.

DOI 10.12776/ams.v25i4.1356 p-ISSN 1335-1532
e-ISSN 1338-1156

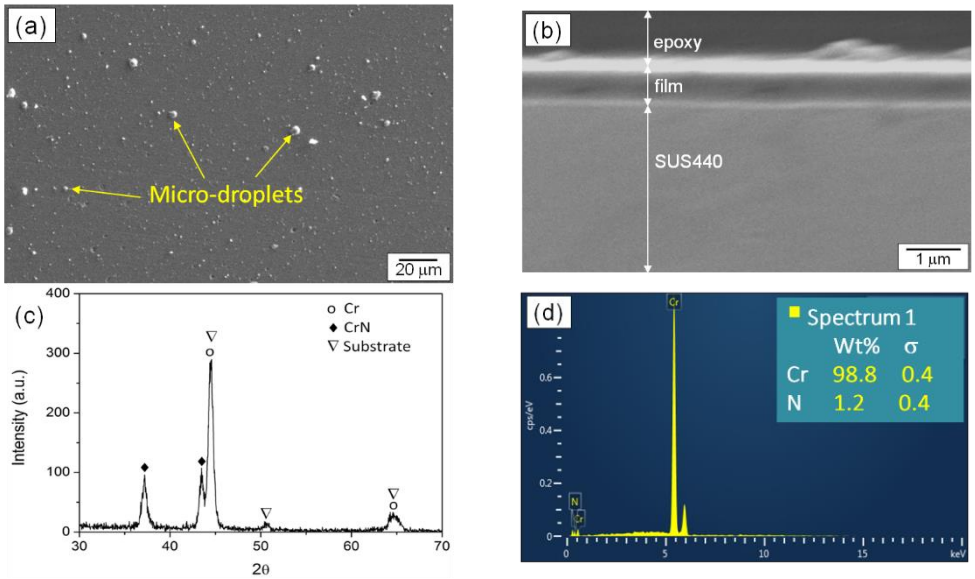

Fig. 2 CrN thin films deposited on the SUS440 samples at the bias of -20 V. (a) Top-view SEM image, (b) cross-sectional SEM image, (c) XRD pattern, and (d) EDS of the surface

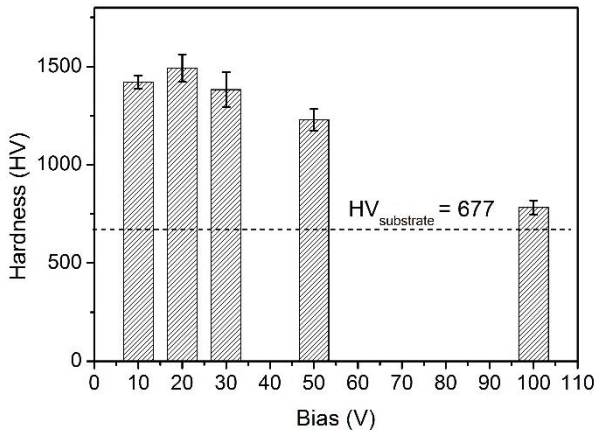

Fig. 3 Effects of the bias voltages on the surface hardness of the CrN thin films deposited on the SUS440 samples

Fig. 4 shows the optical images of the CrN thin films (as-deposited and after the Rockwell-C test) at different bias voltages. These films were deposited with many microdroplets. At the bias voltage of -100 V, the CrN film is delaminated (Fig. 4d). For all coated samples in this study, extended delamination at the vicinity of the imprint indicates poor interfacial adhesion (HF6). Further study, such as those with an increase in deposition time and new substrate materials, should be conducted to investigate the adhesion of the deposited CrN thin films. According to the results of the current study, at high bias voltages, delamination occurs severely, thereby further reducing the adhesion of the CrN thin films. This behavior can be attributed to an excessive intensity of residual stress, which can damage coatings and/or create adhesion failure [17].

DOI 10.12776/ams.v25i4.1356
p-ISSN 1335-1532
e-ISSN 1338-1156

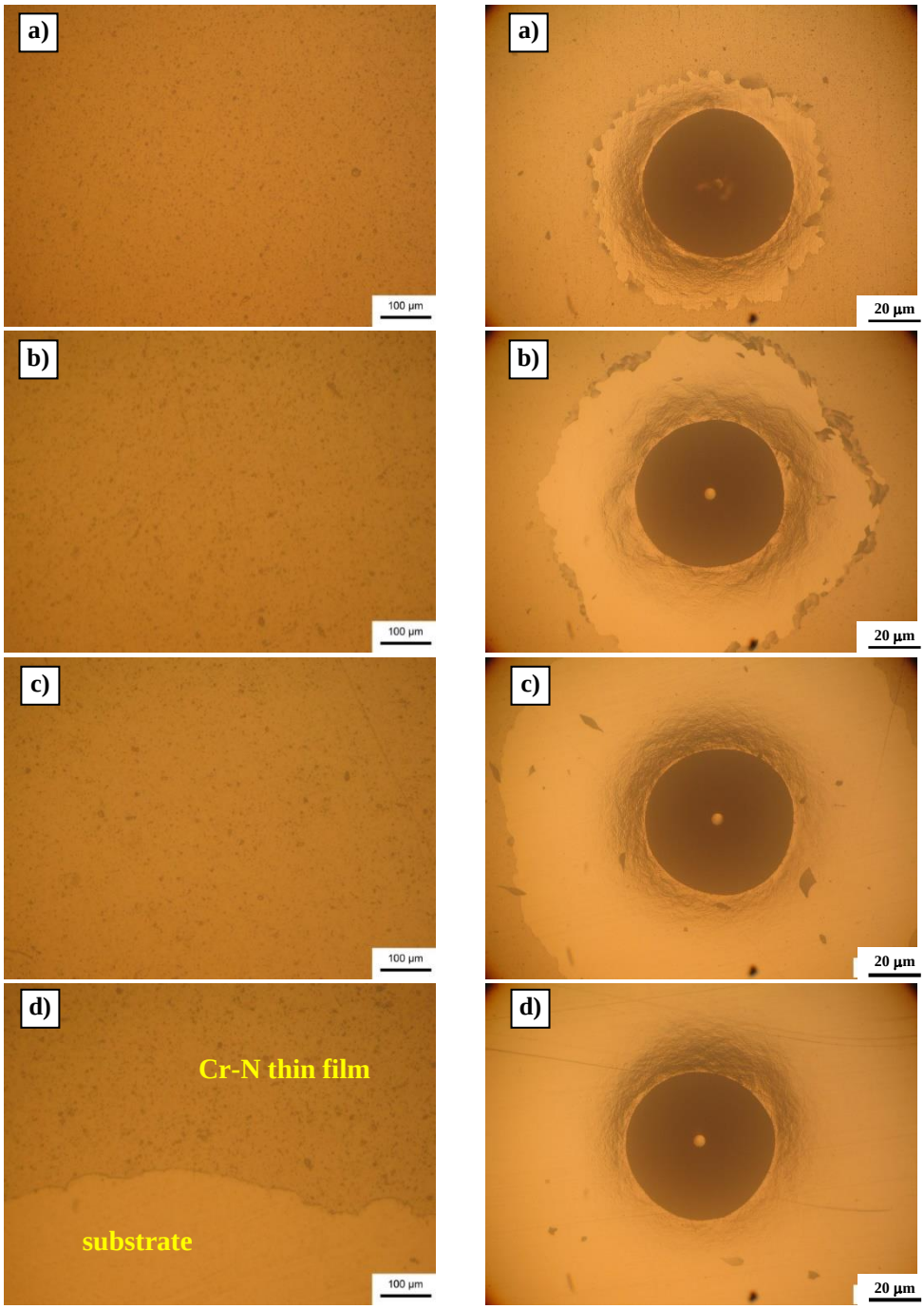

Fig. 4 Top-view optical images (before [left] and after the Rockwell-C indentations [right]) of the CrN thin films deposited on the SUS440 samples at the bias voltages of (a) -20 V, (b) -30 V, (c) -50 V, and (d) -100 V

DOI 10.12776/ams.v25i4.1356 p-ISSN 1335-1532
e-ISSN 1338-1156

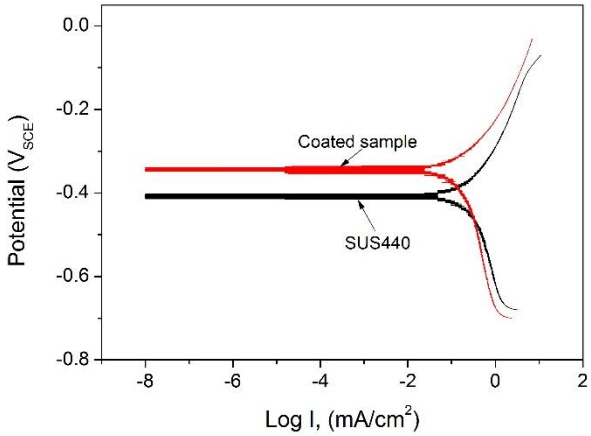

Fig. 5 Polarization curves of coated and uncoated samples in 3.5 wt.% NaCl aqueous solution

Fig. 5 shows the anodic polarization curves in 3.5 wt.% NaCl aqueous solution for the uncoated and CrN-coated samples at the bias voltage of -20 V. The corrosion potential and corrosion current density are −0.34 V and 0.119 mA/cm^2, respectively, for the coated sample and −0.42 V and 0.316 mA/cm^2, respectively, for the uncoated sample. The coated sample has a more positive corrosion potential value than the uncoated sample. On this basis, the coating shifts the corrosion potential to higher positive $E_{corr.}$ values. Therefore, a stable electrode potential is achieved, and the corrosion resistance of the coated sample is improved. $I_{corr.}$ is commonly utilized as an index for evaluating corrosion resistance. In this study, the $I_{corr.}$ is significantly reduced after CrN deposition. Thus, the corrosion resistance of the coated sample has an evident enhancement compared with that of the uncoated sample.

4 Conclusions

CrN thin films with a thickness of 0.76 μm were deposited on SUS440 stainless steel samples by arc plasma evaporation. The hardness of these films increased initially and then decreased as the bias voltage increased. The highest hardness of approximately 1492 HV was observed at the bias voltage of -20 V. These films consisted of CrN + Cr phases with many microdroplets and poor interfacial adhesion. They were delaminated when deposited at the bias voltage of -100 V. Compared with the corrosion resistance of the uncoated sample, that of the coated sampled was enhanced.

References

[1] S. K. Tien, J. G. Duh: Thin Solid Films, Vol. 494, 2006, No. 1-2, p. 173-178, http://dx.doi.org/10.1016/j.tsf.2005.08.198
[2] P. H. Mayrhofer, G. Tischler, C. Mitterer: Surface & Coatings Technology, Vol. 142-144, 2001, p. 78-84, http://dx.doi.org/10.1016/S0257-8972(01)01090-8
[3] C. He´au, R. Y. Fillit, F. Vaux, F. Pascaretti: Surface & Coatings Technology, Vol. 120-121, 1999, p. 200-205, http://dx.doi.org/10.1016/S0042-207X(02)00146-X
[4] S. Y. Lee, B. S. Kim, S. D. Kim, G. S. Kim, Y. S. Hong: Thin Solid Films, Vol. 506-507, 2006, p. 192-196, http://dx.doi.org/10.1016/j.tsf.2005.08.027

DOI 10.12776/ams.v25i4.1356 p-ISSN 1335-1532
e-ISSN 1338-1156

[5] Y. P. Purandare, A. P. Ehiasarian, Eh. P. Hovsepian: Journal of Vacuum Science & Technology A, Vol. 26, 2008, No. 2, p. 288-296, http://dx.doi.org/10.1116/1.2839855
[6] T. Suzuki, H. Saito, M. Hirai, H. Suematsu, W. Jiang, K. Yatsui: Thin Solid Films, Vol. 407, 2002, No. 1-2, p. 118-121, http://dx.doi.org/10.1016/S0040-6090(02)00023-8
[7] M. Zhang, M. K. Li, K. H. Kim, F. Pan: Applied Surface Science, Vol. 255, 2009, No. 22, p. 9200-9205, http://dx.doi.org/10.1016/j.apsusc.2009.07.002
[8] M. Holzherr, M. Falz, T. Schmidt: Surface & Coatings Technology, Vol. 203, 2008, No. 5-7, p. 505-509, http://dx.doi.org/10.1016/j.surfcoat.2008.05.054
[9] V. M. Vishnyakov et al.: Thin Solid Films, Vol. 497, 2006, No. 1-2, p. 189-195, http://dx.doi.org/10.1016/j.tsf.2005.05.005
[10] T. Bin, Z. Xiaodong, H. Naisai, H. Jiawen: Surface & Coatings Technology, Vol. 131, 2000, No. 1-3, p. 391-394, http://dx.doi.org/10.1016/S0257-8972(00)00769-6
[11] X. S. Wan, S. S. Zhao, Y. Yang, J. Gong, C. Sun: Surface & Coatings Technology, Vol. 204, 2010, No. 11, p. 1800-1810, http://dx.doi.org/10.1016/j.surfcoat.2009.11.021
[12] Z. K. Chang, X. S. Wan, Z. L. Pei, J. Gong, C. Sun: Surface & Coatings Technology, Vol. 205, 2011, No. 19, p. 4690-4696, http://dx.doi.org/10.1016/j.surfcoat.2011.04.037
[13] D. Wang, T. Oki: Thin Solid Films, Vol. 185, 1990, No. 2, p. 219-230, http://dx.doi.org/10.1016/0040-6090(90)90086-S
[14] N. Vidakis, A. Antoniadis, N. Bilalis: Journal of Materials Processing Technology, Vol. 143-144, 2003, p. 481-485, http://dx.doi.org/10.1016/S0924-0136(03)00300-5
[15] H. Ljungcrantz, L. Hultman, J. E. Sundgren, G. Hakansson, L. Karlsson: Surface & Coatings Technology, Vol. 63, 1994, p. 123-128, http://dx.doi.org/10.1016/S0257-8972(05)80016-7
[16] C. Rebholz, H. Ziegele, A. Leyland, A. Matthews: Surface & Coatings Technology, Vol. 115, 1999, No. 2-3, p. 222-229, http://dx.doi.org/10.1016/S0257-8972(99)00240-6
[17] R. O. E. Vijgen, J. H. Dautzenberg: Thin Solid Films, Vol. 270, 1995, No. 1-2, p. 264-269, http://dx.doi.org/10.1016/0040-6090(95)06984-4

Acknowledgements

This research is supported by the Hanoi University of Science and Technology (HUST), under project number T2018-PC-088.

INFLUENCE OF CRYOROLLING ON PROPERTIES OF L-PBF 316L STAINLESS STEEL TESTED AT 298K AND 77K

Patrik Petrousek [1)], Tibor Kvackaj [1)], Robert Kocisko [1)], Jana Bidulska [1)], Miloslav Luptak [1)], Diego Manfredi [2)], Marco Actis Grande [2)], Robert Bidulsky [3)]*
[1)] Technical University of Kosice, Faculty of Metallurgy, Materials and Recycling, Dpt. of Plastic Deformation and Process Simulation, Letna 9, 040 01, Slovakia
[2)] Politecnico di Torino, Department of Applied Science and Technology, Corso Duca degli Abruzzi, 24 10129 Torino, Italy
[3)] Authorised representative for innovation and technological transfer, Košice Self-Governing Region, Namestie Maratonu mieru 1, 042 66 Kosice, Slovakia

Received: 08.11.2019
Accepted: 10.12.2019

[*]Corresponding author: e-mail: robert.bidulsky@arr.sk, Tel.:+421 055 68 228 22, Presidents plenipotentiary for innovation and technological transfer, Košice Self-Governing Region, Namestie Maratonu mieru 1, 042 66 Kosice, Slovakia

Abstract
The goal of the present work is to evaluate mechanical properties and to analyse the microstructure of 316L stainless steel produced by Laser Powder Bed Fusion (L-PBF) follow by rolling with different thickness reduction under ambient and cryogenic conditions. The samples before rolling were heat treated. The static tensile test was realized at ambient and cryogenic (77K) conditions. The L-PBF powder metal production technology approved that is a key technology in the additive manufacturing (AM) area, especially for metal powder materials. Mechanical properties tested at 298K and 77K shows that the application of various thermo-deformation rolling conditions increases of strength properties. Achieved mechanical properties are comparable to conventional bulk materials. The strength properties after the rolling under ambient and cryogenic conditions were significantly increased.

Keywords: stainless steel, laser powder bed fusion, cryogenic conditions, mechanical properties, cryorolling

1 Introduction

Additive manufacturing (AM) is a technology that has wide possibilities for producing materials and products of common as well as extraordinary properties through powder metallurgy (PM). PM products are exceptional due to their features but also because their price is significantly lower than products produced by other technologies [1-6]. The biggest benefits are: possibility to produce components of very complicated shapes, use of extremely hard and solid materials, production of composite materials and last but not least, high material savings. AM technologies can achieve up to 90 – 95 % of material savings. With the help of progressive technologies, it is possible to recycle the used powder material and increase the percentage of its utilization up to 100 % [7-12].

Laser Powder Bed Fusion (L-PBF) technology is particularly important in PM. With a laser beam melt the powder particles in a precisely defined field and liquid phase can be achieved in a very

DOI 10.12776/ams.v25i4.1366 p-ISSN 1335-1532
e-ISSN 1338-1156

short time. During the interaction between the surface of the powder layer and the laser, the powder particles are rapidly melted [13-15]. This process will rapidly melt the powder particles and rapidly transfer to solid form without any direct addition of other material elements to modify the chemical composition [16-18]. Due to the relatively low penetration of the liquid phase to a depth (approximately 10 - 1000 μm), very high cooling rates of 10^3 to 10^6 $K.s^{-1}$ are achieved [19]. High internal thermal stresses created in the material because of the high cooling rates must be removed before further processing. [19-22].

Nowadays, it is possible to produce products using L-PBF technology with mechanical properties at the level of conventionally produced materials. Conventionally produced 316L stainless steel, which is intended for the energy sector, have yield strength values of 500 MPa [23, 24]. The steel grade 316L is successfully applicable for working under cryogenic conditions, for example as the construction parts at fusion reactor. For application at fusion reactor nowadays is requirement on the yield strength must reach value $R_{P0,2} \geq 1200$ MPa. [25-27].

The properties of 316L stainless steel can be influenced by thermo-mechanically controlled processing under cryogenic conditions, and thus strength properties exceeding $R_m \approx 1600$ MPa can be achieved [3]. With increasing dislocation density, dislocation movement and stress concentration are inhibited. This causes the plastic deformation mechanism to be triggered by mechanical twinning. With a further increase deformation, it can be assumed that grain refinement will occur until a grain size structure of the order of nanometres can be achieved. The mechanical properties of materials it is possible to increase by forming under cryogenic conditions [27-29].

In this paper are investigating the mechanical properties of samples from 316L PM stainless steel prepared by L-PBF and heat treatment which were subsequently rolled at ambient and cryogenic temperatures. The rolled samples were tested under ambient and cryogenic conditions.

2 Experimental material and methods

Commercially produced material EOS Stainless Steel 316L with chemical composition 18 % Cr, 14,5 % Ni, 2,5 % Mo, and 0,5 % Si was used in the study. The particles of 316L powder were analysed using a FESEM Zeiss Supra 40 microscope. The particles have mostly an ideal spherical shape with particle sizes in range <10; 60> [μm] and average particle size was 33 μm. Sieve analysis was performed following ASTM B 214-07.

The samples produced for the static tensile test were heat treated. The samples before rolling were annealed by solution annealing at 1050 ° C / 60 min, followed by artificial aging at 700 °C / 3000 min. The samples were marked as HT2.

L-PBF technology

The samples were made using L-PBF technology on an EOS M280 Dual Mode (EOS GmbH, Krailling / Munich, Germany). The EOS M280 is equipped with a 200W Yb fiber laser. The samples were produced in an argon atmosphere with a 20 μm layer thickness and a meander scanning strategy. Table 1 shows the bases of the manufacturing process parameters, where P is the laser power, S_s is the scanning speed, h_d is the hatching distance of individual laser paths, and S_1 is the length of the welding strip.

Table 1 Parameters optimized for the fabrication of dense samples in SS 316L through an EOS M280 machine

P [W]	S_s [mm.s^{-1}]	h_d [mm]	S_l [mm]
195	800	0,09	800

DOI 10.12776/ams.v25i4.1366 p-ISSN 1335-1532
e-ISSN 1338-1156

Static tensile test

The static tensile test at 298K and 77K was performed on the TINIUS OLSEN H300KU with Horizon software. Under both temperature conditions, the crosshead movement speed of 0.3 $mm.s^{-1}$ was chosen, which corresponds to a strain rate of 0.0023 s^{-1} following STN EN ISO 6892-2.

3 Results and discussion

Mechanical properties

The values of mechanical properties after rolling under different rolling conditions can be summarized in the **Fig. 1** and **Fig. 2.** In **Fig. 1** the mechanical properties of samples rolled under AT (ambient temperature) and CT (cryogenic temperature) follow by static tensile tests performed at ambient temperature T_{test} = 298K. For deformations ε = 71 % and 86 % were $R_{p0,2,AT} \in$ <1017; 1070> [MPa]; $R_{m,AT}$ <1165; 1300> [MPa] and $A_{t,AT}$ <5; 6> [%]. After CT rolling with ε = 40 %, strength properties were achieved at the level of specimens rolled at deformations of ε = 71 % and 86 %. The total elongation A_t value for samples rolled with deformations above 40 % was almost constant 5 - 6 %. When rolling in AT and CT at selected deformations higher than 40 %, the strength properties increased three-fold compared to the initial state. A significant increase in strength properties resulted in a significant decrease in A_t.

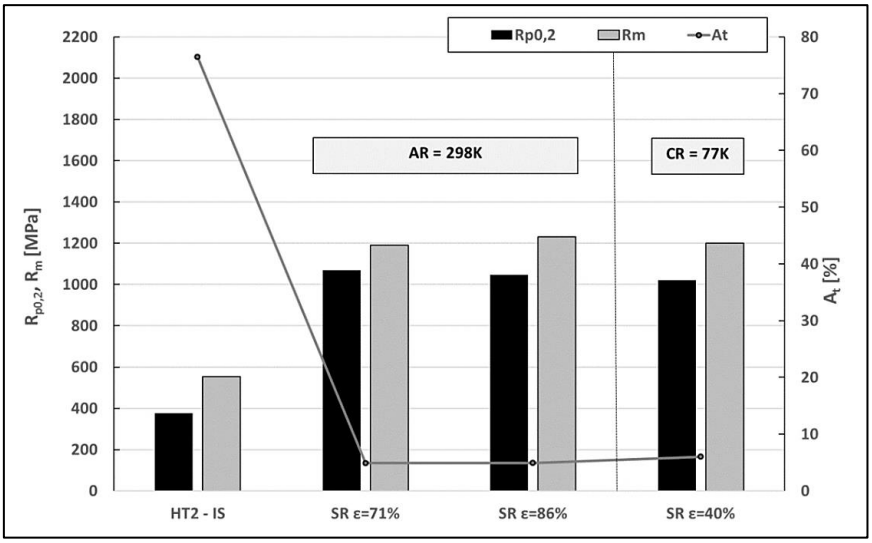

Fig. 1 Mechanical properties of the samples rolled under AT and CT conditions and tested by static tensile testing at 298K

The **Fig. 2** depicts that the static tensile test at T_{test} = 77K showed a further significant increase in strength properties. The increment $R_{p0.2}$ after symmetric rolling at CT (SR_{CT}) is almost the same as SR_{AT} at twice the deformation.

The measured values indicate that even at half deformation in CT conditions it is possible to achieve strength properties at the level of materials rolled under AT conditions. The value of A_t was approximately the same for the measured conditions after rolling and a small increase was observed after the static tensile test under conditions T_{test} = 77K.

DOI 10.12776/ams.v25i4.1366 p-ISSN 1335-1532
e-ISSN 1338-1156

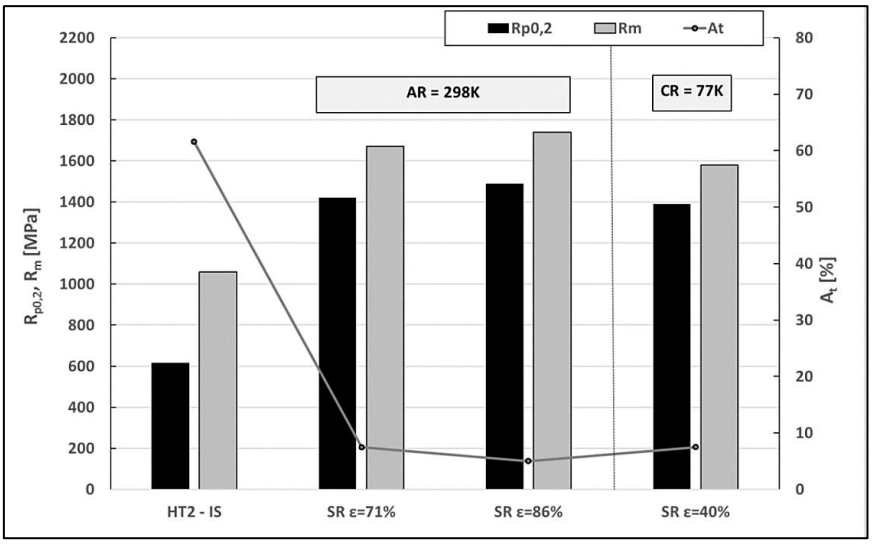

Fig. 2 Mechanical properties of the samples rolled under AT and CT conditions and tested by static tensile testing at 77K

Based on these results, it can be concluded that after the deformation conditions selected, the maximum possible mechanical properties have been achieved and further enhancement of the mechanical properties must be associated with the modification of the structure.

Based on the analysis of mechanical properties under various conditions of thermal and deformation treatment of the material, it is possible to compare the results with the values of recommended mechanical properties of the material 316L according to works [30-32] for fusion reactor. The initial state had about 30 % higher A_t values as compared to conventionally rolled material $A_t \leq 42$ % [31,32]. The initial state tested at $T_t = 77K$ retained a high A_t value with almost doubling the strength properties. After rolling of the HT2 state, a significant increase in $R_{p0.2}$ was achieved. A comparison of the mechanical properties of rolled bulk materials and materials produced by L-PBF technology shows that L-PBF technology can produce materials with properties close to the level of rolled materials.

Microstructure

The microstructure of **Fig. 3a** shows that after the chosen solution annealing and artificial aging, grains were recrystallized with the exclusion of oxide and carbide particles, which are mainly visible in SEM images (**Fig. 3b**). The average grain size after the solution annealing and artificial aging was 35 μm. On the microstructures is visible a quasi polyedric structure with different sized austenitic grains. At the grain boundaries, precipitation of oxidic and carbide particles can be observed. STEM EDS identified two types of precipitates in grains and two types of precipitates contouring the high grain boundaries. Large precipitates (> 200 nm) inside the grains and along the grain boundaries are of the $(Mn,Cr_2)O_4$ and MnO_2. Large precipitates lying along the grain boundaries are $Cr_{23}C_6$ carbides.

The **Fig. 4-6** show microstructures of samples rolled under various deformation conditions. It can be seen that with the deformations ε = 71 % and 86 %, the grains were significantly elongated into the rolling direction and significant slip strips were formed. Some grains in the rolling direction were elongated more than 500 μm. According to the authors [33, 34], $d_{\gamma,kor}$ was calculated for

DOI 10.12776/ams.v25i4.1366 p-ISSN 1335-1532
e-ISSN 1338-1156

individual deformation conditions. As the deformation increased, an overall reduction of $d_{\gamma, kor}$. Samples with ε = 71% and 86% had values $d_{\gamma, kor} \in \langle 20; 23 \rangle$ [μm].

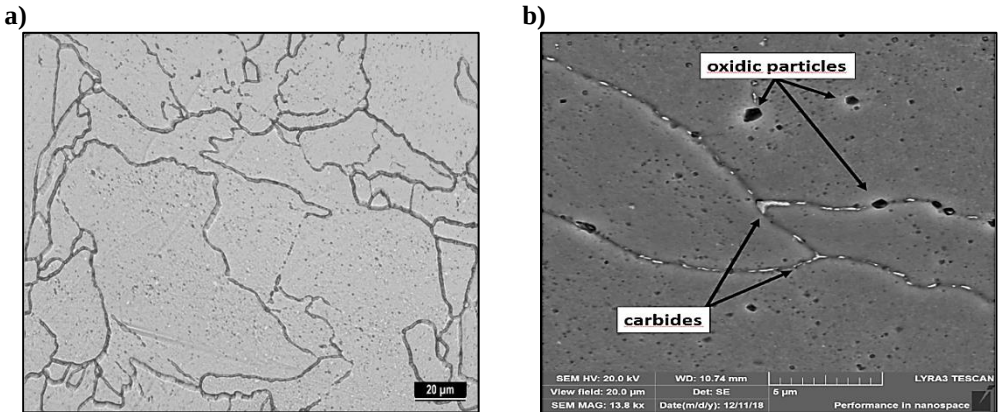

Fig. 3 a) Microstructure of initial state HT2 b) SEM microstructure of oxidic and carbidic precipitates

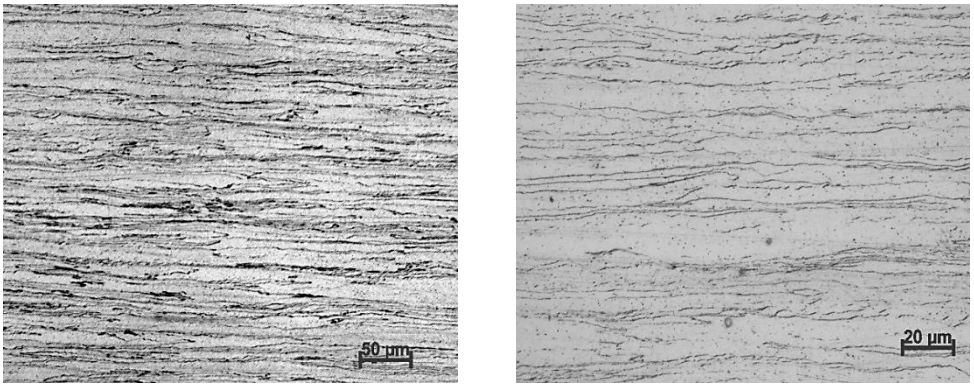

Fig. 4 Microstructure after rolling with ε = 86 % under ambient temperature

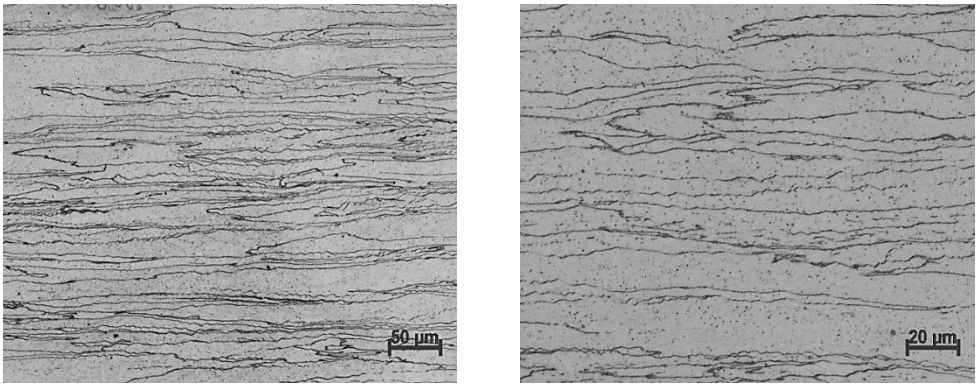

Fig. 5 Microstructure after rolling with ε = 71 % under ambient temperature

DOI 10.12776/ams.v25i4.1366 p-ISSN 1335-1532
e-ISSN 1338-1156

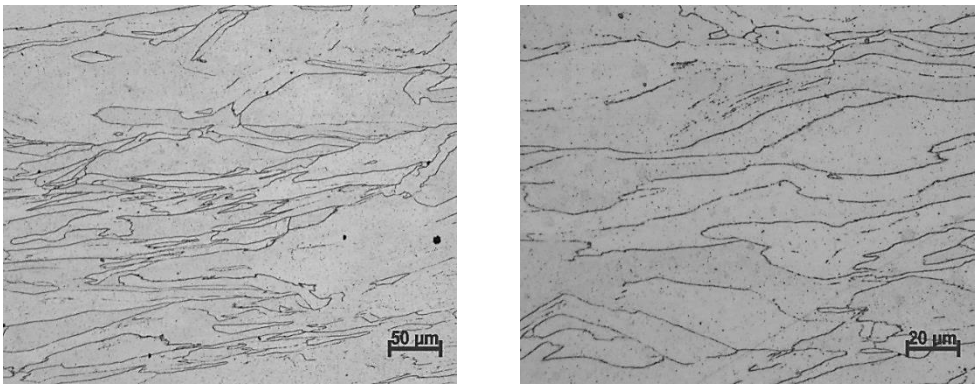

Fig. 6 Microstructure after rolling with ε = 71 % under ambient temperature

Conclusions

1. The strength properties after the rolling under AT and CT conditions were significantly increased.
2. Initial properties after L-PBF + HT2 were: $R_{p0,2,AT}$ = 377 MPa, R_m = 552 MPa and A_t = 76,5 % and $R_{p0,2,CT}$ = 616 MPa, $R_{m,CT}$ = 1058 MPa and $A_{t,CT}$ = 61,5 %.
3. The best level of yield strength was achieved after application of following conditions:
   - HT2 + ambient rolling (298K) with deformation ε = 71 % and tested by static tensile test at 298K formed $R_{p0,2}$=1070 MPa, R_m = 1190 MPa and A_t = 4,9 %
   - HT2 + cryogenic rolling (77K) with deformation ε= 40 % and tested by static tensile test at 77K formed $R_{P0,2}$=1390 MPa, R_m = 1580 MPa and A_t = 7,5 %.

References

[1] A. Adeyemi, E.T. Akinlabi, R.M. Mahamood: Materials Today: Proceedings, Vol. 5, 2018, No. 9, p. 18510 – 18517, http://dx.doi.org/10.1016/j.matpr.2018.06.193
[2] H. Wu et al.: Ceramics International, Vol. 42, 2016, No. 15, p. 17290-17294, http://dx.doi.org/10.1016/j.ceramint.2016.08.024
[3] R. Rajesh, S.S. Sajjan, V. Kulkarni: International Journal of Current Engineering and scientific Research, Vol. 2, 2015, No. 10, p. 91-100
[4] T.G. Spears, S.A. Gold: Integrating Materials and Manufacturing Innovation, Vol. 5, 2016, No. 2, p. 1-25, http://dx.doi.org/10.1186/s40192-016-0045-4
[5] J.P. Kruth: Annals of the CIRP, Vol. 45, 1996, No. 1, p. 183-186, http://dx.doi.org/10.1016/S0007-8506(07)63043-1
[6] K.J.A. Brookes: Metal Powder Report, Vol. 70, 2015, No. 3, p. 137-140
[7] A.T. Sutton, C.S. Kriewall, M.C. Leu, J.W. Newkirk: Virtual and Psysical Prototyping, Vol.12, 2017, No. 1, p. 3-29, http://dx.doi.org/10.1080/17452759.2016.1250605
[8] D. Manfredi, R. Bidulsky: Acta Metallurgica Slovaca, Vol. 23, 2017, No. 3, p. 276-282, http://dx.doi.org/10.12776/ams.v23i3.988
[9] P. Petroušek et al.: MM Science Journal, Vol. 2017, 2017, p. 1752, http://dx.doi.org/10.17973/MMSJ.2017_02_2016190
[10] A. Fedorikova et al.: MM Science Journal, Vol. 2016, 2016, p. 1586, http://dx.doi.org/10.17973/MMSJ.2016_12_2016189

[11] J. Bidulská, T. Kvačkaj, R. Bidulský, M.A. Grande, L. Lityńska-Dobrzyńska, J. Dutkiewicz, Chemicke Listy, Vol. 105, 2011, No. 16, p. 471-473
[12] J. Bidulská, T. Kvačkaj, I. Pokorný, R. Bidulský, M. Actis Grande: Archives of Metallurgy and Materials, Vol. 58, 2013, No. 2, p. 371-375, http://dx.doi.org/10.2478/amm-2013-0002
[13] M. Zavala-Arredondo et al: Materials and Design, Vol. 182, 2019, p. 108018, http://dx.doi.org/10.1016/j.matdes.2019.108018
[14] C. Zitelli, P. Folgarait, A. Di Schino: Metals, Vol. 9, 2019, No. 7, p. 731, http://dx.doi.org/10.3390/met9070731
[15] W.S.W. Harun: Powder Technology, Vol. 331, 2018, p. 74-97, http://dx.doi.org/10.1016/j.powtec.2018.03.010
[16] Ch. Yan et al: Materials Science and Engineering: A, Vol. 628, 2015, p. 238-246, http://dx.doi.org/doi.org/10.1016/j.msea.2015.01.063
[17] T. Neindorf et al: Metallurgical And Materials Transactions B, Vol. 44, 2013, No. 4, p. 794-796, http://dx.doi.org/0.1007/s11663-013-9875-z
[18] I. Yadroitsev, I. Smurov: Psysics Procedia, Vol. 5, 2010, No. B, p. 551-560, http://dx.doi.org/10.1016/j.phpro.2010.08.083
[19] X. Wang, X. Gong, K. Chou: Procedia Manufacturing, Vol. 1, 2015, p. 287-295, http://dx.doi.org/10.1016/j.promfg.2015.09.026
[20] T. Vilaro et al: Metallurgical And Materials Transactions A, Vol. 42, 2011, No. 10, p. 3190-3199, http://dx.doi.org/0.1007/s11661-011-0731-y
[21] C.Y. Yap et al: Applied Physics Reviews, Vol. 2, 2015, No. 4, p. 041101, http://dx.doi.org/10.1063/1.4935926
[22] O. Di Pietro, O. Rufini, A. Di Schino: Acta Metallurgica Slovaca, Vol. 24, 2018, No. 3, p. 207-212, http://dx.doi.org/10.12776/ams.v24i3.1130
[23] A. Di Schino: Metallurgist, Vol. 61, 2017, No. 7-8, p. 549-557, http://dx.doi.org/10.1007/s11015-017-0531-8
[24] A. Di Schino, M. Richetta: Acta Metallurgica Slovaca, Vol. 23, 2017, No. 2, p. 111-121, http://dx.doi.org/10.12776/ams.v23i2.841
[25] Y. Xiong et al: Materials Science and Engineering A, Vol. 709, 2018, p. 270-276, http://dx.doi.org/10.1016/j.msea.2017.10.067
[26] B. Fu et al: Journal of Materials Science and Technology, Vol. 34, 2018, No. 4, p. 695-699, http://dx.doi.org/10.1016/j.jmst.2017.09.017
[27] D. Šimčák, T. Kvačkaj, R. Kočiško, R. Bidulský, J. Kepič, V. Puchý: Acta Metallurgica Slovaca, Vol. 23, 2017, No. 2, p. 99-104, http://dx.doi.org/10.12776/ams.v23i2.928
[28] R. Kumar et al: Materials and Design, Vol. 67, 2015, p. 637-643, http://dx.doi.org/doi.org/10.1016/j.matdes.2014.11.014
[29] Y. Guo et al: Journal of Materials Science and Technology, Vol. 31, 2015, No. 4, p. 403-412, http://dx.doi.org/10.1016/j.jmst.2014.08.014
[30] G. Kalinin et al: Journal of Nuclear Materials, Vol. 233-237, 1996, No. 1, p. 9-16, http://dx.doi.org/10.1016/S0022-3115(96)00316-9
[31] J. Qin et al: Cryogenics, Vol. 53, 2012, No. 7-9, p. 336-339
[32] H.J. Liu et al: Cryogenics, Vol. 51, 2011, No. 6, p. 234-236, http://dx.doi.org/10.4028/www.scientific.net/MSF.667-669.707
[33] T. Kvackaj et al: Acta Physica Polonica A, Vol. 126, 2014, No. 1, p. 184-186, http://dx.doi.org/10.12693/aphyspola.126.184

[34] T. Kvačkaj et al: Acta Metallurgica Slovaca, Vol. 16, 2010, No. 4, p. 268-276

Acknowledgements
This work was supported by Slovak grant agency VEGA project No. 1/0599/18.

DOI 10.12776/ams.v25i4.1366 p-ISSN 1335-1532
e-ISSN 1338-1156

IDENTIFICATION OF THERMAL AND MICROSTRUCTURAL PROPERTIES OF HOT ROLLING SCALE

Badreddine Maalem [1], Djamel Berdjane [1], Okba Belahssen [2], Latifa Tairi [1], Youcef Faci [1], Samira Djemili [1]*

[1] Research Center in Industrial Technologies CRTI, P.O.Box 64, Cheraga 16014 Algiers, Algeria

[2] Physics Laboratory of Thin Films and Applications (LPCMA), University of Biskra, 07000, Algeria

Received: 31.07.2019
Accepted: 22.08.2019

**Corresponding author: bel_okba@yahoo.fr, Tel: +21374637626, Physic Laboratory of Thin Films and Applications (LPCMA), University of Biskra, 07000, Algeria*

Abstract

A significant amount of scale is produced during casting of ingots and processing of hot-rolled products. In manufacturing steel, during the various rolling operations, the amount of scale produced is approximately 0.1% of the annual production of the rolling mills. The quality of the thin sheet during rolling is affected by the behavior of the iron oxide layers formed on their surfaces. For this reason, acids and oils are used for the descaling of slabs and billets by means of pressurized water. The calamine, contaminated by these various acids and used oils, is rejected and stored involuntarily on important areas and pollutes soil and groundwater. Micrographic observations as well as X-ray diffraction analysis have shown that calamine consists mainly of iron oxides. Hematite and magnetite become the main components for oxidation times greater than 1 hour. Characterization tests have shown that calamine is dense ($\rho = 4.8$ g/cm^3), its particle size is variable depending on the degree of oxidation (from 0.5 to 10 mm). Simultaneous thermal analysis showed that an increase in mass of the calamine sample with a release of heat. Studies are underway for the physico-chemical characterization of the soils of the storage areas.

Keywords: Scale, risks, soil, thermal analysis, granulometry, X-ray diffraction

1 Introduction

Until the last decade, the scale, slag, dust and sludge generated by integrated steel plants wascalled waste, but now this term has been replaced with by-product and sometimes product due to intensive re-utilization of these materials. The management of all these substances generated in steel plants has become an important issue due to ever-tightening environmental regulations.

Mill scale is one of these materials produced in the processing of steel during continuous casting, reheating and hot rolling operations. Water sprays remove the scale formed during these operations and then mill scale is accumulated as a by-product in all iron and steel companies, either integrated iron and steel companies or mini steel mills and small mill shops.

Many researchers have found the structure and the thermal properties of scale formed during manufacturing of carbon steels were realized for a long time [1].

However, the research in this field was always actively studied by numerous specialists, in particular those of the steel industry [2].

DOI 10.12776/ams.v25i4.1360 p-ISSN 1335-1532
e-ISSN 1338-1156

In the steel-making manufactory, the flat products are hot-rolled. The quality of the thin sheet steel during the process of rolling is allocated by the formation of the layers of scale on the surface of the sheet steel to the cost all the operation of deformation along the hot rolling mill process. To minimize his growth inside the furnace, we have to respect certain necessary conditions among which the content in smokes which has to be between 1.5 - 2.5 %.
In the high-temperature heating of steel in pusher furnaces operating under traditional conditions with excess oxidant (usually ratio n = air/gas (1.1 to 1.3), three layers of oxides are formed on the surface of the steel.
The iron content is around 67%, a large part of the scale is under magnetite and hematite, namely the oxygen content in the furnace. A certain amount of magnetite crystals will be present in the wüstite.
The degree of oxidation of the steel depends on the temperature, the chemical composition of the metal and the gas composition [3].
The steel where our scrap is collected is an extra-soft hot rolled low-carbon steel according to the international standard ISO 11949 for packaging called black iron, tinplate.

2 Materials and methods

The chemical compositions of the mill scale and the hot rolled steel are identified by SIEMENS SRS 3000 FRX analyzer. The composition is represented in **Table 1**.

Table 1 Chemical analysis of the hot rolled low-carbon steel

Elements		C	Mn	Si	S	P	Al	Fe
%		0.09	0.35	0.04	0.025	0.025	0.05	Balance

- The scanning electron microscopy analyses are carried out on scale scrap collected from the hot rolling mill and on polished surfaces of the same sample using ZEISS EVO-MA 25 scanning electron microscopy. Driven by integrated software where one can acquire micrographic results and chemical analysis by EDS.

The cooling system ensures proper functioning of the components to ensure a secondary vacuum, a 99.99% pure nitrogen bottle is connected to the equipment.
The principle of scanning electron microscopy is based on electron-matter interaction. The incident electron will interact with the nucleus, the more bound electrons of matter and the electrons of the outer layers [4, 5, 6].

- AccuPyc II Series 1340 pycnometers are fast, fully automatic pycnometers that provide high-speed, high-precision volume measurements and true density calculations on a wide variety of powders, solids and slurries.
- The thermal analysis tests were performed by SDT Q600 V20.9 Build20 equipment. The sample holders used are made of alumina. The tests were carried out in a controlled atmosphere in order to avoid possible contamination of the samples. Among the advantages in operating curves, it gives the results coupled on a single graph for example DSC-TGA.
- The quantitative analysis of the constituents of calamine was determined using a rigaku diffractometer equipped with a copper anticathode tube. The diffraction pattern is made in the range 2 theta 10° range at 90° and with a scanning speed of 5 °C/ min.

The instrument completes most sample analyses in less than three minutes without sacrificing accuracy. Once the analyses are started with a few keystrokes, the data is collected, the calculations made and the results displayed. Minimal operator attention is required.

DOI 10.12776/ams.v25i4.1360 p-ISSN 1335-1532
e-ISSN 1338-1156

3 Results and discussions

The mill scale picked up by the hot rolling mill has a grey color. The result of his chemical analysis and granulometry dried at the temperature-time conditions (T = 105 °C, 24h) are represented in the **Tables 2** and **3**.

Table 2 Chemical analysis of raw mill scale

Elements	Fe	FeO	Fe_2O_3	Fe_3O_4	MnO	TiO_2	SiO_2	CaO	Al_2O_3
%	7.04	9.09	20.22	29.31	0.36	0.05	0.34	0.05	0.03

Table 3 Results of granulometry analyzes of the raw mill-scale after drying at 105 °C - 24h

Size [µm]	Mass [g]	Rate[%]	Cumul refuse[%]
>200	0.00	0.00	0.00
125-200	0.381	3.81	3.81
90-125	1.166	11.64	15.45
63-90	2.250	22.47	37.92
45-63	3.137	31.33	69.25
<45	3.079	30.75	100
Total	10.013	100	/

The micrographs taken by scanning microscopy and for different magnifications show the microstructural appearance of laminated iron oxides in layers that are more or less large according to the phases and their distribution over the layer of scale formed (**Figs. 1, 2**).
Thus providing a motor element for the iron to spread through the hematite layer. The inner wüstite-iron interface has become corrected initially; then with the rapid advance of some protruding sections, some parts of the wüstite layer were reduced by first and ultimately the wüstite holding of the islands was reduced to complete the reduction process.

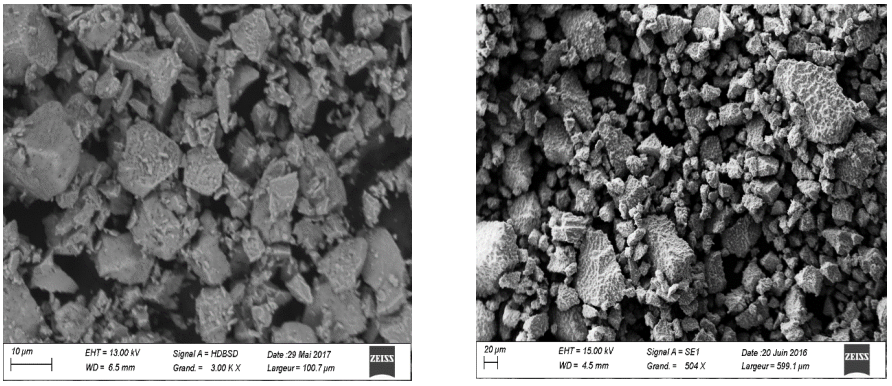

a) b)

Fig. 1 SEM micrographs showing obviously cluster's areas which iron oxides (a) raw scale, (b) scale after milling.

Porosities were produced when wüstite islands were reduced due to localized volume shrinkage. Higher oxygen concentrations in the underlying areas of the near-edge samples were assumed responsible for their slower reduction rates than those at the center [7, 8].

DOI 10.12776/ams.v25i4.1360 p-ISSN 1335-1532
e-ISSN 1338-1156

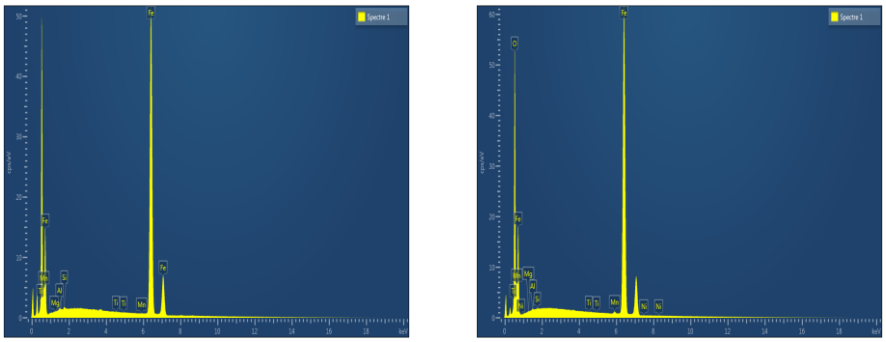

a) b)

Fig. 2 EDS of raw scale and scale after milling (a) raw scale, (b) scale after milling.

The pure iron scale is formed by three layers of superimposed oxides, corresponding to increasing levels of oxidation from the metal to the atmosphere, the layer of FeO protoxide against the metal, then the layer of magnetite Fe_3O_4, then a very thin layer of Fe_2O_3 hematite on the surface, these phases were confirmed by X-ray diffraction (**Fig.3**).

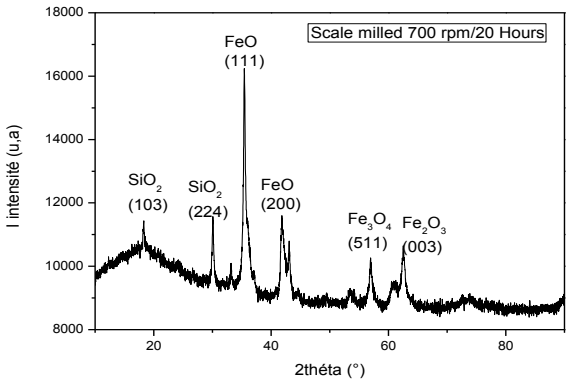

Fig. 3 X-Ray diffraction results of raw powder milling under 700 rpm for 20 h

An annealing at T = 700 °C for 1h with a heating rate from 20 °C/min to that of maintenance is made for mill scale.

The heating rate adopted is 10 °C/min, which is swept from room temperature to T = 1100 °C. The choice of rise of temperature is based on findings revealed on work carried out in this direction and which proved conclusive technical results [10, 11].

On the thermal analysis curves, we can observe the appearance of peaks; we have two peaks, one endothermic at T = 340 °C and the other exothermic at T = 570 °C.

The endothermic peak represents the transformation of ϫ-Fe_2O_3 to α-Fe_2O_3. However, at the exothermic peak at T = 570 °C, a process of beginning of rearrangement of the grains is what is called a primary recrystallization, which takes that the transformation beginning of wüstite to magnetite took place in **Fig. 4**. Above T = 1000 °C, the trend of the heat flow curves and that of DSC is not perfectly clear. From a stability point of view, a steady state will be established in **Fig. 4**. A slight peak can be seen at T = 570 °C in **Fig. 5**.

DOI 10.12776/ams.v25i4.1360 p-ISSN 1335-1532
e-ISSN 1338-1156

For the sample which has been annealed at T = 580 °C for 2 hours with heating rate from 20 °C/min to the holding temperature followed by oven cooling small size grain of oxides has been confirmed. In figure 5, the loss of mass takes a linear appearance from T = 600 °C to T = 1100 °C.

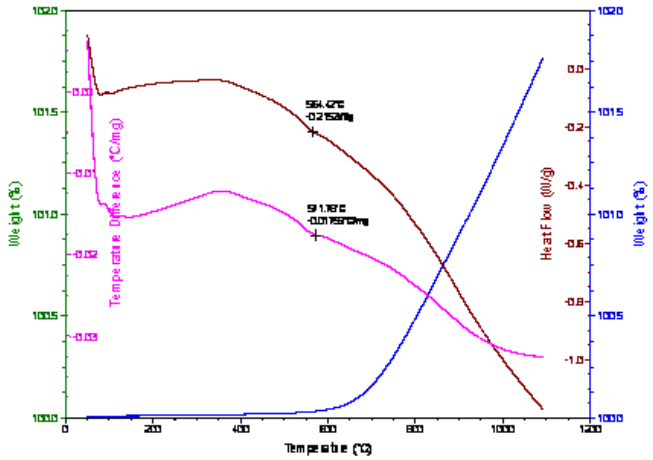

Fig. 4 DSC-TGA of the studied raw scale.

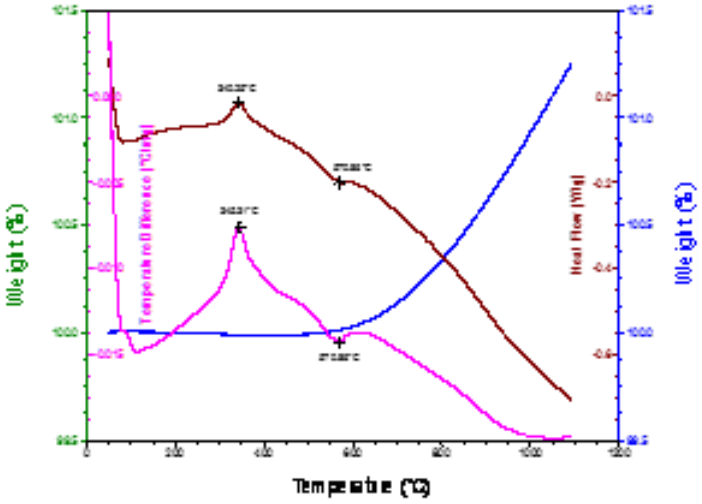

Fig. 5 DSC-TGA of the studied mill scale treated at T = 700 °C

4 Conclusion

This study allowed us to identify the thermal and microstructural properties of calamine from the hot rolling mill for later exploitation in the industrial field.

These oxides are confirmed with X-ray technique which their shape and dispersion were been obviously seen in SEM with different magnificent.

DOI 10.12776/ams.v25i4.1360 p-ISSN 1335-1532
e-ISSN 1338-1156

The chemical analysis shows a total iron of the order of 67 % with other oxides in trace.
The particle size of the powder has an average diameter of the order of 50 μm and with wet and dry densities respectively 5.42 and 5.67 g/cm^3. The presence of silicon was confirmed by X-ray analysis and the most phases common are magnetite and hematite and the SEM micrograhs corroborate their allocation. The presence of silicon is confirmed by EDS analysis.

References

[1] L. A. Shult's, Reducing the High-Temperature Loss of Steel in Furnaces, Steel in Translation, Vol. 46, 2016, No. 7, p. 467–473, http://dx.doi.org/10.3103/S0967091216070123
[2] C. Eyraud and A. Accary, Analyses thermique et calorimétrique différentielles, Traité Analyse et caractérisation, number PE 1295, pp.1-14, 1992. Techniques de l'ingénieur, 1992.
[3] M. Grafoute, Etude Des Propriétés Structurales et Modélisations de Poudres Nanostructurées de Fer obtenues par Broyage Mécanique, thèse de doctorat, Université du Maine, France, 2004. http://pecbip2.univ-lemans.fr/docpdf/theseMG.pdf
[4] S. Chandra, K. Ngamkham, N. Jiratthanakul, Effects of Process Parameters on Mechanical Adhesion of Thermal Oxide Scales on Hot-Rolled Low Carbon Steels, Oxid Met, Vol. 80, 2013, p. 61–72, http://dx.doi.org/10.1007/s11085-013-9370-6
[5] M. Krzyzanowski, J.H. Beynon, D.C. Farrugia, Oxide Scale Behavior in High Temperature Metal Pressing, Wiley & Sons, Weinheim, 2010, http://dx.doi.org/10.1002/9783527630318
[6] D. Genève, D. Rouxela, P. Pigeata, M. Confente, Descaling ability of low-alloy steel wires depending on composition and rolling process, Corrosion Science, Vol. 52, 2009, p. 1155-1166, http://dx.doi.org/10.1016/j.corsci.2009.12.028
[7] J. Xu, Kinetics of Wüstite Formation and Reduction of Manganese alloyed Steel, Master Thesis, Delft University of Technology, Netherlands, 2013. http://resolver.tudelft.nl/uuid:47957f9e-8ee2-4c00-9cb8-9bbd49b7c7f9
[8] R.Y. Chen, Mechanism of Iron Oxide Scale Reduction in 5%H2–N2 Gas at 650–900 °C, Oxid Met, Vol. 88, 2017, No.5-6, p. 687-717, http://dx.doi.org/10.1007/s11085-017-9769-6
[9] G. Naveen Kumar, Y.V. Mohana Reddy, K. Hemachandra, Reddy Synthesis and characterization of iron oxide nanoparticles reinforced polyester/nanocomposites, International Journal of Scientific and Research Publications, Vol. 5, 2015, No. 8, p.1-13, doi. ISSN 2250-3153
[10] S. Ahmed Al-Kadya, M. Gaber, M. Hussein, B. El-Zeiny, M. Ebeida, Structural and fluorescence quenching characterization of hematite nanoparticles, Spectrochimica Acta, Vol. 83, 2011, p. 398–405, http://dx.doi.org/10.1016/j.saa.2011.08.052
[11] S. Chandra-ambhorn, T. Nilsonthi, Y. Wouters, A. Galerie, Oxidation Kinetics, Mechanical Adhesion and Pickling Behaviour of Thermal Oxide Scales on Hot-rolled Conventional and Recycled Steels, Steel Research International, Vol. 81, 2010, No. 9, p. 130-133, http://dx.doi.org/ 10.4028/www.scientificnet MSF.696.170

DOI 10.12776/ams.v25i4.1360 p-ISSN 1335-1532
e-ISSN 1338-1156